STUDIA

UNIVERSITATIS BABEŞ-BOLYAI

PHYSICA

1

1990

CLUJ-NAPOCA

ANUL XXXV 1990

STUDIA
UNIVERSITATIS BABEŞ-BOLYAI

PHYSICA

1

Redacţia 3400 CLUJ-NAPOCA, str M Kogălniceanu, 1 ● Telefon 11 61 01

SUMAR — CONTENTS — SOMMAIRE

STUDIA UNIV. BABEŞ-BOLYAI, PHYSICA, XXXV, 1, 1990

THEORETICAL APPROACH TO GAS TRANSPORT THROUGH METALLIZED POLYMER MEMBRANES

T.A. BEU*, P. MERCEA** and D. SILIPAŞ**

ABSTRACT. — By using a finite difference technique, a two-dimensional Laplace type equation of the gas transport through a metallized polymer membrane was solved numerically, in conjunction with a specific set of boundary conditions The obtained concentration profiles were used to determine the flux of gas which permeates through an whidcal metallized polymer membrane The influence of the membrane thickness and of the size of the pinhole-shaped defects in the structure of the metal layer are also discussed These theoretical results are compared with experimental ones, obtained for the permeation of He, CO_2, Ar and N_2 at 50 °C through a poly (ethylene terephtalate) membrane metallized with palladium.

Introduction and Background. Products made of polymeric materials may be coated or plated with a thin, continous and adherent layer of metal by vacuum deposition [1], chemical [2] or electrochemical [3] plating. Most of the commercial metallized polymer membranes (MPM) are produced by vacuum deposition and are widely used for packing, for winding to form capacitors, as superinsulating materials for thermal blanketing, as gas and vapor barriers and for decorative purposes. There is a wide range of polymeric substrates polyesters, polypropylene, polycimide, polycarbonate, polyethylene and cellophane, on which Al, Zn, Au, Ag, Cu and Ni are deposited [4]. Usually, MPM are produced commercially in reel-to-reel machines, in which the polymer membrane is transversed at low speeds, about a few meters per second, above the metal held molten in resistence-heated boats [5]. In laboratory, MPM are produced individually in small vacuum chambers [6]. The ratio of the deposited metal thickness to the polymer membrane thickness is usually about 1 . 1000. This very thin coating has a strong influence not only on the optical and electrical properties, but also on the gas permeability of the polymer membrane. The structure properties of aluminized polyester membranes was studied by light and scanning electron microscopy [7]. It was found that the deposited Al layers, both by reel-to-reel and by individual techniques, show up to about 10^3 defects/mm^2 These defects are mainly caused by the presence of dust particles on the polymer membrane surface during metallization which, subsequently, become dislodged and leave an unmetallized shadow Damage by scuffing of particles can also produce defects which are often observed as „runs" It was reported [6] that Ni, Pd and Cu layers, deposited by means of an individual technique on poly (ethylene terephtalate) (PET) membranes, showed cracks in their structure as well These cracks probably appear as a result of the difference between the contraction coefficients of the polymer and the metal.

* *University of Cluj-Napoca, Department of Physics, R—3400 Cluj-Napoca, Romania*
** *Institute of Isotopic and Molecular Technology, P.O. Box 700, R—3400 Cluj-Napoca, Romania*

The gas-barrier and gas-selective properties of the MPM were studied experimentally elsewhere [6—10]. It was found that for gases which are unable to dissolve in the deposited metal layer, the actual gas-barrier properties of the MPM are governed by the defects which are inevitably produced in the metal layer during the preparation and/or testing of the MPM. Depending on the quality of the deposited metal layer, the gas-barrier property may determine a decrease of the overall rate of gas transfer through the MPM with up to more than two orders of magnitude [8].

On the other hand, the gas-selective property of an MPM depends essentially on the fact whether a given gas is able or not to dissolve in, and diffuse through the metal layer itself. Among the gases studied in refs. [6, 10 and 11], only H_2 had the ability to dissolve in Pd, and to a smaller extent in Ni It was found that the selectivity for H_2 of a PET membrane metallized with a 1000 Å thick Pd layer is with up to more than one order of magnitude larger than that of a bare PET membrane [10] The above mentioned properties of the MPM may be explained in terms of a phenomenological model of the gas permeation [6]

A theoretical treatment of gas transport through an MPM has been given [12] In order to derive an analytical expression for the flux of gas which permeates through an MPM it was assumed that all defects of the impermeable metal layer are circular pinholes of radius r_0, and that there are n pinholes per cm². The steady state flux of gas through a single-pinhole MPM is given by

$$Q_1 = -D\int_0^{r_0} 2\pi r\, dr\, (\partial c/\partial z)_{o,} \qquad (1)$$

where D is the diffusion coefficient, c is the gas concentration in the polymer z and r are the coordinates of the cylindrical coordinate system with the origin at the pinhole center, Fig. 1 Hence, the total flux per cm² is $Q = nQ_1$

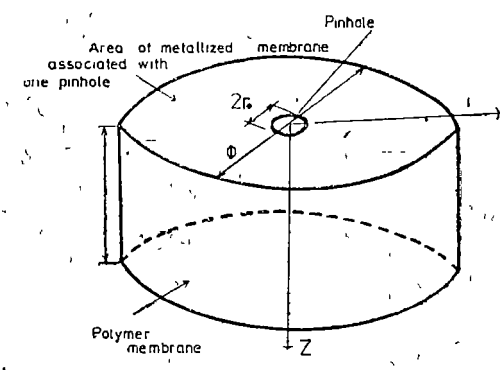

Fig 1 Geometric framework of the FDA, showing the assumption of isolated pinholes and associated polymer cylinder

Provided the pinholes are smaller than the thickness of the polymer, l, i.e $\lambda = l/ro > 0\,3$, an approximate analytical expression for $c(z, r)$ was derived by solving the twodimensional Laplace equation

$$\partial^2 c/\partial r^2 + (1/r)\ \partial c/\partial r + \partial^2 c/\partial z^2 = 0 \qquad (2)$$

with the boundary conditions

$$c(0,r) = c_2 \qquad \text{for } r \leq r_0 \qquad (3)$$

$$(\partial c/\partial z) = 0 \qquad \text{for } r > r_0 \qquad (4)$$

$$c(1,r) = c_1 \qquad \text{for all } r \qquad (5)$$

Using a graphical integration method, it was shown that Q can be expressed to a good approximation as

$$Q = D\theta(1 + 1.18\lambda)(c_2 - c_1)/l \text{ provided } \theta \ll 1 \quad (6)$$

where, $\theta = \pi r_0^2 n$ is the fraction per cm² of the polymer surface that is not metallized, and c_1 and c_2 are the concentrations of the dissolved gas just below the downstream and upstream surface of the polymer, respectively. Eq. (6) shows an interesting feature. The flux of gas which permeates through a bare polymer membrane of thickness l and area θ, which is the so-called "free" surface of the previously mentioned MPM, is given by:

$$Q_0 = D\theta(c_2 - c_1)/l \quad (7)$$

Therefore, from Eqs. (6) and (7) one may notice that, in the limit of large λ, Q can become many times larger than Q_f. Qualitatively this result is understandable: the thicker the membrane compared to the size of the pinhole, the more the diffusing gas spreads in the polymer membrane. On the other hand, the total flux per cm² through a bare polymer membrane, Q_0, is given by [13].

$$Q_0 = D(c_2 - c_1)/l \quad (8)$$

It follows that the ratio Q/Q_0 is a function of geometrical parameters only, such as membrane thickness and pinhole radius and density. Additionally to the l and r_0 dependence showed by Q/Q_0 in Eqs. (6) and (8) of [6,10 and 11] it was found that Q/Q_0 depends on the nature of the penetrant gas as well. This fact seems to indicate that the gas transport through an MPM is a more complex process than that simulated in [12] for the experimental confirmation of Eq. (6), by means of a simple electrical analog. In order to explain the experimental evidence, one can assume that a selective molecular flow through the smaller defects of the metal layer, a surface diffusion and an additional flux of gas which diffuses through preferential paths along the metal grain boundaries, may have a contribution to the overall rate of gas transfer through an MPM.

Another technique to calculate the flux of gas which diffuses from a pinhole through a polymer membrane is the finite element approach (FEA) of [7]. The basis of the FEA is a two-dimensional net of points representing the cylinder depicted in fig. 1. At each point of the cylinder the equation

$$w_n c_n + w_{n+1}c_{n+1} + w_{n+2}c_{n+2} + w_{n+3}c_{n+3} = (w_n + w_{n+1} + w_{n+2} + w_{n+3})c_0 \quad (9)$$

is applied, where $c_0, c_n, \ldots, c_{n+3}$ represent gas concentrations, c_0 being at the point under consideration, and $w_n, \ldots, w_{n+3}$ are weightings that allow two-dimensional representation of the three-dimensional problem. Eq. (9) creates a new array of points, and the equation is repeatedly applied until the system converges. The initial array of points was chosen so that $c(z, 0)$ shows a constant gradient and $c(0, r)$ is set up as a logarithmic decay from $c(0, r_0) = c_2$ to some assumed value at the outer surface of the cylinder.

As an example, for an MPM with a thickness $l = 12$ μm, and a density of pinholes $n = 400$ pinholes/mm², the results obtained by means of the theoretical models mentioned above can be compared in terms of the relative flux

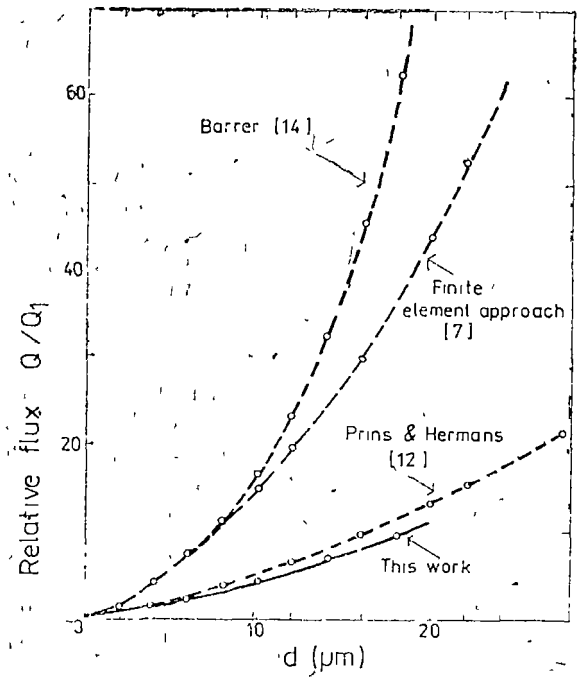

Fig 2 Relative permeabilities of metallized polymer membranes, calculated as function of pinhole diameter

Q/Q_1 dependence on r_0 (Fig 2) where Q_1 is the gas flux which permeates through n pinholes with $r_0 = 1$ μm

In Fig 2, the obtained results are also compared with approximate calculations [14] for the outwards diffusion from the center of a sphere:

$$Q = 4\pi D(c_2 - c_1)\, ab/(b - a) \tag{10}$$

where a and b are the inner and outer radii of the spherical shell and they can be approximately related to r_0 and l. Eq. (10) is appropriate only for pinholes of diameter considerably smaller than l. Even for small diameters Eq (10) tends to overestimate Q, as it really assumes a hemispherical volume of polymer behind the pinhole rather than the sheet of polymer itself The fact that the relative flux, Q/Q_1 derived from Eq (6) is smaller than that given by the FEA seems to indicate that, in this latter case, the considered boundary conditions lead to an overestimation of the volume of the polymer cylinder associated with each pinhole or/and that the concentration gradient considered along the z axis is not the real one

In fig 2 we also show the dependence of the ratio Q/Q_1 on r_0, calculated in the present work by means of a finite difference approach

Finite Difference Approach. In order to determine theoretically the flux of gas which permeates, due to a pressure difference $\Delta p = p_2 - p_1$, through a MPM, let us make the following assumptions

First, we will assume that the defects in the structure of the impermeable metal layers of the MPM are all circular pinholes, with diameters d_i The size and distribution of the d_i's can be established experimentally, for example, by means of scanning electron microscopy [7, 10] We will also assume that the pinhole spacings allow for the additivity of the single-pinhole permeation fluxes. Let us call such an MPM, an "ideal" MPM, and assume that the gas permeates through the pinholes of its metal layer only

Then, there will by imposed no restriction on the thickness of the metall layer, which will have an influence on the gas permeation through the MPM only in those cases where the pinholes act essentially as channels When these

channels are comparatively long, the rate of the permeation process may be determined to a certain extent by the flow regime of the permeating gas in the channels.

We will finally assume that a steady state diffusion has been established through the MPM, in which the concentration of the penetrant gas the upstream and downstream boundaries of the polymer substrate are c_2 and c_1, respectively. For some simple gases, such as He, H_2, N_2, Ar and CO_2, c_2 and c_1 will be determined by the pressures p_2 and p_1 on either side of the MPM. It is generally accepted that for the above mentioned gases and for $p_1 < p_2 \approx \approx 1$ atm, c_2 and c_1 obey Henry's law [15], which states that the pressure and the concentration are proportional to each other. Moreover, in these cases one can assume that D is independent of concentration and $c_1 \approx 0$.

Depending on the way the MPM was prepared and disposed into the experimental set up, one may distinguish between three cases:

Case I. The MPM shows a single impermeable metal layer deposited on a nonporous polymeric substrate, and the metal layer faces the upstream chamber of the experimental set up

Case II. Same as above, but the metal layer faces the downstream chamber of the set up.

Case III. The MPM has been made by depositing on each surface of the polymeric substrate a metal layer. For the purpose of our discussion, it is immaterial whether these metal layers have or not the same thickness, and are made of the same material or not.

In this paper we will mainly concentrate on the gas permeation through an MPM in the first case

The geometric framework used for the calculation of the flux of gas through a single-pinhole MPM is the one presented in Fig. 1 We associate to each pinhole a circular metal layer area of diameter Φ, which results from dividing the total area of the MPM by the total number of pinholes, $N = \Sigma n_i$, where i spans the distribution of the pinholes according to size (see, for example, Fig 1 of [10]).

The above assumptions lie at the basis of our finite difference approach, FDA, used to calculate the flux of gas, Q, which permeates through a single-pinhole MPM Knowing the size and distribution of pinholes, we can then determine the overall flux of gas by summing up the contributions from all pinholes.

In order to calculate Q, we solve Eq (2) subject to boundary conditions (3–5) and placing two additional boundary conditions.

$$(\partial c/\partial r)_{r=0} = 0 \qquad \text{for all } z \tag{11}$$

$$(\partial c/\partial r)_{r=\Phi/2} = 0 \qquad \text{for all } z \tag{12}$$

The Dirichlet-type boundary conditions (3) and (5) prescribe the value of c at the free upper and lower boundaries of the MPM, respectively The reflective Neumann-type boundary conditions (4) an (12) prevent the gas to cross the metallized area of the MPM and the outer boundary of the cylinder, respectively Condition (11) prescribes the natural symmetry of the concentration profiles with respect to the z-axis.

In order to solve Eq (2) in conjunction with this extended set of boundary conditions, a finite difference technique was chosen Actually, we solved numerically the more general problem of the two-dimensional Poisson equation in cylindrical coordinates.

$$[\partial^2/\partial r^2 + (1/r)\ \partial/\partial r + \partial^2/\partial z^2] f(z, r) = g(z, r) \quad (13)$$

Details of the discretization schemes and the algorithm used in this work can be found elsewhere [16]

Results and Discussions. A first set of our calculations concern the permeation of He, CO_2, Ar and N_2 through a 30 μm thick PET membrane metallized with one 500 Å thick Pd layer The permeability of this MPM at 50 °C and $\Delta p \sim 70$ cm Hg and the distribution of pinholes according to size were determined previously [10] It was found that for the MPM in question, the mean number of pinholes per mm², N, is 172, yielding a total pinhole area of about $7\,6 \times 10^{-3}$ μm²/mm² Therefore, as already mentioned, to each pinhole one can associate a cylinder which has a diameter $\Phi \sim 43$ μm, and by means of the FDA one can determine the flux of gas, Q_i, which permeates through this cylinder The total flux per cm², Q, which permeates through the MPM, is then given by $Q = \Sigma\, Q_i n_i$

Table 1

Experimental and calculated flux of gas which permeates at $t = 50$ °C and $\Delta p \sim 70$ cm Hg through a 30 μm thick PET membrane metallized with 500 Å of Pd

Gas	Q_{MPM}	Q_{MPM}(a)	Q_{MPM}(b)	Q_{PET}(c
		cm³/cm²s × 10^{-7}		
He	2 92	20 00	3 50	49 00
CO_2	0 44	6 10	0 60	8 10
Ar	0 28	0 66	0 36	5 10
N_2	0 16	0 40	0 21	3 10

(a) Ref [10]
(b) As calculated from Eq (6) of [12]
(c) Refs [6] and [10]

The theoretical results obtained for the MPM and gases mentioned above are summarized in Table 1 One can compare these results with those calculated by means of Eq (6), which was modified in order to take into account that the pinholes may have different radii r_0 [10], and with the experimental results in [6 and 10] For He and CO_2 the calculated fluxes are about 20 times smaller than the experimental ones for the bare PET membrane The situation is reversed when one compares the fluxes calculated from Eq (6) with those in [10] there is a quite good agreement for Ar and N_2, but a rather poor one for He and CO_2 These disagreements may be caused by the fact that the gas fluxes determined with the FDA, the FEA and the model given in [12] depend on the geometrical parameters of the MPM only, and not on the

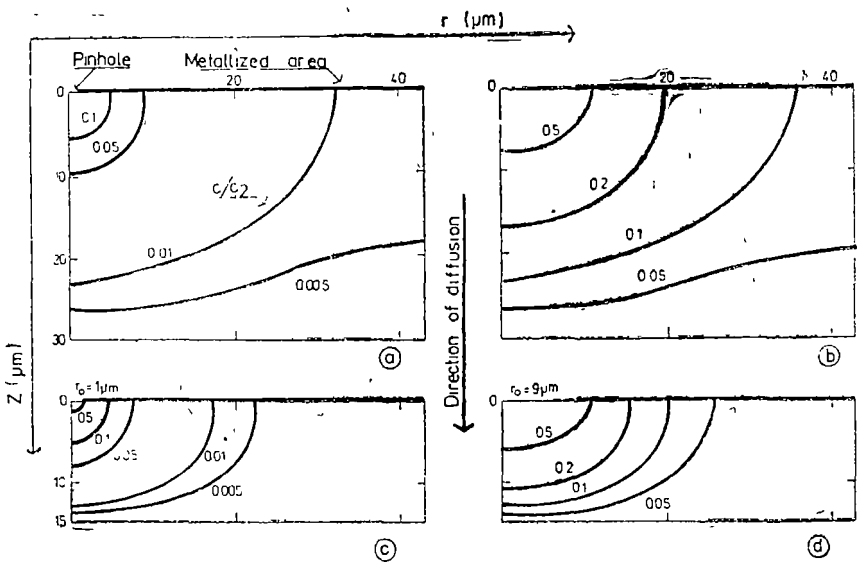

Fig 3 Calculated normalized concentration profiles for a) $l = 30\ \mu m$, $r_0 = 1\ \mu m$, b) $l = 30\ \mu m$, $r_0 = 9\ \mu m$, c) $l = 15\ \mu m$, $r_0 = 1\ \mu m$, b) $l = 15\ \mu m$, $r_0 = 9\ \mu m$

nature of the penetrant gas, as discussed above Nevertheless, the FDA offers the possibility to determine, for a given pinhole distribution, the order of magnitude of the gas flux through an MPM

As part of our FDA it is possible to determine the gas concentration profiles in the polymer associated with any particular single-pinhole MPM geometry, both in *Case I* and *Case II* Such calculations were performed for membrane thicknesses ranging from 5 to 30 μm, and pinhole diameters ranging from 2 to 18 μm Fig 3 shows, as examples, the calculated normalized concentration profiles for some MPM geometries

In Figs. 3a-d one can see that the distribution of the penetrant gas into the polymer matrix is strongly dependent on both r_0 and l Therefore, it is worth determining the dependence of the relative flux Q/Q_1 for an MPM of a given thickness l with the pinhole radius r_0 In Fig 4, Q/Q_1 is plotted versus r_0 for three particular values of the MPM thickness

In Figs 2 and 4, the flux normalization was accomplished relative to the flux corresponding to a pinhole with radius $r_0 = 1$ μm In Fig 4 one can notice that in the limit of large r_0, the gas flux decreases with increasing of the polymer layer thickness

On the other hand, Fig 5 present plots of Q / Q_1 as function of l for three different values of r_0 An interesting fact evidenced in Fig 5 is the comparative insensivity of the permeability with respect to the polymer membrane thickness, especially for small pinholes For the typical pinhole radius of 1 μm, the predicted barrier properties are virtually independent of l A consequence

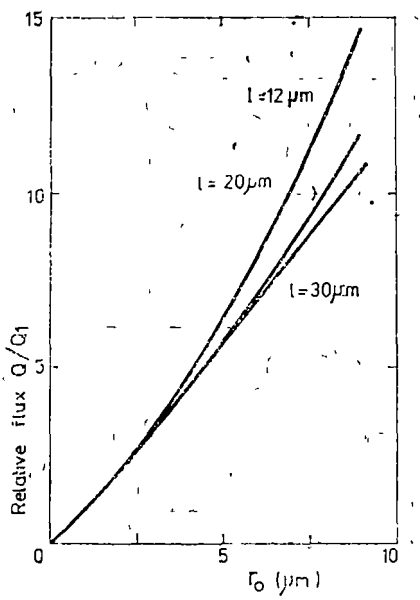

Fig 4 Relative flux dependence on the pinhole radius

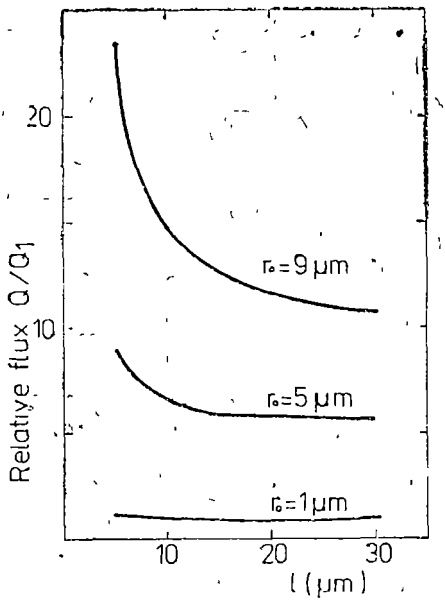

Fig 5 Relative flux dependence on the polymer substrate thickness

of the behavior presented in Figs 4 and 5 is that if the gas-barrier performance of an MPM is expressed in terms of the improvement ratio, that is, the ratio of the permeabilities of bare to metallized membrane, then the ratio will have meaning only for a fixed substrate thickness It also follows that, for a given metallization quality, the improvement ratio is dependent on the reciprocal of the film thickness.

Relative concentration profiles along the Oz and Or directions are plotted in Figs 6 and 7, versus relative membrane thickness, z/l, and relative associated cylinder diameter, $2r_0/\Phi$, respectively.

One can find from fig. 6 that the relative concentration along the Oz axis is influenced both by r_0 and l. For small pinholes, the concentration profile is especially steep just below the edge of the pinhole and its steepness increases with l For example, in a 30 μm thick MPM with $r_0 = 1$ μm, c drops to half of its initial value, c_2, at a depth smaller than the radius of the pinhole As one may observe from the plotted concentration profiles, the case $r_0 \to \infty$, i e. $\lambda/r_0 \to 0$, will lead to a constant $(dc/dz)_{r=0}$, which is characteristic for a bare polymer membrane.

The dependence of the concentration on r_0 and l along the Or axis shows some interesting features, as well (Fig 7) For small pinholes, the profile is very steep near the pinhole and shows little if any dependence on the thickness of the MPM For large pinholes, the concentration profile becomes less steep in the vicinity of the pinhole and, at the same time, the gas spreads out more into the thicker MPM. Figs. 6 and 7 seem to suggest that the gradient pre-

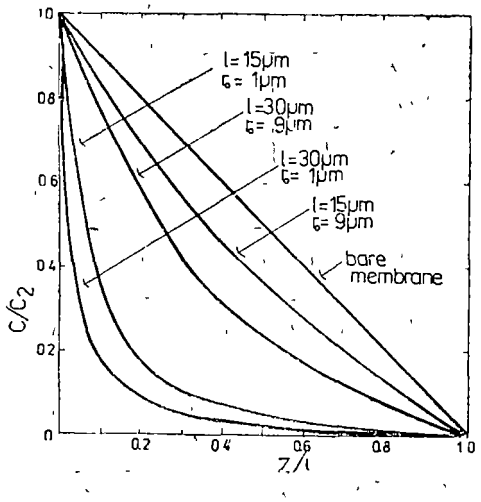

Fig 6 Relative concentration profile along the Oz axis

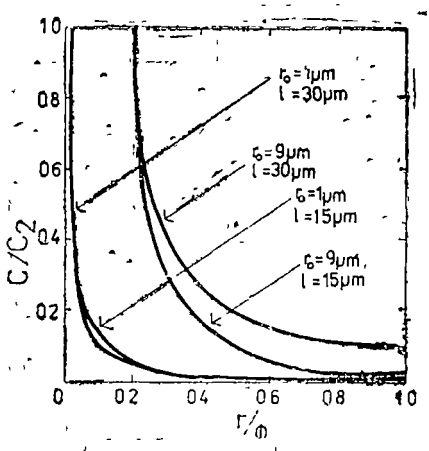

Fig 7 Relative concentration profile along the Oz axis

scriptions used for the FEA calculations [7] represent a rather rough approximation, which, eventually, leads to an overestimation of the overall rate of the gas transfer through an ideal MPM (see Fig. 2).

Fig 8 shows in *Case I* the dependence of $z_{1/2}$, the z axis distance where the concentration drops to half of its initial value, c_2, on both l and r_0. One can easily observe that, for a given r_0, $z_{1/2}$ is relatively insensitive to l. On the other hand, for a given l, $z_{1/2}$ increases almost linearly with r_0.

The FDA was also used for gas flux calculations in *Case II*. For this purpose, Eq. (2) was solved subject to an appropriate set of boundary conditions:

$$c(O,r) = c_2 \qquad \text{for all } r \qquad (14)$$

$$c(l,r) = c_1 \qquad \text{for } r \leqslant r_0 \qquad (15)$$

$$(\partial c/\partial z)_{z=l} = 0 \qquad \text{for } r > r_0 \qquad (16)$$

$$(\partial c/\partial r)_{r=l} = O \qquad \text{for all } z \qquad (17)$$

$$(\partial c/\partial r)_{r=\Phi/2} = O \qquad \text{for all } z \qquad (18)$$

Finally, it was found that for a given r_0 and l the gas flux is the same as in *Case I*. This result is in good agreement with those found experimentally [10] for the permeation of He, N_2, Ar and CO_2 through PET membranes de-

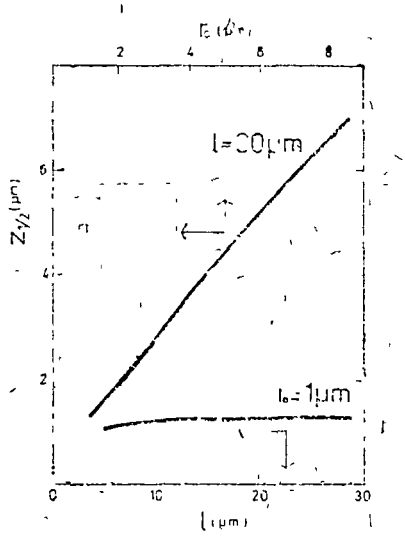

Fig 8 Dependence of the z axis distance where the concentration drops to half of its upstream value, c_2, on the MPM thickness and on the pinhole radius

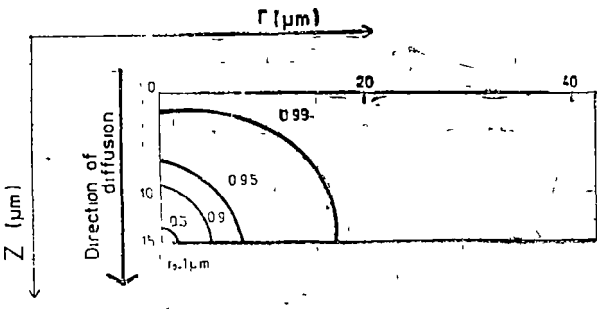

Fig 9 Calculated normalized concentration profiles for the permeation of a gas through a MPM in *Case II*.

posited with Pd Moreover, this result may be of practical value, because it allows one to deposit the metal layer in such a way as to be protected from any chemical or mechanical damage. The concentration profiles for a MPM withgeo metrical parameters $l = 15$ μm and $r_0 = 1$ μm are given in Fig. 9 Let us compare Fig. 9 with the corresponding figure in *Case I*, i e Fig 3c.
One can observe that by reversing Fig 3c with respect to the *Or* axis, and by summing up the relative concentrations, c/c_2, at every point of these concentration profiles, one obtains the constant value 1

We have plotted in Fig 10 the concentration profiles for the gas permeation through an MPM in *Case III* The geometrical parameters employed were $r_0 = 1$ μm for both pinholes, $l = 15$ μm and the center of the pinhole of the downstream metal layer is located at $\Phi/4$ from the *Oz* axis
However, these results should be considered as qualitative Since our two-dimensional approach to the solution of the Laplace equation implies a revolution symmetry of the solution with respect to the *Oz* axis, the three-dimensional representation of the downstream metal layer defect depicted in Fig 10 would be a circular groove, rather than a pinhole Thus, the flux of gas which is allowed to cross the MPM will be overestimated Reliable results in *Case III* could only be obtained as part of a consistent three-dimensional approach

Conclusions. The FDA calculations used in order to solve the two-dimensional Laplace equation for $c(z,r)$, yielded some interesting results concerning the permeation of gases through MPM.

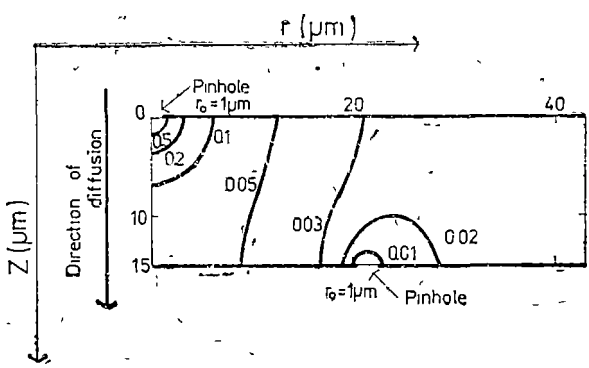

Fig 10 Calculated normalized concentration profiles for the permeation of gases through an MPM in *Case III*.

Taking into account the features of the metal layer deposited onto the polymeric substrate, the geometrical parameters of the MPM and the thermodinamic working conditions, there have been determined with satisfactory accuracy the fluxes of gas which permeate through an MPM.

At the present stage of development of our theoretical model, it seems that the relative discrepancies between the theoretical and the experimental data, besides the causes already mentioned, might be due to the insufficient accuracy in the determination of the pinhole distribution according to size. As discussed in [10], this distribution has been established for a 30 cm^2 MPM from a 5×5 mm area

The concentration profiles of Figs 3, 9 and 10 validate the assumption that the penetrant gas does not diffuse beyond the cylindrical boundary of a single-pinhole MPM Generally, the gas concentration at this boundary is very low, less than 1% from its largest value, c_2

From Fig 4 one may draw a conclusion with a practical value the improvement ratio for the permeability of an MPM, with many large pinholes, may be increased by increasing the polymer membrane thickness. However, the gas flux does not decrease proportional to the increase of l.

Figs 6, 7 and 8 demonstrate that the barrier properties of the polymeric substrate immediately beneath the metal coating are critical in determining the permeability of the MPM. As discussed in [7], under some circumstances, the barrier properties of this part of the polymer membrane may be made dissimilar to the bulk of the MPM For example, where the membrane is laquered with a less permeable material and then metallized over the laquer, one can reduce drastically the rate of gas transfer through the MPM On the other hand, when there is a thin coating, made of a more permeable polymer, on the polymeric substrate, then the flux of gas which permeates through the MPM can also be altered

REFERENCES

1 L Holland, "Vacuum Deposition of Thin Films", Chapman & Hall, London, 1956, pp. 358–381
2 F G Arroyo, *Boletin Soc Espanola de Ceram y Vidrio*, **14,** 145 (1975)
3 J Spiinger, F Forster, S L Hadiwinoto, „Beitrage zur Galvanisierung von Polymeren", *Die Angew Makromolek Chem*, **130,** 179 (1985)
4 "Jonergin Product Catalogue", St Albanas, Vermont, 1984
5 "Safidief Product Catalogue", Paris, 1980
6 P Mercea, L Mureşan, V Mecea, "Permeation of Gases through Metallized Polimer Membranes", *J Membrane Sci*, to appear
7 E H H Jamieson, A H Windle, "Structure and Oxygen-Barrier Properties of Metallized Polymer Films", *J Mater Sci*, **18,** 64 (1983)
8 M M Gudimov, Ju V Jerdev, A V Koriolin, V A Kozlov, "The Influence of Polymer Metallization on the Gas Permeability (in russian), *Fiz Khim Mekh Mater*, **7,** 59 (1971)
9 D H W Carstens, E P Ehart, "Permeability of Deuterium and Helium in Poly (vinyl alcohol)", *J Appl Polym Sci*, **29,** 261 (1984)
10 P Mercea, L Mureşan, V Mecea, D Silipaş, I Ursu, "Permeation of Gases through a Poly (ethylene terephtalate) Membrane Metallized with Palladium", *J Membr Sci*, to appear

11. P Mercea, *Ph D Diss*, "The Selective Transport of Gases through Polymer Membranes", Univ of Bucharest, Bucharest, 1986
12. W. Prins, J J Hermans, "Theory of Permeation through Metal Coated Polymer Films", *J Phys Chem*, **63,** 716 (1959)
13 R M Felder, G S Hurard, in R A Fara (Ed), "Methods of Experimental Physics, Polymers", Part C *Physical Properties*, Vol 16, Academic Press, New York, 1980, pp 316—319
14 R M Barrer, "Diffusion in and through Solids", University Press, Cambridge, 1951, p 6.
15. S A Stern, H L Frisch, "The Selective Permeation of Gases through Polymers", *Ann Rev Mater Sci*, **11,** 523 (1981)
16. T.A Beu, F Spineanu, M Vlad, R I Câmpeanu, I I Popescu, "TOPIC — Tokamak Plasma Impurities Code", *Comput Phys Commun*, **36,** 161 (1985)

STUDIA UNIV. BABEŞ-BOLYAI, PHYSICA, XXXV, 1, 1990

GENERALIZATION OF LAGRANGE'S EQUATIONS OF THE FIRST KIND

CONSTANTIN TUDOSIE*

Received: January 25, 1990

ABSTRACT. — In this paper Lagrange's equations of the first kind are generalized with the aim to establish a system of equations that allow to determine the higher order accelerations, by determining their solutions The established integro-differential equations yield, Lagrange's equations for $n = 3$

1. Introduction. The higher order accelerations occur directly in the dynamics of all complex phenomena with a very fast evolution Their determination by the method of successive derivations most ofen leads to great difficulties of mathematical calculation. A direct method to determine these accelerations, of any order $n > 2$, is possible by passing from the differential equations of the classical mechanics to the equations of the mathematical physics.

In this paper, Lagrange's equations of the first kind are generalized with the purpose of establishing a system of equations in which the higher order accelerations might be obtained by determining their solutions. For the order of the acceleration coinciding with the order of the derivative, x is called zero order acceleration, and x first order acceleration.

2. Establishment of the equations. It is known that in vectorial form Lagrange's equations of the first kind are [3]

$$m_i \ddot{\bar{r}}_i = \bar{F}_i\,(t,\ \bar{r}_i, \dot{\bar{r}}_i) + \sum_{j=1}^{h} \lambda_j \nabla_i f_j, \tag{1}$$

$$(i = 1, 2, 3, \ldots, N),$$

where

$$\nabla_i = \bar{i}\,\frac{\partial}{\partial x_i} + \bar{j}\,\frac{\partial}{\partial y_i} + \bar{k}\,\frac{\partial}{\partial z_i},$$

is "the nabla operator" and $\lambda_j(t)$ — "Lagrange's multiplications". System (1) and Eqs (2) describe the motion

$$f_j(t, \bar{r}_1, \bar{r}_2, \ldots, \bar{r}_N) = 0, \tag{2}$$

$$(j = 1, 2, 3, \ldots, h).$$

In the scalar form, (1) and (2) make up a system (Q) of $3N + h$ equations with the same number of unknown functions $\{x_i(t),\ y_i(t),\ z_i(t),\ \lambda_j(t)\}$.

* *Polytechnic Institute, 3400 Cluj-Napoca, Romania*

The second order accelerations are written under the form:

$$\ddot{\bar{r}}_i = \sum_{\sigma=0}^{n-3} \overset{(2+\sigma)}{\bar{r}_i}(0)\frac{t^{(\sigma)}}{\sigma_1} + \int_0^t \frac{(t-s)^{n-3}}{(n-3)!}\bar{\varphi}_{i,n}(s)\,ds, \tag{3}$$

where

$$\overset{(n)}{\bar{r}_i} = \bar{\varphi}_{i,n}(t), \quad (i = 1, 2, 3, \ldots, N), \quad (n = 3, 4, 5, \ldots).$$

From (1) and (3) it follows

$$\bar{E}_{i,n}(t, \bar{r}_i, \dot{\bar{r}}_i) - \int_0^t K_n(t, s)\bar{\varphi}_{i,n}(s)\,ds = \bar{0}, \tag{4}$$

$$(i = 1, 2, 3, \ldots, N), \quad (n = 3, 4, 5, \ldots),$$

where

$$K_n(t, s) = \frac{(t-s)^{n-3}}{(n-3)!},$$

$$\bar{E}_{i,n}(t, \bar{r}_i, \dot{\bar{r}}_i) = (m_i)^{-1}\left[\bar{F}_i(t, \bar{r}_i, \dot{\bar{r}}_i) + \sum_{j=1}^{h}\lambda_j\nabla_i f_j\right] - \sum_{\sigma=0}^{n-3}\overset{(2+\sigma)}{\bar{r}_i}(0)\frac{t^\sigma}{\sigma!}.$$

The integro-differential equations (4) represent "the generalization of Lagrange's equations" of the first kind, in vectorial form. In scalar form, "the generalization of Lagrange's equations" results from (4), [2]

$$\begin{cases} X_{i,n}(t, x_i, \dot{x}_i) - \int_0^t K_n(t, s)\, x_{i,n}(s)\,ds = 0, \\ Y_{i,n}(t, y_i, y_i) - \int_0^t K_n(t, s)\, y_{i,n}(s)\,ds = 0, \\ Z_{i,n}(r, z_i, \dot{z}_i) - \int_0^t K_n(t, s) z_{i,n}(s)\,ds = 0, \end{cases} \tag{5}$$

$$(i = 1, 2, 3, \ldots, N), \quad (n = 3, 4, 5, \ldots),$$

where

$$X_{i,n}(t, x_i, \dot{x}_i) = (m_i)^{-1}\left[X_i(t, x_i, \dot{x}_i) + \sum_{j=1}^{h}\lambda_j\frac{\partial f_j}{\partial x_i}\right] - \sum_{\sigma=0}^{n-3}\overset{(2+\sigma)}{x_i}(0)\frac{t^\sigma}{\sigma!},$$

$$Y_{i,n}(t, y_i, y_i) = (m_i)^{-1}\left[Y_i(t, y_i, y_i) + \sum_{j=1}^{h}\lambda_j\frac{\partial f_j}{\partial y_i}\right] - \sum_{\sigma=0}^{n-3}\overset{(2+\sigma)}{y_i}(0)\frac{t^\sigma}{\sigma!},$$

$$Z_{i,n}(t, z_i, \dot{z}_i) = (m_i)^{-1}\left[Z_i(t, z_i, \dot{z}_i) + \sum_{j=1}^{h}\lambda_j\frac{\partial f_j}{\partial z_i}\right] - \sum_{\sigma=0}^{n-3(2+\sigma)}\overset{}{z_i}(0)\frac{t^\sigma}{\sigma!}.$$

The equations associated to Eqs. (5) result from (2)

$$f_j(t, x_1, y_1, z_1, x_2, y_2, z_2, \ldots, x_N, y_N, z_N) = 0, \quad (j = 1, 2, 3, \ldots, h). \tag{6}$$

In vectorial form, Lagrance's equations (1) are obtained from the general ones (4), for $n = 3$ The problem of the higher order accelerations ($n = 3, 4, 5, \ldots$) can be solved by Eqs (5) and (6).

3. Application. Let us determine the fourth order acceleration of a heavy point, of mass m, mobile without friction on a plane which rotates with the constant angular velocity ω about the horizontal axis Ox, contained in the plane At the initial moment, $t = 0$, the mobile plane is horizontal, with conditions $x(0) = x_0,\ y(0) = y_0,\ z(0) = 0, \dot{x}(0) = 0,\ y(0) = \frac{g}{2\omega},\ \dot{z}(0) = 0$

Solution From the equation of the mobile plane

$$f(t,y,z) = y \sin \omega t - z \cos \omega t = 0, \tag{7}$$

it follows

$$\frac{\partial f}{\partial x} = 0,\ \frac{\partial f}{\partial y} = \sin \omega t,\ \frac{\partial f}{\partial z} = -\cos \omega t. \tag{8}$$

Considering the Cartesian trihedron $Oxyz$ with the axis Oz vertically ascendant, the differential equations of the motion of heavy point are

$$\ddot{x} = 0;\ m\ddot{y} = \lambda \sin \omega t,\quad m\ddot{z} = -(mg + \lambda \cos \omega t) \tag{9}$$

For $i = 1$ and $n = 4$, Eqs. (5) become

$$\begin{cases} A_4(t) - \int_0^t K_4(t, s)\, x_4(s)\, ds = 0, \\ B_4(t, \lambda) - \int_0^t K_4(t, s)\, y_4(s)\, ds = 0, \\ C_4(t, \lambda) - \int_0^t K_4(t, s)\, z_4(s)\, ds = 0, \end{cases} \tag{10}$$

where

$$K_4(t, s) = t - s,$$

$$A_4(t) = -\sum_{\sigma=0}^{1} x^{(2+\sigma)}(0)\, \frac{t^\sigma}{\sigma!}, \tag{11}$$

$$B_4(t, \lambda) = (m)^{-1} \lambda \sin \omega t - \sum_{\sigma=0}^{1} y^{(2+\sigma)}(0)\, \frac{t^\sigma}{\sigma!}, \tag{12}$$

$$C_4(t, \lambda) = -(m)^{-1}\ (mg + \lambda \cos \omega t) - \sum_{\sigma=0}^{1} z(0)^{(2+\sigma)} \frac{t^\sigma}{\sigma!}\ . \tag{13}$$

By substituting (9) in the second order derivative of Eq. (7), one obtains

$$\lambda(t, y, \dot{z}) = -m\ [g \cos \omega t + 2\omega\ (y \cos \omega t + \dot{z} \sin \omega t)] \tag{14}$$

By eliminating $\dot{z}$ between Eq (7) and its first derivative, it follows

$$y\ (t, y, y) = -m\left[g \cos \omega t + 2\omega \left(\frac{y}{\cos \omega t} + \omega y \frac{\sin \omega t}{\cos^2 \omega t}\right]\right). \tag{15}$$

By substituting (15) in (12), one obtains

$$D_4(t, y, y) = -\left[\frac{g}{2} \sin 2\omega t + 2\omega(yt g\omega t + \omega y t^2 g\omega t) + \sum_{\sigma=0}^{1} y(0)^{(2+\sigma)} \frac{t^\sigma}{\sigma!}\right] \tag{16}$$

By eliminating y between Eq (7) and its first derivative, it follows

$$\lambda(t, z, \dot{z}) = -m\left[g \cos \omega t + 2\omega \left(\frac{\dot{z}}{\sin \omega t} - \omega z \frac{\cos \omega t}{\sin^2 \omega t}\right)\right]. \tag{17}$$

By substituting (17) in (13), one obtains

$$G_4(t, z, \dot{z}) = -g \sin^2 \omega t + 2\omega\ (\dot{z} \operatorname{ctg} \omega t - \omega z \operatorname{ctg}^2 \omega t) - \sum_{\sigma=0}^{1} z(0)^{(2+\sigma)} \frac{t^\tau}{\sigma!}\ . \tag{18}$$

The accelerations $y^{(i)}$ and $z^{(i)}$, $(i = 0, 1)$ are written under the form

$$y(t) = \sum_{\sigma=0}^{3} y^{(\sigma)}(0) \frac{t^\sigma}{\sigma!} + \int_0^t H_4\ (t, s)\ y_4\ (s)\ ds, \tag{19}$$

$$y(t) = \sum_{\sigma=0}^{2} y(0)^{(1+\sigma)} \frac{t^\sigma}{\sigma!} + \int_0^t Q_4\ (t, s)\ y_4\ (s)\ ds, \tag{20}$$

$$z(t) = \sum_{\sigma=0}^{3} z^{(\sigma)}(0) \frac{t^\sigma}{\sigma!} + \int_0^t H_4(t, s)\ z_4\ (s)\ ds, \tag{21}$$

$$\dot{z}(t) = \sum_{\sigma=0}^{2} z(0)^{(1+\sigma)} \frac{t^\sigma}{\sigma!} + \int_0^t Q_4\ (t, s)\ z_4\ (s)\ ds, \tag{22}$$

where

$$H_4\ (t, s) = \frac{(t-s)^3}{6}\ , \quad Q_4(t, s) = \frac{(t-s)^2}{2}\ .$$

By substituting (19) — (22) in (16) and (18), it follows

$$L_4(t) = -\left\{\frac{g}{2}\sin 2\omega t + \sum_{\sigma=0}^{1} \overset{(2+\sigma)}{y}(0)\frac{t^\sigma}{\sigma!} + 2\omega \operatorname{tg}\omega t\left[\sum_{\sigma=0}^{2} \overset{(1+\sigma)}{y}(0)\frac{t^\sigma}{\sigma!} + \omega \operatorname{tg}\omega t \sum_{\sigma=0}^{3} \overset{(\sigma)}{y}(0)\frac{t^\sigma}{\sigma!}\right] + \right.$$

$$\left. + \int_0^t \omega \operatorname{tg}\omega t\left[(t-s)^2 + 2\omega \operatorname{tg}\omega t \cdot H_4(t, s)\right] y_4(s)\, ds\right\}. \tag{23}$$

$$P_4(t) = -g\sin^2\omega t - \sum_{\sigma=0}^{1} \overset{(2+\sigma)}{z}(0)\frac{t^\sigma}{\sigma!} + 2\omega \operatorname{ctg}\omega t\left[\sum_{\sigma=0}^{2} \overset{(1+\sigma)}{z}(0)\frac{t^\sigma}{\sigma!} - \omega \operatorname{ctg}\omega t \sum_{\sigma=0}^{3} \overset{(\sigma)}{z}(0)\frac{t^\sigma}{\sigma!}\right] +$$

$$+ \int_0^t \omega \operatorname{ctg}\omega t\left[(t-s)^2 + 2\omega \operatorname{ctg}\omega t H_4(t, s)\right] z_4(s)\, ds \tag{24}$$

Taking into account (23) and (24), system (10) becomes

$$\begin{cases} A_4(t) - \int_0^t K_4(t, s)\, x_4(s)\, ds = 0, \\ U_4(t) - \int_0^t N_4(t, s)\, y_4(s)\, ds = 0, \\ V_4(t) - \int_0^t S_4(t, s)\, z_4(s)\, ds = 0, \end{cases} \tag{25}$$

where

$$U_4(t) = -\left\{\frac{g}{2}\sin 2\omega t + \left[\sum_{\sigma=0}^{1} \overset{(2+\sigma)}{y}(0) + 2\omega \operatorname{tg}\omega t \sum_{\sigma=0}^{2} \overset{(1+\sigma)}{y}(0) + 2\omega^2 \operatorname{tg}^2 \omega t \sum_{\sigma=0}^{3} \overset{(\sigma)}{y}(0)\right]\frac{t^\sigma}{\sigma!}\right\}, \tag{26}$$

$$V_4(t) = -g\sin^2\omega t - \left[\sum_{\sigma=0}^{1} \overset{(2+\sigma)}{z}(0) - 2\omega \operatorname{ctg}\omega t \sum_{\sigma=0}^{2} \overset{(1+\sigma)}{z}(0) + 2\omega^2 \cdot \operatorname{ctg}^2 \omega t \sum_{\sigma=0}^{3} \overset{(\sigma)}{z}(0)\right]\frac{t^\sigma}{\sigma!}, \tag{27}$$

$$N_4(t, s) = K_4(t, s) + \omega \operatorname{tg}\omega t K_4^2(t, s)\left[1 + \frac{\omega}{3}\operatorname{tg}\omega t K_4(t, s)\right], \tag{28}$$

$$S_4(t, s) = K_4(t, s) + \omega \operatorname{ctg}\omega t K_4^2(t, s)\left[1 + \frac{\omega}{3}\operatorname{ctg}\omega t K_4(t, s)\right]. \tag{29}$$

By making use of (14) and the derivatives $\dot{\lambda}$ and $\ddot{\lambda}$, from the Eqs. (9) it follows directly and by derivation, for $t = 0$, the constants

$$\overset{(\sigma)}{x}(0) = 0,\ (\sigma = 2, 3, 4),\ \dddot{y}(0) = 0,\ \ddddot{y}(0) = -2\omega g,$$

$$y_4(0) = 0,\ \dddot{z}(0) = g,\ \pm\ddddot{z}(0) = 0,\ z_4(0) = -4\omega^2 g.$$

Eqs (25) are "Volterra type linear integral equations" of the first kind [4].

Determination of the solution of equations (25) The solution of the first equation in (25) is $x_4(t) = 0$, which also results from the first equation in (9). The second and the third equations in (25) are solved by a method of numerical integration On the interval $[0, a]$, $a > 0$, one applies a method analogous to that of the polygonal lines The interval $[0, a]$ is divided through the points $t_k = k\frac{a}{m}$, $k = \overline{1, m}$, by using the quadrature formula [5], [6]

$$\int_0^{k\frac{a}{m}} f(s)\,ds \approx \frac{a}{m}\sum_{\nu=1}^{k} f\left(\nu\frac{a}{m}\right), \quad (k = 1, 2, 3, \ldots, m),$$

for the approximate calculation of the integrals For the second and the third equations in (25) systems (Q_1) and (Q_2) are obtained, having m algebric equations with m unknown quantities

$$U_4\left(k\frac{a}{m}\right) - \frac{a}{m}\sum_{\nu=}^{k} N\left(k\frac{a}{m}, \nu\frac{a}{m}\right) y_4\left(\nu\frac{a}{m}\right) = 0, \tag{30}$$

$$V_4\left(k\frac{a}{m}\right) - \frac{a}{m}\sum_{\nu=1}^{k} S_4\left(k\frac{a}{m}, \nu\frac{a}{m}\right) z_4\left(\nu\frac{a}{m}\right) = 0, \tag{31}$$

$$(k = 1, 2, 3, \ldots, m).$$

The unknown quantities **of** the two systems are

$$y_4\left(\frac{a}{m}\right), y_4\left(2\frac{a}{m}\right), \ldots, y_4(a),$$

$$z_4\left(\frac{a}{m}\right), z_4\left(2\frac{a}{m}\right), \ldots, z_4(a)$$

The variation diagrams of the functions $y_4(t)$ and $z_4(t)$, constructed through the points t_k, $(k = \overline{1, m})$, represent the graphical approximation of the solution of the two equations in (25), on the interval $[0, a]$, $a > 0$

In numerical values, the solution of systems (30) and (31) is determined by the known methods [1]

The module of the fourth order acceleration of the heavy point is

$$|\bar{a}_4(t)| = [y_4^2(t) + z_4^2(t)]^{\frac{1}{2}},$$

and vectorially

$$\bar{a}_4(t) = y_4(t)\bar{j} + z_4(t)\bar{k},$$

$\bar{i}, \bar{j}, \bar{k}$ being the unit vectors of the Cartesian trihedron **Oxyz.**

REFERENCES

1 B Démidovitch, I Maron, "Eléments de calcul numerique", Ed Mir, Moscou, 1973

2 M Ghermănescu, „Ecuaţiile fizicii matematice", Ed de Stat didactică şi pedagogică, Bucureşti, 1961

3 C Iacob, „Mecanică teoretică", E D P , Bucureşti, 1971

4 T Lalescu, „Introducere la teoria ecuaţiilor integrale", Ed Acad , 1956

5 C Tudosie, "Deduction of higher order accelerations by the method of associated angular velocity", *Strojnicky Časopis*, **34**, 1983, č 3, 337—342

6. C Tudosie, "Determination of higher order accelerations by a functional method", *Acta Technica ČSAV*, **2**, 218—224, 1983

STUDIA UNIV BABEŞ-BOLYAI, PHYSICA, XXXV, 1, 1990

ON THE ELECTRONIC STRUCTURE OF La_2CuO_4

V. CRIŞAN*, A. JÁNOSI*, D. KAPUSI*, C. POPOVICIU*, V. POPESCU*, K. MOSTIŞ and A. VÁSÁRHELYI*

Received September 12, 1989

ABSTRACT — Using the Haydock recursion method the density of states for the La_2CuO_4 high T_c superconductor was computed The results are in agreement partly with the band structure calculations — the peak just below the Fermi level and partly with the cluster-type calculation — the gap in the density of states on Cu atoms

Before starting any discussion on the mechanism of superconductivity in the high T_c's, one of the most basic question one must address concerns their electronic structure and the nature of the states at the Fermi level when the oxygen stoichiometry is changed and some atoms are replaced by others

Several reports of the application of band theory to the new copper oxides have already appeared [1—5]. While several aspects of the band structures of the 2—1—4 system [1—5] correlate well with experimental data such as the Fermi surface nesting [1, 2], the position of the van Hove singularity with a rigid band model for T_c [3] the transport properties and the anisotrop of the Fermi velocities [6], some discrepances have been noted Leung, Wang and Harmon [7] and Sterne et al. [8] have failed to produce a stable antiferromagnetic ground state within the local spin density approximation

On the other hand, recent experiments have revealed several new aspects The photoemission experiments have confirmed a strong Coulomb repulsion about 7 ev at Cu-site [9—11] A basic question is that the high T_c' s belong or not to the class of strongly correlated systems.

The d density of states (DOS) in the high T_c 's is spread out over a large energy range, 6—7 eV, suggesting that for these states the band width may be small compared to the Coulomb interaction However, if the band structure is investigated one can see that the broad density of states results to a large extent from splittings due to the crystal field and not to the translational symmetry In these systems the Coulomb and the exchange interactions, the O(2p) — Cu (3d) hybridisation, the multiplet structure and the crystal field splitting are important [12, 13]

Better approaches to describe the electronic structure of these systems are impurity and cluster configuration interaction model calculations [14, 15]

Assuming that superconductivity in the high T_c materials takes place in the CuO_2 planes, one then studies a Cu impurity in an oxygen band or a cluster of the type $(CuO_4)^{6-}$, $(CuO_5)^{8-}$ or $(CuO_5)^{10-}$

* *University of Cluj Napoca, Department of Physics, 3400 Cluj Napoca, Romania*

Because there is a large number of similarities between CuO and high T_c's, in many papers CuO is considered as a model material for the high T_c compounds [17].

Results and Discussions. The density of states (DOS) for the ideal La_2CuO_4 compound was calculated with parameters

$$\varepsilon\,(x^2 - y^2) = 0 \qquad \varepsilon\,(p_x) = 0$$

$$t = -1 \cdot 6\,eV$$

the obtained results being shown is Figs 1 and 2 For $\varepsilon(3z^2 - r^2) = 0$ an important maximum in DOS has appeared at the Fermi level which was done by the out of plane (apex) oxygens The DOS for Cu $(3z^2 - r^2) = 0$ has two peaks, the Fermi level being on the highest in energy peak

The Cu $(x^2 - y^2)$ orbital has a very small contribution to the DOS at the Fermi level. The in plane oxygen has two large peaks in the same region as the Cu $(x^2 - y^2)$ DOS and a sharp peak at about 1 5 eV below the Fermi level One can see from Fig 2a that the system has a metallic character

For $\varepsilon\,(3z^2 - r^2) = -1$ eV, the DOS for Cu $(x^2 - y^2)$ and in-plane oxygen remain unchanged, the apex oxygen has a sharp maximum at the Fermi level

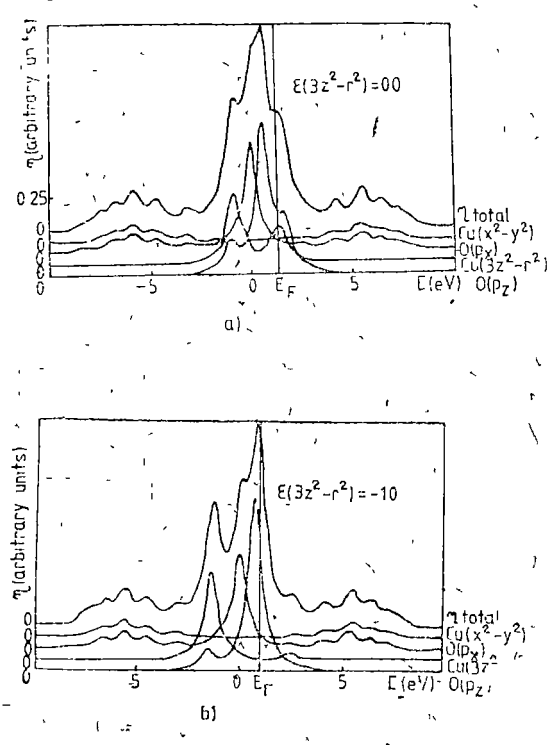

Fig 1.

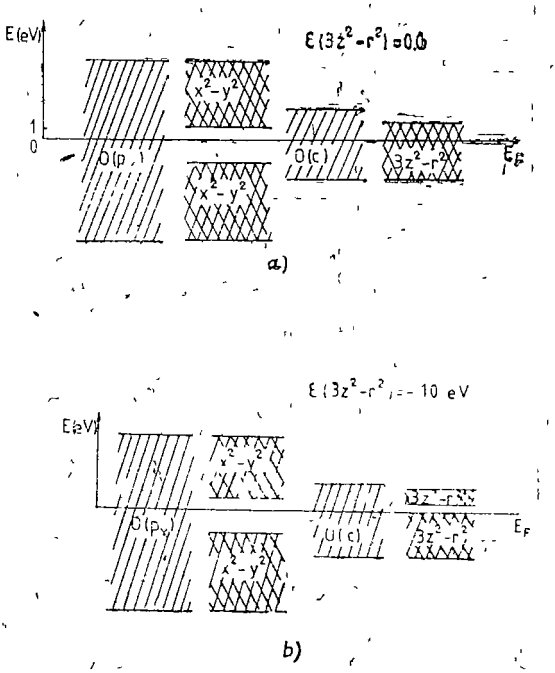

Fig. 2.

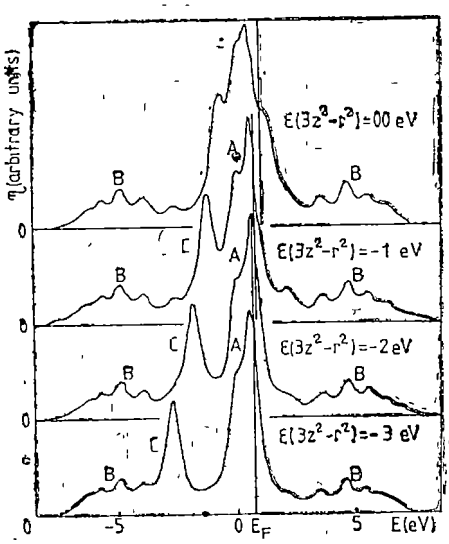

Fig 3

and the Cu $(3z^2 - r^2)$ has a gap at the Fermi level as one can see from Figs 1b and 2b. The Fermi level shifts towards the lower energy

The changes in the shape of DOS when $\varepsilon(3z^2 - r^2)$ is varying are shown in Fig 3. The A peak becomes sharper and starting with $\varepsilon(3z^2 - r^2) = -1$ eV a new peak C appears, which is shifted to the lower energies when $\varepsilon(3z^2 - r^2)$ is decreased (Fig 4) The peaks B remain unchanged One can see from Fig 4 that starting with $\varepsilon(3z^2 - r^2) = -2$ eV DOS for Cu $(3z^2 - r^2)$ has no contribution above the Fermi level From this model one can see that the correlation effect can be simulated considering two orbitals on Cu atom and one orbital for each plane and apex oxygens.

The obtained results are in agreement with the band structure theory having a peak just below the Fermi level and at the same time in agreement with clusters-type calculation in which the DOS for copper atoms has a gap at the Fermi level.

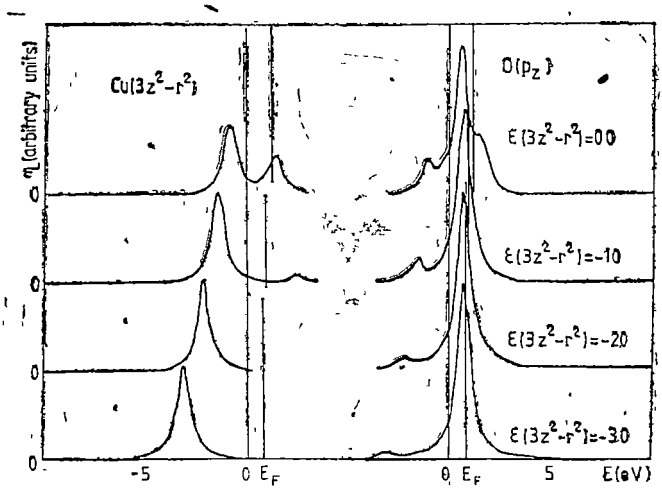

Fig. 4

REFERENCES

1 L F Mattheiss, *Phys Rev Lett*, **58,** 1028 (1987)
2 J Yu, A J Freeman, J H Xu, *Phys Rev Lett* **58,** 1035 (1987)
3, W E Pickett, H Krakauer, D A Papaconstantopoulos, L L Boyer, *Phys Rev*, **B35,** 7252 (1987)
4 T Fuginara, Y Hatsugai, *Jpn J Appl Phys*, **36,** L716 (1987)
5 R V Kasowski, W Y Hsu, F Herman, *Solid State Commun* **63,** 1077 (1987)
6 P B Allen, W E Pickett, H Krakauer, *Phys Rev* **B36,** 3926 (1987)
7 T C Leung, X W Wang, B N Harmon, *Phys Rev* **B37,** 387 (1988)
8 P.A Sterne, C S Wang, G M Stokes, W A Temmer man, MRS Symp Proc Boston, 1987
9 T Takahashi, M Maeda, H Arai, H Katayama-Yoshida, Y Okabe, T Suzuki S Hosoya, A Fujimori, T Shidara, T Koide, T Maya-kura, M Onoda, S Shamoto, M Sato, *Phys Rev* **B36,** 5686 (1987)
10 Zhi-Xun Shen et al *Phys Rev* **B36,** 8414 (1987)
11 F Milla, *Phys Rev* **B38,** 11358 (1988)
12 H Eskes, H Tjeng, G A Sawatzky, "Materials Science", vol **11**, 1989, p 20.
13 G A Sawatzky, *int J Mod Phys* **B1,** 779 (1988)
14 A Fujimori, F Mihami, *Phys Rev* **B30,** 957 (1984)
15 G A Sawatzky, J-W Allen, *Phys Rev Lett*, **53,** 2339 (1984)
16 J Zaanen, G A Sawatzky, J W Allen, *Phys Rev Lett* **55,** 418 (1985)
17. H Eskes, L H Tjeng, G A Sawatzky, preprint

STUDIA UNIV BABEŞ-BOLYAI, PHYSICA, XXXV, 1, 1990

OXIGEN—VACANCY ORDERING AND DENSITY OF STATES IN $YBa_2Cu_3O_{7-y}$

V. CRIŞAN*, Z. NEUFELD*, K. MOSTIŞ*, A. LUPULESCU* and A. JÁNOSI*

Received October 17,1989

ABSTRACT — Using Haydock recursion-method the density of states for the ordered vacancies model of Alario Franco for $YBa_2Cu_3O_{7-y}$ was computed With the oxygen vacancies concentration the changes of the shape of the density of states was observed Due to isolated units of Cu—O—Cu from the chains, for $y \geq 0.25$ at $E-E_F \sim 4eV$, a sharp peak in the density appeared, in qualitative agreement with optical experiments

The high temperature superconducting materials prepared to date contain, in varying degrees, structural disorder, manifested as [1] grain boundaries or extended defects or [2] compositional disorder associated with random atomic substitution, oxygen vacancies, spinodal decomposition etc In particular, $YBa_2Cu_3O_{7-y}$ has been shown to exist in a large compositional range extending between $YBa_2Cu_3O_6$ and $YBa_2Cu_3O_7$.

It was shown that the oxygen stoichiometry changes the superconducting temperature from about 93K for $y = 0$ to 60 K at $y = 0.5$ If the oxygen deficiency is larger, the superconducting properties vanishes [1], the materials are antiferromagnets with Neel temperature increasing with y [2], the higher value, 500 K, being reported for $y = 1$ Other reported results show that the slow extraction of oxygen at about 600 °C the orthorhombic superconducting phase can exist down to at least $y = 0.7$ [1]

The oxygen vacancies also affect other properties of these materials For instance, the dependence of resistivity on the oxygen content at 120 K shows an increase with the increase of y probably due to the decrease of the carrier density [3, 4] The maximum in resistivity was achieved probably because of orthorhombic to tetragonal transition

The thermal conductivity for $y = 0$ analogous to that of ordinary superconductors contaminated by impurities [5] in which the general part of the thermal conductivity is due to the phonons scattered mainly by the electrons. It was found that χ decreases with increasing of y at any temperature above T_c The maximum at 120 K at the same value of y as for the resistivity and for the thermoelectric power has been found. It was done by the structural transition from the orthorhombic to tetragonal lattice at about $y = 0.6$, or by the Mott transition due to the small carrier density and disorder in the oxygen vacancies distribution.

Using O—K_αX ray emission and Cu—L X—ray self-absorption spectroscopy F. Burgazy et al [5] showed that the valency of copper depends strongly on the oxygen content.

* *University of Cluj-Napoca, Department of Physics, 3400 Cluj-Napoca, Romania*

At the same time, the diffusion rate of oxygen in these ceramics depends on y [7] Detailed work by Kishio et al. [30], among others, [4, 6], shows an almost linear dependence of y on oxygen pressure at each temperature.

Structural properties. The first element of the $YBa_2Cu_3O_{7-y}$ series with $y = 0$, crystallizes in the orthorhombic system with the space group Pmmm and lattice parameters $a_0 = 3\,8193$ Å, $b_0 = 3\,8852$ Å and $c_0 = 11\,6873$ Å Because the a and b parameters are quite equal, in the calculations of the density of states we neglect this small distorsion. The end of the series, $y = 1$, has a tetragonal symmetry with the parameters $a_t = 3\,8870$ and $c_t = 11\,8194$ Å. In the 123 oxides the Cu (2) — 0 layers in the $a - b$ plane form a mainly square, two dimensional Cu lattice with oxygen atoms situated midway between each nearest neighbour pair These layers are separated by Y layers that contain no oxygen The Cu (1) — 0 atoms form chains on the b axes between two Ba—0 planes When oxygen is removed from the sample, it is the 0(1) site in the Cu (1) — 0 chains that is depleted For y greater than about 0 5 the layer is further depleted of oxygen, an orthorhombic to tetragonal transition takes place, and superconductivity is lost

Recently, X ray — absorption study [11] has shown that the distances between Cu atoms other from the unit cell increase only slightly from 5 to 600 K, except for the shorter of the two Cu—Ba distance, Cu (2) — Ba, which decreases with increasing temperature, results qualitatively consistent with the structural measurements. Similar features are observed for both orthorhombic and tetragonal samples No significant anomalies are observed versus temperature. The X-ray absorption near-edge structure supports the conclusion that the Cu(1) becomes monovalent as is Cu_2O with a linear O—Cu—O structural configuration and a $3d^{10}$ electronic configuration when y goes from 7 to 6 The valence for $y \sim 0$ consist of a combination of Cu_{II} and Cu_{III}

Khachaturyan and Morris [12] argued that the orthorhombic phase with intermediate concentrations of vacancies in the range 0 to 0 5 is not stable and the system tends towards the two ordered structures ($y = 1$ and $y = 0$). They have proposed a phase diagram according to which an off-stoichiometric compound with $0 < y < 1$ should under equilibrium conditions split into a mixture of the two structures with $y = 1$ and $y = 0$ Also they have allowed for the possibility of this decomposition to proceed through a series of intermediate homologous ordered structures having oxygen stoichiometries $7 - ((n/2n + 1))$ where n is a positive integer Chen et al [8] observed vacancy ordered domains in three dimensions by electron microscopy experiments. Similar domains were observed by Weider et al (13] the dimensions being 100—500 Å along the b direction, 15—50 Å along the a direction and 11 Å [16], or 150 Å [15], along the c direction These domains were estimated to form in about 3 to 10% of the volume samples The above observations were done on prepared oxygen deficient samples without thermal ageing. In the samples with equalibrium structures obtained by thermal ageing the decomposition and ordering were observed for $y = 0\,27$ [8] and $y = 0\,22$ [15] For instance in samples aged 672 hours 15% is in tetragonal phase with $y = 0.85$ the remaing being in orthorhombic phase with $y = 0.11$ [15].

Raveau and coworkers [16] pointed out that in the 123 ceramic oxides there is a mixing of superconductive $YBa_2Cu_2^{II}Cu^{III}O_7$ regions and of insulating regions of $YBa_2Cu_2^{II}Cu^{I}O_6$ and that in average T_c is proportional to the Cu_{III}/Cu_I total ratio.

Based on electron diffraction experiments Alario F Fanco et al [17] proposed ordering oxygen vacancies models for $YBa_2Cu_3O_{7-y}$ where $y = 0$ 125n and $0 \leqslant n \leqslant 8$ For $n = 1, 2$ and 3 the unit cell has the same parameters $a = 2\sqrt{2}a_0$, $b = 2\sqrt{2}b_0$, and $c = 3a_0$, The structures were obtained by elimination of one, out of every eight oxygen atoms of the basal plane for $n = 1$ two and three for $n = 2$ or $n = 3$

For $n = 4$, $(y = 0\,5)$, the consecutive fourth oxygen form the same row were taken and the unit cell parameters became $a = 2a$, $b = b$ and $c = 3a$

For $n = 5$ 6 and 7 the structure was obtained replacing the oxygen atoms by oxygen vacancies and vice-versa the resulting tetragonal unit cells having the parameters $2\sqrt{2}a_t \times 2\sqrt{2}b_t \times c_t$ where subindices "t" refer to the tetragonal cell For $n = 8$, i e for $YBa_2Cu_3O_6$, a tetragonal cell results, corresponding to the total absence of oxygen in the basal plane of the structure with the parameters $a_0 \times a_0 \times 3a_0$

It seems important to notice that the 123 compounds have a structural phase transition at 220 K, which lower the symmetry to Pmm2 as was revealed by ultrasonic measurements [29], and that the orthorhombic to tetragonal transition at 970K is believed to be an order disorder transition [7].

Optical properties. Electron spectroscopy has provided most of the direct information about the electronic configurations in this class of oxides [18—20] From photoelectron spectroscopy, resulted that the density of states at the Fermi level is, surprisingly, very low for all these materials. A valence band is about 5eV wide and is centered at 4 eV below the E_F All of these materials show distinct peaks at 9 5 eV and 12 5 eV. No sharp Fermi edge is observed and the density of states near E_F appears to be consistent with a semiconducting behaviour in the normal state. In $YBa_2Cu_3O_7$ the band centered at 4 eV is decomposed in two features located at 2 3 and 4 5 eV This two components are attributed to Cu 3d and 0 2p features the study of the cross-section of the two valence bands features showed that there are strong covalent interactions between the Cu 3d and 0 2p levels It was reaveled that the Coulomb correlation of Cu 3d holes is about 6 eV. At the same time, it is known that the correlation energy of two 0 2p holes on a single site is greater than 8 eV [21] and on different neighboring ligands is about 4 5 eV These results imply that correlation effects dominate in the YBaCuO that means that one-electron theories of the electronic structure are not able to adequately describe these materials X-ray photoemission and Auger measurements [22] support the same idea A large number of papers reported optical reflectance and ellipsometric measurements [23—27] In YBaCuO7 compound three bands at 2 8, 4 1 and 4 7 eV were found The substitution of Y atoms by other lanthanide atoms do not significant by change the spectra, except for a red shift of the 2 8 eV band with ionic radius of rare earth element With decreasing the oxygen content the 2 8 eV band shifts to lower position and the spectra are

dominated by two rather sharp structures at 1 75 and 4.08 eV. The 4 08 eV decrese linearly in intensity, and shifts to higher energy with increasing the oxygen content At low temperature limit three satellites at 3 95 and 3,73 appear The 1 75 eV band intensity decreases with y, and appers only as a weak shoulder as in the rellectivity measurements [28]

The computational model, results and discussions. The superconducting properties of the this new class seem to be entailed by the special arrangement of copper and oxygen in planes and rows. Itt was shown that the oxygen vacancies appeared in 0(1) positions from the b axis. The oxygen vacancies ordering is a subject of study both of theorethical and experimental points of view Is was shown that for some values of oxigen content, the oxygen vacancies ordering, as a thermodynamical property is not forbidden The experimental evidence, especially that of electron diffraction, shaws an oxygen vacancies ordering and a supercell behaviour.

The density of states was computed for the ordering vacancies model of Alario Franco [17]. Detailed band structure calculations [18] show a remarcable simple band structure near E_F Four bands, cross the Fermi level Two of them, strongly dispersed, consist of Cu2 $(d_{x^2-y^2})$ —O (p_y)—O (p_y) combinations and have a 2D character. The Cu1 $(d_{x^2-y^2})$—O (p_y)—O (p_y) antibonding band shows the 1D dispersion expected from the Cu1—O—CuA linear chains. The Π bonding band formed from the Cu2 $(d_{x^2-y^2})$ —(p_x)—O (p_y) orbitals is almost entirely occupied for the $y = 0$ compound lies just below the Fermi level and gives rise two peaks in the density of states near the E_F, making the density of states at E_F very sensitive for the oxigen vacancies concentrations. Using these informations in order to compute the density of states near the Fermi level, we used only the orbitals involved in the interactions which have contributions at the E_F. At the same time, because the distances d (Cu—O1) = 1.85 Å and d(Cu—02)= 2 303 Å the interaction Cu—02 were neglected, which means that the chains and the planes are enterely decoupled.

In the recursion method the local density of states defined by

$$N(E, R) = |<n|\alpha \vec{R}>| \varphi \delta (E - E_F)$$

where $|n>$ and E are eigenfunctions of the system and $|\alpha R>$ a localized orbita α, located at $\vec{R}$, was computed using the Green function

$$N(e, R) = -\frac{1}{\Pi} Im < \alpha\vec{R} \mid G(E + i0)| \alpha\vec{R}>$$

The ortogonal basis $|n\}$ was generated by means of a recursion algorithm

$$H \mid n\} = a_n|n\} - b_n|n-1\} + b_{n+1}|n+1\}$$

in which

$$|0\} = |0>.$$

A tight binding hamiltonian was used

$$H = \sum_{ij} |i> t_{ij} <j| + \sum_i \varepsilon_i |i> \varepsilon_i <i|$$

where t_{ij} were computed in Slater—Koster approximation The orbitals $|i>$ are $d_{x^2-y^2}$ and $d_{3z^2-r^2}$ for Cu atoms and p_x, p_y or p_z for oxygen atoms. The self energies for the copper atoms were ε (Cu(1)) = 1 1 eV

ε (Cu(2)) = 1 23 eV

ε (0(1)) = ε(0(4)) = ε(0(3)) = 0, Bullet [32]

The diffraction experiments show a low correlation in oxygen vacancies ordering in the c axis That is why in computation we used two independent planes and one chain which have an uncorrelated behaviour

The results are shown in Figs 1 and 2 The Fermi level is moving to higher energies, which shows that as we expected the oxygen vacancies act as dopants The density of states at the Fermi level hase two maxima, one for $y = 0\,250$ and one for $y = 0\,750$ The first maximum appeared because at this concentration of vacancies one Cu atom becomes isolated from other atoms from the chains, which gives a sharp peak in the density of states at E_F.The general feature is that the antibonding states are below the E_F with a small contribution at the E_F and the antibonding states have the maximum in the vecinity of E_F but for $E_F > E$

The density of states for $YBa_2Cu_3O_{7-y}$ are generally in qualitative agreement with band stucture calculations The shape of the DOS for Cu(1), O(1) and O(2) are almost the same in band structure calculations as in our results The Cu(1), O(1) and O(2) started as in the band structure calculations below the Fermi level, the bands having a width of about 8 eV. The peak from π bonding appeares in both methods between —2eV and O

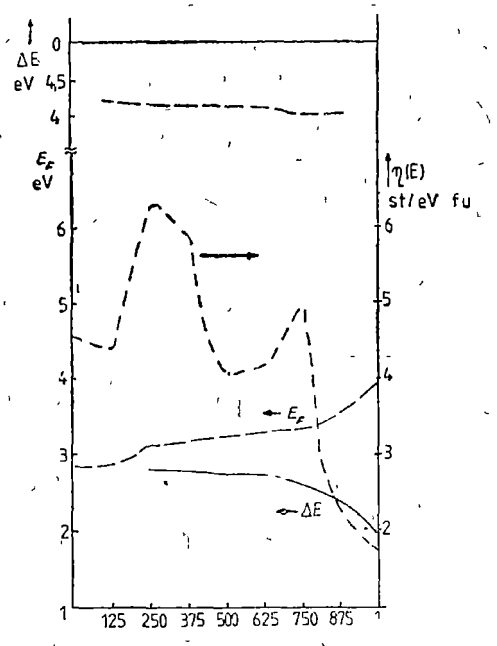

Fig 1.

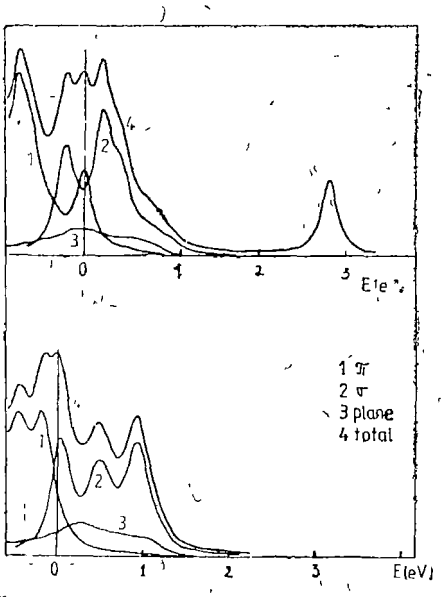

Fig. 2.

One major difference was found The -0.5 eV peak from band structure calculation was not obtained in our calculation, and it seems that our results are in better agreement with Fujimori's optical experiments [19].

As the oxygen vacancies concentration increases a sharp peak at $E-E_F \approx$ $\approx$ 4eV appeares. This peak, which appeared only in compounds with oxygen vacancies increases in intensity as y increases and at the same time shifts to lower energy. Our results, (Fig. 2), in qualitative agreement with optical experiments, show that the isolated units of Cu—O—Cu from the chains are responsible for this.

The density of states at the Fermi level varies with oxygen vacancies concentration, as in Fig. 3 At the same time, the Fermi level shifts towards the higher energy, as the oxygen vacancies increase, in agreement with experimental and theoretical [3] assignments.

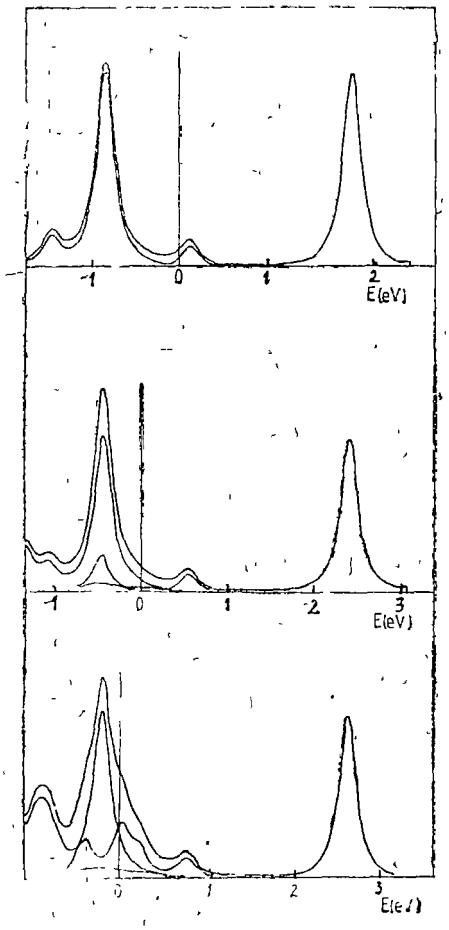

Fig. 3.

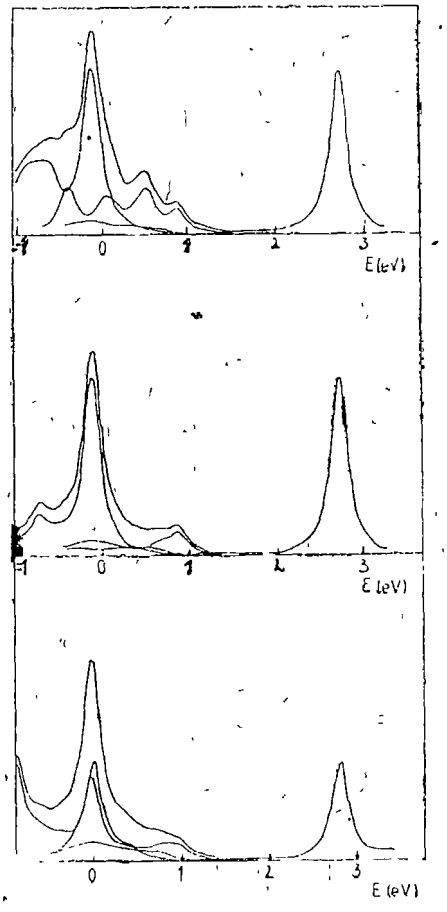

Fig. 4.

REFERENCES

1 R J Cava, B Batlogg, C H Chen, E A Rietman et al, *Nature*, **329**, 423 (1987); *Phys Rev* **B, 36,** 5719 (1987)
2 J M Tranquada et al *Phys Rev Lett* **59,** 1045 (1987), J H Brewer et al, *Phys. Rev. Lett* **60,** 1073 (1988)
3 A V Samoilov, preprint
4 H P Ong, preprint
5 F Burgazy, preprint
6 F Burgazy, *Z Naturfors Ch* **44**a, 180 (1989)
7 K N Tu *Phys Rev* **B39,** 304 (1989)
8 J Jorgensen, M A Beno, D G Hinks, L Sondelholrm, K Volin, R L Hiterman, J D Graco, I K Schuller, C V Segre, K Zhang. *Phys Rev* **B. 36** (10) 5731, (1987)
9 P Strobel, J J Capponi, M Marezio, P Monod, *Solid State Comm* **64** (4), 513 (1987)
10 H M O'Bryan, P K Gallagher, *Solid State Ionics*, in press
11 J B Boyce, F Bridges, T. Claeson, M Nygren, *Phys Rev*, **B39,** 6555 (1988)
12 A G Khachaturyan, J W Morris Jr *Phys. Rev Lett*, **59,** 2776 (1987), *Phys. Rev Lett* **61,** 215, (1988)
13 D J Werder, C H Chen, R J Cava, B Batlogg, *Phys Rev*, **B3,** 5130 (1988)
14 A K Sood et al *Physica* — C **156,** 720 (1988)
15. T S Radhakrishnan et al *Pramana*, in press
16 B Raveau, *Rewnews of Sol St Science*, **2,** 115 (1988)
17 M A Alario—Franco, C Chaillout, J Capponi, J Chenavas, M. Marezio, *Physica*, **C 156,** 455—460 (1988)
18 R L Kurtz et al "Proceedings of first Iberian Vacuum Meeting"
19 A Fujimori et al, *Solid State Commun* **63,** 857 (1987)
20 P Steiner et al, *Z Phys*, **B 67,** 19 (1987)
21 J C Fuggle, J Fink, N Nucker, "Proceedings of the High Tc Superconductivity Conference", Trieste, Ed Y Lu, E Tosatti, et al, World Scientific, Singapore, 1988
22 A Balzarotti et al, *Phys Rev*, **B38,** 6461 (1988)
23 M Garriga et al, *Physica*-C, **153—155,** 643 (1988)
24 J Humlicek et al, *Solid State Commun*, **67,** 589 (1988)
25 M Garriga et al, *Solid State Commun* **66,** 1231 (1988)
26 M K Kelly et al, *Phys Rev Lett* in press
27. M Garriga et al, preprint
28 U Venkateswaran et al, *Phys Rev*, in press (from 19)
29 J. Toulouse, *Phys Rev*, **B38,** 7077 (1988)
30 K Kishio, J Shimoyama, T Hasegawa, K Kitazawa, K Fueki *Jap J Appl Phys*, **26,** 5731, 1987)
31 R Haydock, V Heine, M J Kelly, *J Phys*, **C8,** 2591 (1975), R Haydock *Solid State Physics* (Edited by H. Ehrenreich, F Zeitz, D Turnbull) Vol 35, Academic Press New York, (1980)
32. D W Bullett, W G. Dawson, *J Phys*, **C 20,** 1853 (1987)

STUDIA UNIV. BABEŞ-BOLYAI, PHYSICA, XXXV, 1, 1990

VARACTOR TUNED VAWEGUIDE IMPATT OSCILLATOR DESIGN

D. IANCU and D. STĂNILĂ

Received November 15, 1989

ABSTRACT. — This paper presents a complete calculus method for a varactor tuned IMPATT oscillator We have followed the Eisenhart and Khan calculus method [1], for a single post monture, extended to two posts, one for the IMPATT and the second for the varactor diode The theoretical bandwidth for this oscillator was determined by means of a computer program Experimental we have obtained a 0 3 GHz bandwidth, in good agreement with the experimental value

Theory. It is assumed a rectangular vaweguide structure as shown in Fig. 1. Both the IMPATT and the varactor diodes are disposed along the x axis. Following the Osman procedure [2], the two posts are considered as two coupled antennas. Taking into account the contributions of all the armonic modes, for each n spatial harmonic, a coupling network may be postulated In this way the complet equivalent circuit will consist of an infinit number of such coupling circuits, corresponding to all values of n, from zero to infinit (Fig 2a). The T coupling networks are prefered because of the better physical insight of the problem. In concordance with these, it may be defined the following

Z_{1n} = the series impedance of the T coupling network corresponding to the n-th spatial mode,

Z_{2n} = the shunt arm impedance of the T coupling network,

Z_{1n} and Z are the following expressions

$$Z_{1n} = j\eta \frac{2b}{a} \frac{K^2 - K_y^2}{(2 - \delta_n)K} \sum_{m=2,4,6}^{\infty} \frac{K_{pm}^2 / K_{gn}^2}{\Upsilon_{mn}} \tag{1}$$

$$Z_{2m} = j\eta \frac{b}{a} \frac{K^2 - K_y^2}{(2 - \delta_n)K} \sum_{m=1}^{\infty} (-1)^{m+1} K_{pm}^2 / K_{gn}^2 \tag{2}$$

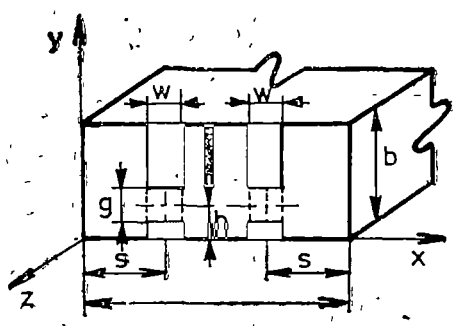

Fig 1 Parallel type varactor-tuned IMPATT oscillator (general structure)

* *University of Cluj-Napoca, Department of Physics, 3400 Cluj-Napoca, Romania*

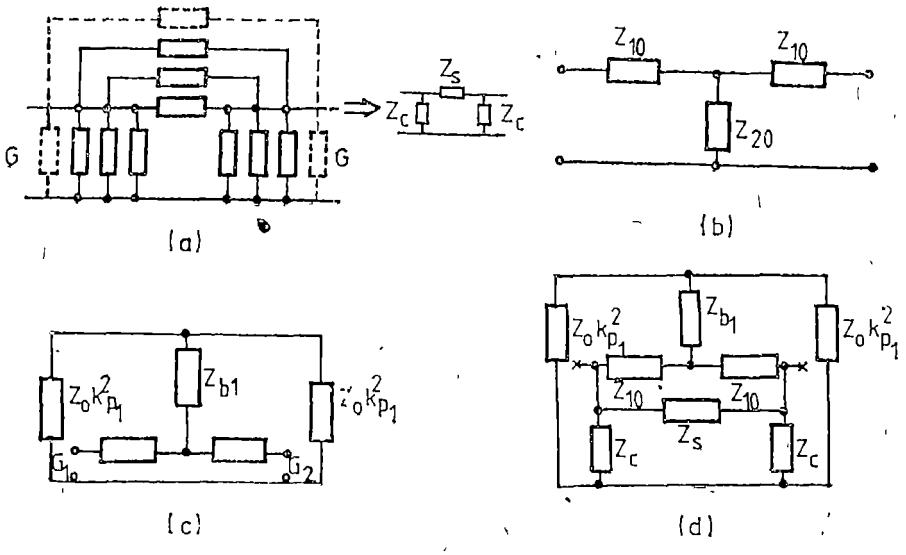

Fig 2 a) π coupling networks for all $n > 0$, b) T network coupling for the two gaps for $n = 0$, c) Rearranged T coupling network for $n = 0$, d) Complet equivalent circuit and the coupling network for all n modes

$$\text{where } K = \frac{2\pi}{\lambda},\quad K_x = \frac{n\pi}{b},\quad K_y = \frac{m\pi}{a},\quad \delta_n = \begin{cases} 1, & \text{for } n = 0 \\ 0, & \text{for } n \neq 0 \end{cases}$$

$$K_{pm} = \sin K_x s \frac{\sin \theta m}{\theta m},\quad K_{gn} = \cos K_y h \frac{\sin \varnothing n}{\varnothing n}, \tag{2}$$

$$\Gamma_{mn} = (K_x^2 + K_y^2 - K^2)^{1/2},\quad \varnothing_n = \frac{n\pi g}{2b},\quad \theta_n = \frac{m\pi\omega}{2a}$$

$$\eta = \sqrt{\frac{\mu_0}{\varepsilon_0}} = 376\,6\,.$$

For the dominant mode TE_{10},

$$Z_{10} = j\eta \sum_{m=2,4,6}^{\infty} \frac{K_{pm}^2}{\Gamma_{m0}} \tag{3}$$

and

$$Z_{20} = \frac{1}{2}\left[\frac{2b}{a}\eta j \frac{K}{\Gamma_{10}}\right] K_{p1}^2 + j\eta \frac{b}{a} \Big] \sum_{m=2}^{\infty} (-1)^{m+1} \frac{K_{pm}}{\Gamma_{m0}} \tag{4}$$

First term of the Z_{20} expression is real and represents half of the characteristic impedance of the guide, referred to the post position as shown in Fig. 2b If it is interpreted as being the parallel combination of the impedances presented by the guide at the plane $Z = 0$ for both directions of propagation the network may be redrawn as in Fig 2c.

According to the above representation this impedance term may be represented as a termination of the mount, this permitting to consider the mount as an obstacle in guide

Using the coupling network presented in Fig 2a, a single network with shunt and series admitances may be obtained as shows Fig 2d, having the following expressions.

$$Y_c = \sum_{n=1}^{\infty} \left(j\eta \frac{b}{a} \frac{K^2 - K_y^2}{K} \sum_{1,3,5}^{\infty} \frac{K_{pm}^2 (K_{gn}^2)}{\Gamma_{mn}} \right)^{-1} \tag{5}$$

$$Y_s = \frac{1}{Z_s} = \sum_{n=1}^{\infty} \left\{ \left(j2\eta \frac{b}{a} \frac{K^2 - K_y^2}{K} \sum_{m=2,4,6}^{\infty} \frac{K_{pm}^2 / K_{gn}^2}{\Gamma_{mn}} \right)^{-1} - \right.$$

$$\left. - \left(j2\eta \left(\frac{b}{a} \frac{K^2 - K_y^2}{K} \sum_{m=1,3,5}^{\infty} \frac{K_{pm}^2 / K_{gn}^2}{\Gamma_{mn}} \right)^{-1} \right. \right. \tag{6}$$

The network presented in Fig 2d, after Δ/Y transformation becomes as may be seen in Fig 3, where

$$Z_a = \frac{Z_{10} Z_s}{2Z_{10} + Z_s} \tag{7}$$

$$Z_{b2} = \frac{Z_{10}^2}{2Z_{10} + Z_s} \tag{8}$$

$$Z_b = Z_{b1} + Z_{b2} \tag{9}$$

where Z is the second term in the expression of Z_{20} considered as an obstacle, the mount impedance is given by.

$$Z_{obs} = \frac{1}{K_{p1}^2} Z_b + \frac{1}{2} \left(Z_a + \frac{Z_c Z_g}{Z_c + Z_g} \right) \tag{10}$$

where Z_g is the impedance of the devices assumed identical In the case when the gaps are open, Z_g will represent the gaps static capacitance

Both for the IMPATT and varactor diodes we used a simplified equivalent circuits represented in Fig 4

Replacing Z_{g1} with equivalent circuit of the IMPATT diode and Z_{g2} with the equivalent circuit of the varactor diode, in the equivalent circuit shown in Fig 3, we will obtain the complete equivalent circuit

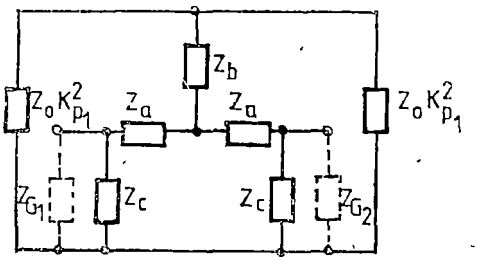

Fig 3 Equivalent circuit after Δ/Y transformation

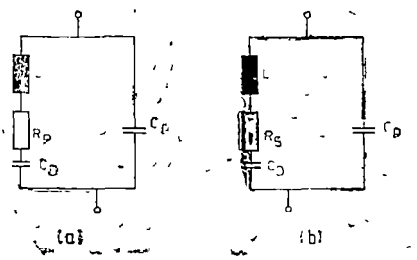

Fig 4 a) Equivalent circuit for IMPATT device, b) Equivalent circuit for varactor device

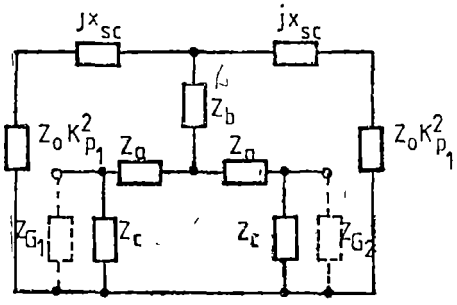

Fig 5 Final equivalent circuit

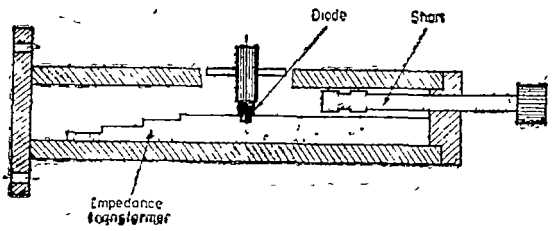

Fig 6 Oscillator configuration

If the post diameter is greater than 1 mm, the effect of the phase variation of the field across the posts in the Z direction is more evident [3]. In account of this effect, a new reactance x_{sc} may be insert in the equivalent circuit, thus the final equvalent circuit may be seen in Fig 5

The expression of x_{sc} is given by.

$$x_{sc} = -2Z_0 \frac{a}{\lambda g} \left(\frac{\pi d}{a}\right)^2 \sin^2 \frac{\pi s}{a}, \tag{11}$$

referred to the center of the guide

Experiment. On the basis of the above theoretical discussion we have been realized an oscillator presented in Fig 6

The values of the Z_a, Z_b and Z_c impedances as a function of the microwave length have been determined by means of the computer program The plot of these functions, for different values of the post diameter, are shown in Fig. 7

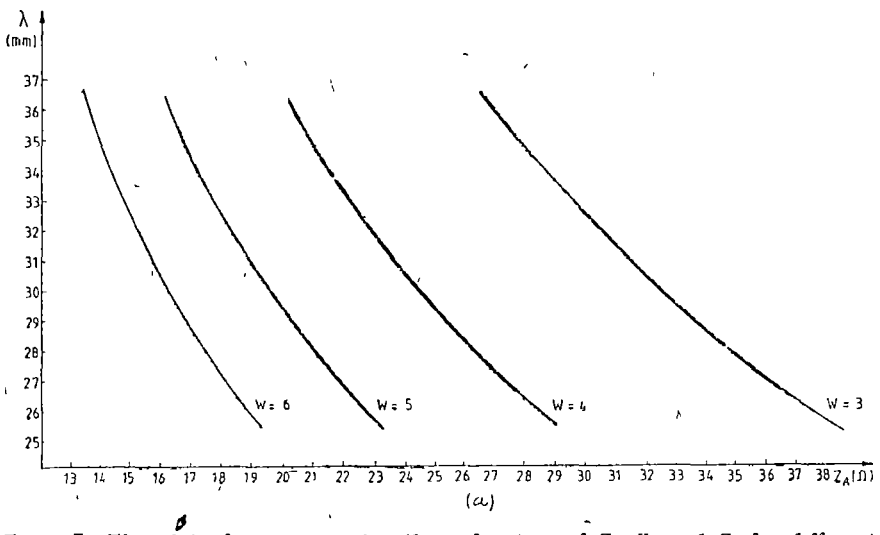

Fig 7 The plot of microwave length as function of Z_a, Z_b and Z_c for different values of post diameter

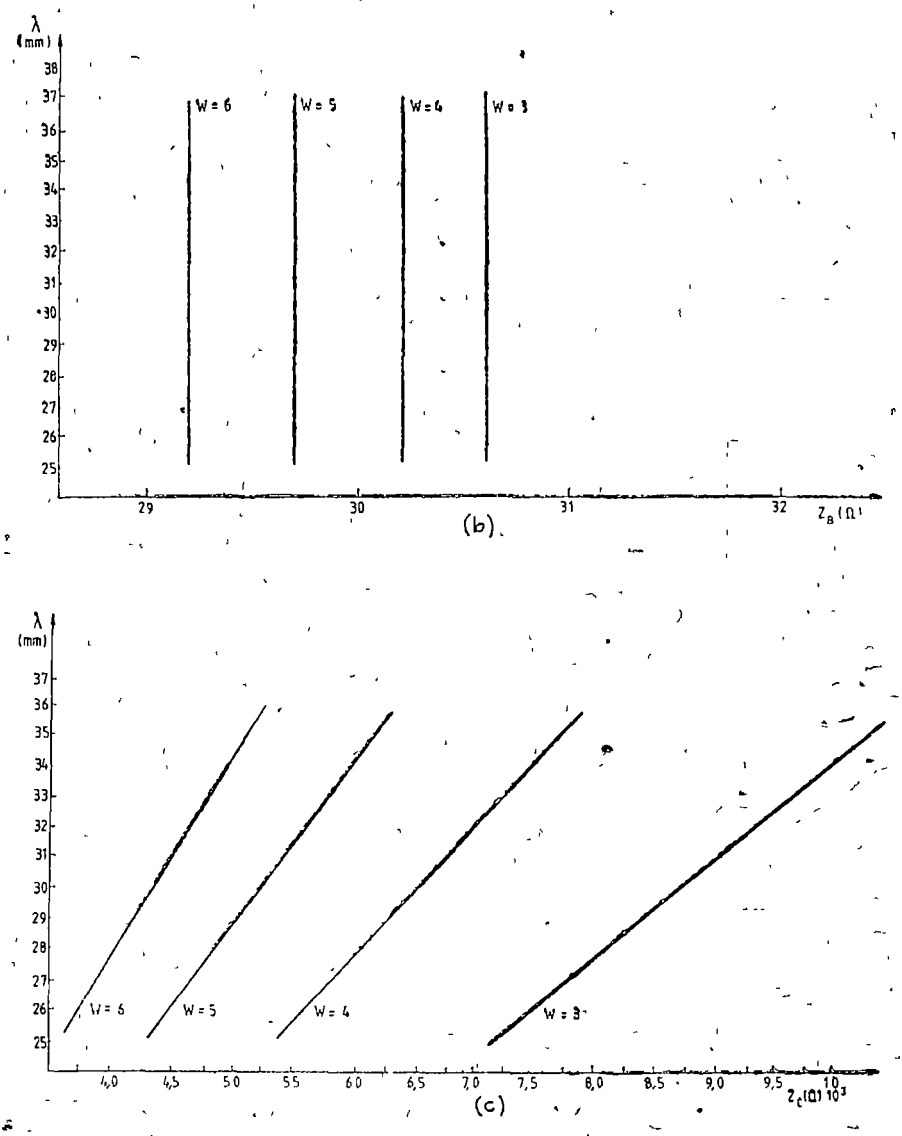

Fig 7

There have been used as active devices, two diodes with following parameters.

	L(nH)	C_p(nH)	R_p(Ω)	R_s(Ω)	C_p(pF)	C_{p1}(pF)	C_{p2}(pF)
IMPATT	0 6	0 3 pF	−2		0 52		
VARACTOR	0 6	0 3 pF		1		1 08	3 23

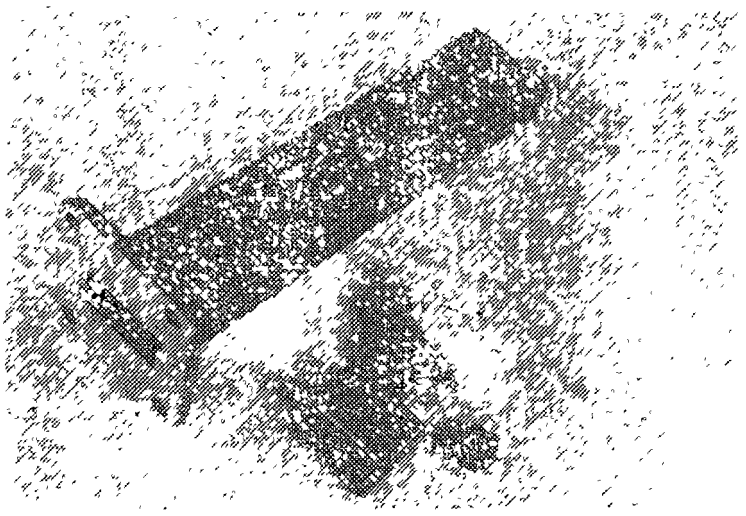

Fig 8 The photography of oscillator

Following the general method used to determine the resonance condition for the network presented in Fig. 5, we found the resonance frequency $f_1 = 1\,0909 \times 10^{10}$ Hz for $C_{p1} = 1.08$ pF and $f_2 = 1.0526 \times 10^{10}$ Hz for $C_{p2} = 3\,23$ pF Taking into account these values of the resonance frequences, the bandwidth will be $B = 383$ MHz.

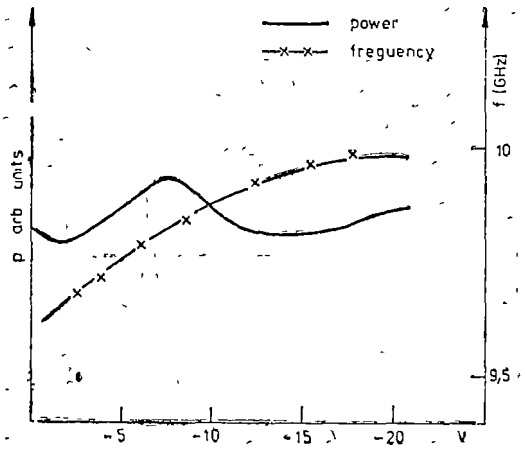

Fig 9 a) The plot of the power as a function of he voltage across the varactor diode, b) The plot of the frequency as a function of the voltage across the varactor diode

Experimental, we found a 300 MHz bandwidth for a zero to twenty volt triangular voltage, across the varactor.

Fig 8 presents the photography of the oscillator, and Fig 9 shows the plot of the microwave power and the frequency as a function of the voltage across the varactor diode, drawn by means of the curve drawer PROCESSOR TYPE —4910/9.

Conclusion. On the basis of the experimental measurements, we may conclude that the above mentioned theory provides a fairly good method to characterize the parallel varactor-tuned waveguide IMPATT oscilator.

REFERENCES

1 R L Eisenhart and P J Khan, *IEEE Trans MTT*, vol MTT **19**, pp 706–719, Aug 1971
2 L Osman El-Sayed, *IEEE Trans MTT*, vol MTT **22**, No 8, pp 769–776, Aug 1974
3 N Marcuvitz, "Waveguide Handbook" (MIT Rad Lab Ser, vol **10**), New York McGraw-Hill, 1951, pp 258–262
4 R Baican, „Oscilatori și amplificatori de microunde cu dispozitive semiconductoare", Ed. Acad RSR, București, 1979, p 67

STUDIA UNIV BABEŞ-BOLYAI, PHYSICA, XXXV, 1, 1990

DEPENDENCE OF THE ELECTRICAL RESISTANCE OF THE ZSM—5 TYPE ZEOLITE CONTAINING CHROMIUM ON THE ATMOSPHERIC PRESSURE

V. CRISTEA*, ELEONORA TRIF*, DORINA STRUGARU*, R. RUSSU**, GABRIELLA GHEORGHE** and IULIANA GROZA***

Received October 10, 1989

ABSTRACT. — The paper presents the influence of the atmospheric pressure and of the thermal treatment upon the electrical resistance of the mixtures of HZSM—5 zeolite and various contents of CrO_3. The dependence $R = R(p)$ changes from $R = Rp_0^{-\alpha}$ for parent HZSM—5 zeolite to $R = R_0 - \alpha \ln p$ for mixtures $y\%$ CrO_3 + HZSM—5 and suggests that in the later case there are two or more contributing effects to the electrical conduction. The parameter α increases when the concentration of the oxide increases and can be taken as a measure of the electrical conductibility.

1. Introduction. Owing to various utilizations, the aluminosilicates of zeolite type stand in attention of many research centers in the latest decades. Great attention has been devoted to the synthesis and to the physico-chemical properties of new types of zeolites crystallized in the presence of organic bases. Among these materials, zeolite ZSM—5 containing polyvalent ions has become a material of high commercial importance, especially in the conversion of methanol into hydrocarbons. Increasing interest has been devoted to ZSM—5 zeolites containing chromium (Si/Al = 47.2).

The introduction of chromium ions in cation sites has been carried out by solid state reaction between HZSM—5 zeolite and CrO_3 oxide.

The migration, the distribution and the valence of the chromium ions is interesting from both the theoretical and practical viewpoint [1—3]. Our study describes the influence of the atmospheric pressure and of the thermal treatment upon the electrical resistance of the ZSM—5 zeolite containing chromium.

2. Samples preparation. Homogeneous mechanical mixtures of HZSM—5 zeolite and various contents (0%, 1%, 5% and 10% wt) of CrO_3 oxide were prepared. These mixtures were then compacted as pellets under a pressure of 3×10^8 N/m^2. Some pellets were obtained from mixtures calcined previously at 1073 K. On each pellets, the Ag electrodes were deposed by vacuum evaporation. The pellets equipped with Ag electrodes were keeped in air at room temperature.

* *University of Cluj-Napoca, Department of Physics, 3400 Cluj-Napoca, Romania*
** *ICITPR, 2000 Ploiești, Romania*
*** *Secondary School, 3360 Copăcenî, Romania*

3. Results and Discussion. The experimental procedure has been described in our earlier work [4] Owing to the dependence of the resistance on the applied tension, all measurements were performed by maintaining a constant value of the applied tension (100 V)

In Fig 1, the variation of the resistance with pressure for the parent zeolites (0% CrO_3) is shown, in bolth the semilogarithmic (a) and the doublelogarithmic scale (b) It can be seen that the experimental points describe, in a quite good aproximation, a line of the type:

$$\ln R = \ln R_0 - \alpha \ln p \qquad (1)$$

or

$$R p^{\alpha} = R_0 \qquad (1')$$

where $R_0 = 2\,57 \times 10^{12}\Omega$ and $\alpha = 1\,05$.

In a previous study [4] we obtained or Y type zeolites a relationship of the form

$$Rp = \text{const.} \qquad (1'')$$

which is similar to the (1') one, when $\alpha = 1$

The relationship (1'') shows the decreasing of the carriers mobility with pressure diminution, which is accompanied by water extraction from the pores of the samples. The value of $\alpha = 1\,05$, close to unity, obtained for HZSM—5 zeolites shows that the previous interpretation is valid also for the ZSM—5 type zeolites

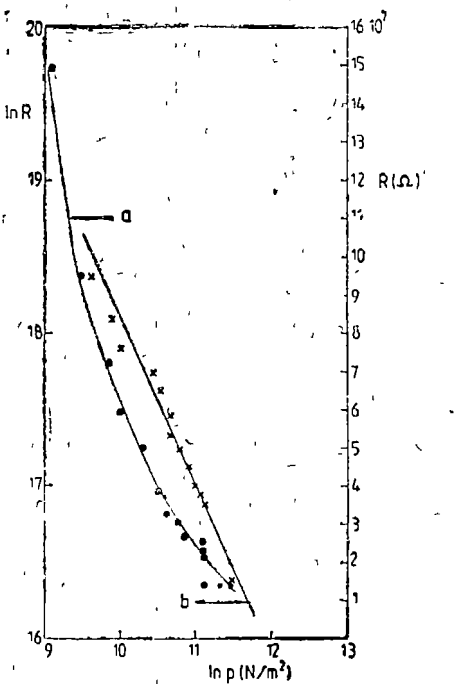

Fig 1 The pressure dependence of the electrical resistance for parent HZSM—5 zeolite a) semilogarithmic scale b) doublelogarithmic scale

The pressure dependence of the resistance for samples containing 1% CrO_3 is plotted in Fig 2. In the high pressure range the experimental points describe a straighline „c" of the type

$$R = R_0 - \alpha \ln p \qquad (2)$$

A similar behaviour, line „d", is obtained for samples heated previously at 1073 K and keeped then in air, at room temperature during five days The, values of the parameters R_0 and α were found to be: $R_c = 1.55 \times 10^9\ \Omega$ $\alpha_c = 1\,23 \times 10^8$, $R_d = 3\,22 \times 10^{10}\ \Omega$ and $\alpha_d = 2\,75 \times 10^9$ respectively

For samples containg higher concentrations of CrO_3, the experimental results are presented in Fig. 3, namely.

e) for uncalcined mixture of ZSM—5 and 5% CrO_3,

f) for calcined mixture at 1073 K of ZSM—5 and 5% CrO_3;

g) for uncalcined mixture of ZSM—5 and 10% CrO_3.

At pressures higher than $p > 166$ mmHg, the experimental points describe straighlines corresponding to Eq. (2), with the parameters:

$R_c = 25.4 \times 10^8\ \Omega$ $R_f = 1.29 \times 10^{11}\Omega$ $R_g = 47\,4 \times 10^8\Omega$

$\alpha_c = 1\,88 \times 10^8$ $\alpha_f = 10^{10}$ $\alpha_g = 3\,79 \times 10^8$

It can be observed that the values of the parameters R_0 and α depend on the concentration of CrO_3 oxide and on the thermal treatment history.

4 **Conclusion.** The pressure dependence of the electrical resistance of the parent zeolites can be described by relation $Rp^{\alpha} = R_0$ (1')

For mixtures of HZSM—5 with CrO_3 oxide the pressure dependence of the electrical resistance is changed compared with than of the pure HZSM—5. The experimental points lie on the straighline $R = R_0 - \alpha \ln p$ (2). In the case of the parent sample in a limited range of pressure only, i.e $36\,316\ \frac{N}{m^2} < p < 98715\ N/m^2$, the function (1') may be approximated by the straighline (2) having the parameters $R_0 = 3 \times 10^8\Omega$ and $\alpha = 2\,5 \times 10^7$ For samples containing 1% CrO_3, the parameter α increases by an order of magnitude, i.e , $\alpha_o = = 1.23 \times 10^8$. By increasing the content of oxide, the parameter α increases but its order of magnitude is not affected compared with samples containing 1% CrO_3. This indicates that only a limited number of metallic ions contributes to the conduction.

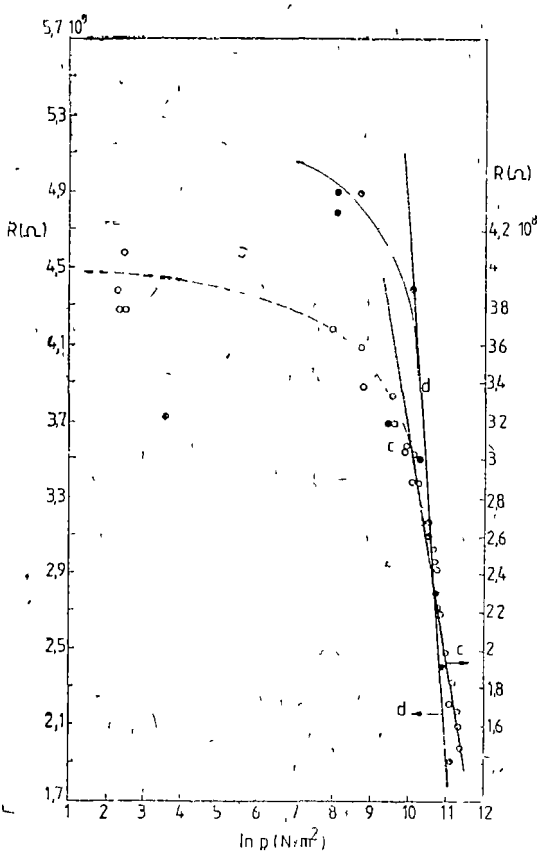

Fig 2 The pressure dependence of the electrical resistance for 1% CrO_3 + HZSM—5 mixture c) for uncalcined mixture d) for mixture heated previously at 1073 K.

The change of the function $R = R(p)$ from $R = R_0 p^{-\alpha}$ for parent HZSM—5 zeolite to $R = R_0 - \alpha \ln p$ for mixtures y% CrO_3 + + HZSM—5, suggests that in the later case there are two or more contributing effects to the electrical conduction One of this is the ionic conductibility accomplished by chromium ions (Cr^{2+} and Cr^{5+}) as charge carriers. The ions migrate from outer surface of the zeolite into the pores of zeolite when the solid-state interaction occurs between H-zeolite and CrO_3 oxide The

solid-state interaction may occur slowly at room temperature also Hence, by EPR we detected [3] isolated ions for mixtures prepared one year ago According to the EPR results, the increase of the parameter α, by at least one order of magnitude for calcined samples, indicates a greater number of ions entered in canals and cavities of the zeolites

The formation of the Cr_2O_3 crystalline compound evidenced by DRX, from CrO_3 in excess, not interacted with zeolite, can also contribute to the increase of the α parameter value when increases the concentration of the CrO_3 oxide in the mixture

For all investigated samples, a marked variation of the electrical resistance was observed in the normal pressure vicinity This indicates that the HZSM—5 zeolite may be dehydrated easier than the Y type zeolite. These results are in agreement with those obtainde by thermal analysis [5]. Indeed, the value of the endothermic peak has been obtained at $T = 120°C$ for HZSM—5 zeolite and at $T = 220°C$ for Y-type zeolite, respectively.

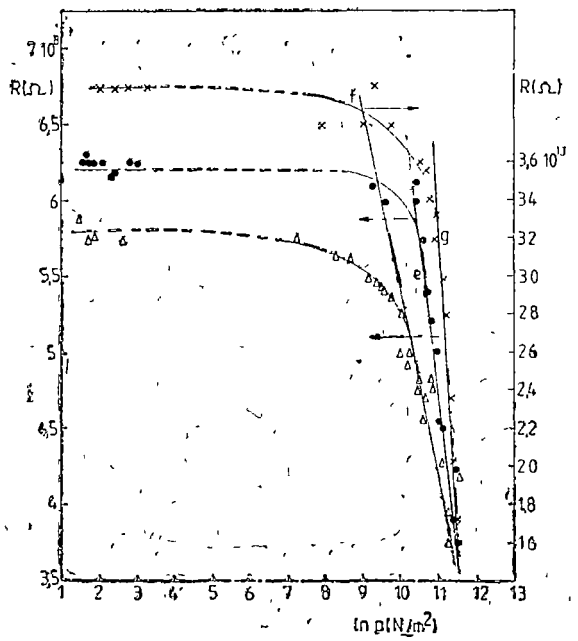

Fig 3 The pressure dependence of the electrical resistance for e) uncalcined mixture of 5% CrO_3 + HZSM—5, f) calcined mixture of 5% CrO_3 + HZSM—5, g) uncalcined mixture of 10% CrO_3 + HZSM—5

Our results suggest that the parameter α can be a measure of the electrical conductibility.

REFERENCES

1 A V Cucerov, A A Slinkin, *Kinetika i kataliz*, **29**, 3, 678 (1986)

2 A V Cucerov, S S Tariascenko, E G Aleşin, K I Slobetskaia, *Kinetica i kataliz*, **30**, 1, 184 (1989)

3. E Trif, D Strugaru, I Ivan, R Russu, G Gheorhe, in vol „Probleme actuale de fizică", coordonator I Ardelean, Cluj-Napoca 1988, p 23

4 V Cristea, E Trif, Al Nicula, *Studia Univ Babeş—Bolyai, Physica*, XXXII, (1), 30 (1987)

5. E Trif, D Strugaru, I Ivan, R Russu, G Gheorghe şi Al Nicula, *Studia Univ Babes—Bolyai, Physica*, XXXIII (1), 79 (1988)

STUDIA UNIV BABEŞ BOLYAI, PHYSICA, XXXV, 1, 1990

SOURCES WITH IMPOSED MOTION IN THE THEORY OF GENERALIZED RELATIVITY

Z. GÁBOS*

Received January 19, 1990

ABSTRACT. — The gravific coupling between two bodies has been studied in two cases For the isolated system consisting from two bodies it is generally accepted that the system has a natural (inertial) motion, thus it was studied in fact a motion without constrains There are few investigations of the case in which one of these bodies (the source body S) has an imposed motion

In this paper we study the gravific action on the body S on the second body P which is considered without constrains We showed the existence of the training effect which appears when the body S has an accelerated motion

1. The system consisting from two material points. Let us consider the vectors $\vec{x}$ and $\vec{v}$ denoting the position and the velocity of the material point P The same vectors for the material point S are given function of time, and will be denoted by $\vec{X}(t)$ and $\vec{V}(t)$. The rest masses of the two bodies are respectively m_0 and M_0.

If we are content with a second order approximation the simplest possibility to describe the motion of the material point P is given by the Fock-Fichteholtz Lagrangean [1]. From this Lagrangean we keep only the terms which are necessary for the description of the studied effect:

$$L = -m_0c^2\sqrt{1-\frac{v^2}{c^2}} - \frac{m_0\lambda}{2r}\left[7(\vec{v},\vec{V}(t)) + (\vec{n},\vec{v})(\vec{n},\vec{V}(t))\right] + \ldots, \tag{1}$$

where

$$\lambda = \frac{kM_0}{c^2},\quad r = |\vec{x}-\vec{X}(t)|,\quad \vec{n} = \frac{\vec{x}-\vec{X}(t)}{r}. \tag{2}$$

The Euler-Lagrange equation

$$\frac{\partial L}{\partial \vec{x}} - \frac{d}{dt}\left(\frac{\partial L}{\partial \vec{v}}\right) = 0 \tag{3}$$

gives the motion equation of the material point P

$$\frac{d}{dt}\left(\frac{m_0\vec{v}}{\sqrt{1-\frac{v^2}{c^2}}}\right) = \frac{7m_0\lambda}{2r}\dot{\vec{V}} + \frac{m_0\lambda}{2r}(\vec{n},\dot{\vec{V}})\vec{n} + \ldots, \tag{4}$$

where we keep only the terms which contain $\dot{\vec{V}} = \vec{A}$.

* *University of Cluj-Napoca, Department of Physics, 3400 Cluj-Napoca, Romania*

From the Eq (4) results the existence of a training effect. The force associated with the effect has two contributions The first one is acting on the imposed acceleration. The second contribution has a radial direction and is sensitive dependent on the component $(\vec{n}, \dot{\vec{V}}) = A_r$ of $\dot{\vec{V}}$ for $A_r < 0$ respectively $A_r > 0$ the material point S is acting with a traping, respectively repulsion force on the material point P.

We also have to mention that

a) the component of the second training force in direction of $\vec{A}$ has the positive expression

$$\frac{m_0\lambda}{2r}\frac{A_r^2}{|\dot{\vec{V}}|}, \tag{5}$$

b) if we denote the training force by $\vec{F}_a$, from (4) we get

$$(\vec{n}, \vec{F}_a) = \frac{4m_0\lambda}{r}(\vec{n}, \dot{\vec{V}}), \qquad (\vec{n} \times \vec{F}_a) = \frac{7m_0\lambda}{r}(\vec{n} \times \dot{\vec{V}}) \tag{6}$$

We also note that the coefficients from (6) have positive values.

2. The system consisting from two rigid spherical bodies. We consider now the case when the body P has a spherical shape with the radius a and the rest mass m_0 (the distribution of the rest mass is uniform) which interact with a central spherical body S with the radius A and the rest mass M_0 (the distribution of the rest mass presents a spherical symmetry) The origin of the reference system will be considered in the centre of the body S, which has a rotation motion with a variable angular velocity $\vec{\Omega}(t)$ (the rotation axis crosses the origin) We will denote the position vector and the velocity of the center of the body P by $\vec{x}$ and $\vec{v}$

a) *The rotation-translation training effect* In this case from the Lagrangean of the system we will consider the terms [2]

$$L = -m_0c^2\sqrt{1 - \frac{v^2}{c^2}} - \frac{4m_0\lambda A^2}{3r^3}\alpha(\vec{x}, \vec{v}, \vec{\Omega}) + \ldots, \tag{7}$$

where

$$\alpha = \frac{I_4}{A^2I_2}, \qquad \text{and } I_n = \int_0^A \mu(r)r^n \mathrm{d}r$$

(μ being the mass density).

From (4) and (2) we get

$$\frac{d}{dt}\left(\frac{m_0\vec{v}}{\sqrt{1 - \frac{v^2}{c^2}}}\right) = \frac{4m_0\lambda A^2}{3r^3}\alpha(\dot{\vec{\Omega}}x\vec{x}) + \ldots \tag{8}$$

The material point in trained by a force which is acting in direct sens.

b) *The rotation-rotation training effect* From the Lagrangean which describes the system we keep the terms [2]

$$L = \frac{m_0}{5} a^2\omega^2 + \frac{4m_0\lambda}{15r^5} \alpha a^2 A^2 [(\vec{\Omega}, \vec{\omega})r^2 - 3(\vec{\Omega}, \vec{x})(\vec{\omega}, \vec{x})] + \ldots \tag{9}$$

($\vec{\omega}$ being the angular velocity of the body denoted by P)

Using the equation of motion

$$\frac{d}{dt}\left(\frac{\partial L}{\partial \vec{\omega}}\right) = \left(\vec{\omega} x \frac{\partial L}{\partial \vec{\omega}}\right. , \tag{10}$$

we get

$$\dot{\vec{\omega}} = -\frac{2\lambda A^2}{3r^5} \alpha [\dot{\vec{\Omega}} r^2 - 3(\dot{\vec{\Omega}}, \vec{x})\vec{x}] + \ldots \tag{11}$$

From the Eq. (11) we get the relations:

$$(\vec{x}, \dot{\vec{\omega}}) = \frac{4\lambda A^2}{3r^3} \alpha(\vec{x}, \dot{\vec{\Omega}}), (\vec{x} \times \dot{\vec{\omega}}) = -\frac{2\lambda A^2}{3r^3} \alpha (\vec{x} \times \dot{\vec{\Omega}}). \tag{12}$$

The radial component of $\dot{\vec{\Omega}}$ gives rise to a training effect in the positive sens (direct sens) while the transverse component of this quantity (perpendicular on $\vec{x}$) produces a training effect in the negative sens The resultant effect is obtained from the superposition of the two opposite training effects

c) *The rotation-rotation training effect in the case of the internal Thirring effect* If the rest mass M_0 is distributed uniformly on the spherical surface of radius A and with the center in the origine (0), and the rest mass m_0 is distributed uniformly, inside of the sphere with radius a and the center in 0, we have [3]

$$\dot{\vec{\omega}} = \frac{4\lambda}{3A} \dot{\vec{\Omega}} + \ldots . \tag{13}$$

In this case we have a „pure" effect ($\dot{\vec{\omega}}$ and $\dot{\vec{\Omega}}$ have the same direction) the obtained training being in the positive sens

3 **Conclusions.** For a gravific coupling between two bodies, the body having an imposed accelerated motion is acting on the second body by a training effect.

In any cases a direct training is obtained namely translation-translation training for the material points, and the internal Thirring effect In the case of the rotation-rotation training the effect is sensitive to the geometry of the system because in this case two contrary effects are competing

Excepting the quantities $\dot{\vec{V}}$, $\dot{\vec{\Omega}}$, the effect is also influenced by the dimensionless quantities λ/r, A/r, but no dependence of m_0 has been observed.

REFERENCES

1 I G Fichtenholtz, *JETF*, **20**, 233 (1950)
2 Z Gábos, J Szén, *Studia Univ Babeş—Bolyai, Physica*, **29**, 46 (1984).
3. Z Gábos, *Studia Univ Babeş—Bolyai, Physica*, **33** (1), 38 (1988).

STUDIA UNIV BABEŞ BOLYAI, PHYSICA, XXXV, 1, 1990

SOME CONSIDERATIONS CONCERNING ENERGY TRANSFER BY LASER IRRADIATION OF SOLID SAMPLES

CĂLINA-DIANA CÂMPEAN*, M. VASIU** and I. N. MIHĂILESCU***

Received February 25, 1990

ABSTRACT — It was observed at resonance incidence that the absorbtion of laser radiation on metallic surface is highly amplified, both within and outside the irradiation spot. This has a particular interest in obtaining better energy coupling from a high intensity laser radiation to metallic samples.

Introduction. The occurrence of SPS (surface periodical structures) was shown to be a very general phenomenon [1–4]. A possible classification could divide the SPS that occur on sample surfaces as an effect of high-intensity laser irradiation into i) resonant surface periodical structures (RSPS) that form during laser action and their characteristics can be related to the incident laser beam parameters and, ii) non-resonant surface periodical structures (NRSPS) which appear in the molten material after switching off the laser, and seem to have geometrical characteristics with no relation with the incident laser beam parameters [1], [8–10].

RSPS either induced on the surface of various materials under the action of high intensity laser irradiation, or preexisting on the surface as a result of a prior processing, was given a great deal of attention in connection with their influence on the optical characteristics of the surface. The possible changes of the superficial absorbtivity A, may have large implications in any other physical processes on the irradiated surface.

It was shown that RSPS formed in the case of metals, result as an interference between the incident laser wave (ILW) and the surface electromagnetic waves (SEW), which are induced and propagate across the sample surface.

We shall review in this paper some recent results concerning the supplementary energy transfer from the laser radiation to RSPS metalic surfaces.

As for the mechanism involved in RSPS formation by high intensity laser irradiation of solid samples, one can refer to [3], [4], [6], [11], [12], [13], [15].

Theoretical predictions. We have examined [16] the interaction of a laser beam of rectangular cross-section $x_0 y_0$, with RSPS-riddled, metallic surface of a period $\Lambda = \frac{\lambda}{1 - \sin 0}$, with a sinusoidal profile, $z(x) = h \sin(gx)$, where h is the amplitude depth of RSPS, g is the RSPS inverse vector, $g = \frac{2\pi}{\Lambda}$ and $k = \frac{2\pi}{\lambda}$

* *Economic Lyceum, 3400 Cluj-Napoca, Romania*
** *University of Cluj-Napoca, Department of Physics, 3400 Cluj-Napoca, Romania*
*** *Central Institute of Physics, 7000 Bucharest, Romania*

the wave vector of the ILW We have considered that RSPS are covering only the irradiation spot.

The laser radiation is linearly polarized in the incidence plane with electrical field, E, of the ILW normal to RSPS grooves.

We emphasize the following characteristics which are due to the laser radiation absorbtion on the RSPS riddled surface, both within the limits of the irradiation spot and outside it on the planar surface.

a) The fraction p of the incident power (energy) which SEW evacuates along the Ox axis from the irradiation spot is given by:

$$p(x_0, h) \simeq M \frac{\alpha}{\alpha_d} C(h) F_2(\alpha x_0) \tag{1}$$

where $M \leqslant 1$ is a dimensionless constant very close to unity in case of metals·

$$C(h) = \frac{4h^2h_0^2}{(h^2 + h_0^2)^2} \tag{2}$$

$$F_2(\alpha x_0) = (1 - e^{-\alpha x_0})^2/(2\alpha x_0) \tag{3}$$

and

$$\alpha = \alpha_d + \alpha r = \alpha_d \left(1 + \frac{h^2}{h_0^2}\right) \tag{4}$$

is the SEW attenuation coeficient, taking into account the heat dissipation into the metal α_d and outside it, α_r.

We suppose:

$$\alpha^e \approx \alpha_d^e; \qquad \alpha_r^e = 0 \tag{5}$$

$$\alpha_d = \frac{\pi}{8\lambda} \frac{A_0^2 k}{n} \tag{6}$$

A_0 is the absorptivity of the planar surface of normal incidence, k and n are the absorptive index and refractive index of the metal.

b) The fraction p of the power (energy) taken by SEW off the irradiation spot is dissipated as heat on the planar surface of the target. The absorptivity determined in this case outside the irradiation spot is [16]

$$A_2(x_0, x_T, h) = M(\alpha/\alpha_d) C(h) F_2(\alpha x_0)[1 - e^{-2\alpha_d^e(x_T - x_0)}]$$

$$\simeq p(x_0, x_T, h)[1 - e^{-2\alpha_d^e(x_T - x_0)}] \tag{7}$$

Whenever the following condition is fulfilled

$$x_T - x_0 \geqslant 1/(2\alpha_d^e) \tag{8}$$

we have in the case $h^2 \geqslant h_0^2$

$$x_0 \simeq 1{,}26/\alpha(h) \tag{9}$$

the absorptivity $A_2(x_0, h) \to A_2^{\max}(h) \simeq p_{\max} \simeq 0{,}8$ i e. as much as 80% of the incident laser power (energy) is evacuated by SEW outside the irradiation spot where it is completely absorbed into the sample

c) SEW excitation determines also a supplementary absorptivity in the limits of the irradiation spot, A_1:

$$A_1(x_0, h) = C(h)\, F_1(\alpha x_0) \tag{10}$$

where

$$F_1(\alpha x_0) \simeq (2\alpha x_0 - 3 + 4e^{-\alpha x_0} - e^{-2\alpha x_0})/(2\alpha x_0) \tag{10}$$

if $x_0 \gg 1/(2\alpha)$ we have $F_1(\alpha x_0) \simeq 1$, and $F_2(\alpha x_0) \simeq 0$.

Therefore, from Eqs (7) and (11) we get

$$A_1(x_0, h) \simeq A_1(h) = MC(h)$$
$$A_2(x_0, x_T, h) \simeq 0 \tag{11}$$

i.e. SEW do not succeed to evacuate power (energy) outside the irradiation spot.

d) In the case we have

$$\alpha x_0 \leqslant 1 \text{ or}$$
$$\alpha x_0 << 1$$

is easy to show that we get:

$$A_1(x_0, h) \leqslant A_2(x_0, x_T, h) \tag{12}$$

i.e. the incident laser power (energy) absorptivity outside the irradiation spot can largely exceed the absorptivity within the limits of the irradiation spot.

Conclusions. When the laser radiation is falling upon a RSPS riddled metalic sample, the laser radiation absorption is governed by some important features.

1) A supplementary laser radiation absorption takes place, inside and outside the irradiation spot.

2) Both supplementary absorptivities of the incident laser power (energy) inside A_1 and outside A_2, the irradiation spot depend not only on the amplitude depth h, of the RSPS, and also on spot dimension x_0, while A_2 depends only on target dimension x_1.

3) When we use an optimum choice of h_0, x_0 and x_T we get maximum values of A_1 and A_2.

REFERENCES

1. I. Ursu, I N Mihăilescu, Al Popa, A. M. Prokhorov, V. P Ageev, A A Gorbunov and V I Konov, *J Appl Phys.*, **58**, 3909 (1985)
2. I. Ursu, I N Mihăilescu, L.C Nistor, V S Teodorescu, A M Prokhorov, V I Konov, *Appl Opt*, **24**, 3736 (1985)
3 D J Ehrlich and Y Tsao, *J. Vacuum Sci Technol* **B**, **1**, 978 (1986)
4 J Moylan, D Baum and R Jones, *Appl Phys* **A**, **40**, 1 (1986)
5 F Keilman, *J Phys (Les Uhs)* **C**, **5**, 77 (1983)
6 S F Yoeng, J S Preston, H M van Driiel and J E Sipe, *Phys Rev* **B**, **27**, 1155 (1983)
7 I. Ursu, I N Mihăilescu, Al. Popa, A M Prokhorov, V.I Konov, V.N Tokarev, *Appl. Phys Letters*, **45**, 365 (1984)
8. T J. Bastow, *Nature*, **222**, 1058 (1969)

9. S. J Thomas, R.F. Harrison and J F Figueira, *Appl. Phys Letters*, **40**, 200 (1982)
10. J F Figueira and S. J Thomas, *IEEE J Quantum Electron* QE—**18**, 1380 (1982)
11. F Keilman and Y H Bai, *Appl Phys* **A, 29**, 9 (1982)
12. A M Bonch—Bruevich, M K Kochenghina, M I Libensons and V S. Makyn, *Akad Nauk SSSR, Ser Fiz*, **46**, 1186 (1982)
13. H M. van Driel, J E Sipe and J.F Young, *Phys Rev Letters* **B, 30**, 2001 (1984)
14. I Ursu, I N. Mihăilescu, A.M Prokhorov, V I. Konov and V N Tokarev, *Appl. Surf Science*, **36**, 471 (1989)
15. Zhou Guosheng, P M. Fouchet and A E Siegmann, *Phys Rev.* **B, 21**, 5366 (1982)
16. C D Câmpean, *Thesis, Univ. of Cluf-Napoca, 1990.*

STUDIA UNIV BABEŞ-BOLYAI, PHYSICA, XXXV, 1, 1990

THERMISTANCE À ÉCHAUFFEMENT INDIRECT

C. CODREANU* and S. CODREANU**

Recu le 15 Janvier, 1990

RÉSUMÉ. — On a étudié un prototype-thermistance à échauffement indirect, en utilisant une thermistance originale miniaturisée sémi-réfractaire Nous avons présenté les caractéristiques $R(T)$ et $U(I)$, de même que les principaux parametres R_{293}, ΔE, B, α_T

Introduction. On utilise ce type de dispositif électronique dans les cas où l'on exige une séparation électrique entre le circuit de commande, d'une part et le circuit commandé, d'autre part comme, par exemple — la télécommande des systémes mécaniques, la protection de surcharge des circuits électroniques, dans l'anémométrie etc Ce fait est possible par l'entremise d'un microréchaud, placé au voisinage immédiat du corp actif de la thermistance, de sorte que la chaleur dissipée par celui-là peut modifier le régime d'équilibre thermique de la thermistance.

Expériment. Nous avons realisé une thermistance prototype en utilisant une thermistance sphérique miniaturisée (d = 1,2 mm), munie de sorties en fil PtIr, dont le matériel est un sèmiconducter céramique ($MnO-CoO-LaB_6$), à partir d'une phase coulée, par une technologie spéciale [1]

Le microréchaud spiralé a une résistance nominale $R_2 = 2{,}9\Omega$ Les deux éléments sont introduits dans une ampoule cylindrique en verre, remplie d'air sous pression normale, ayant quatre sorties (contacts), comme on le voit sur la figure 1

Résultats et discussions. La caractéristique thermique expérimentale $R_1(T)$, (fig 2), correspond trés bien à la lois théorique [2].

$$R_1(T) = T_{T_0} \exp B\left(\frac{T_0 - T}{T_0 T}\right)$$

où $T_0 = 293$ K, $R_{T_0} = 278{,}046$ kΩ.

En analysant les fonctions $R_1(T)$ et $\ln R_1 = f(1/T)$, (fig 2), on a évalué les quelques principaux paramétres de la thermistance, présentés dans le tableau A.

Tableau A

Résistance nominale	R_{293}	(kΩ)	278
Constante électronique	B	(K)	4833
Energie d'activ therm	ΔE	(eV)	0,8
Coeff thermique de R_T	α_T	(%/K)	(5,6 – 1,5)
Temp max admise	T_{max}	(K)	570

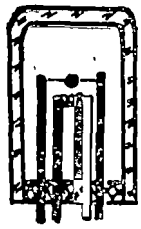

Fig 1

* *L'Institut Polytechnique de Cluj-Napoca, 3100 Cluj-Napoca, Roumanie*
** *L'Universite de Cluj-Napoca, 3400 Cluj-Napoca, Roumanie*

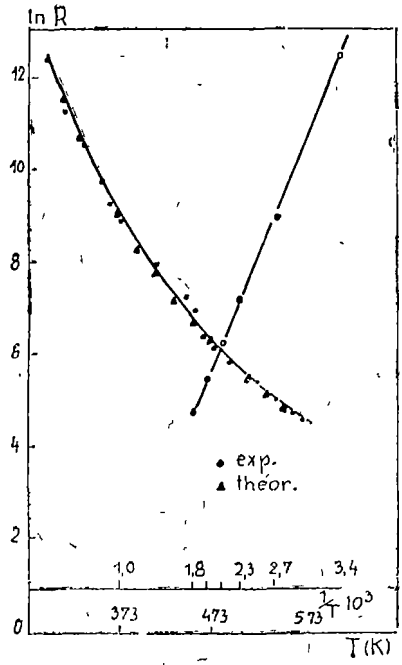

Fig 2

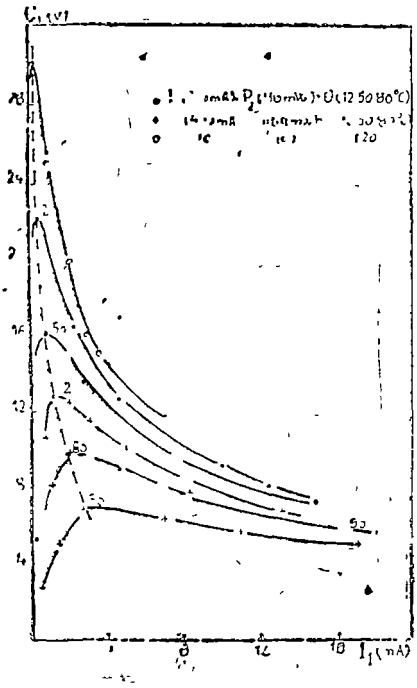

Fig 4.

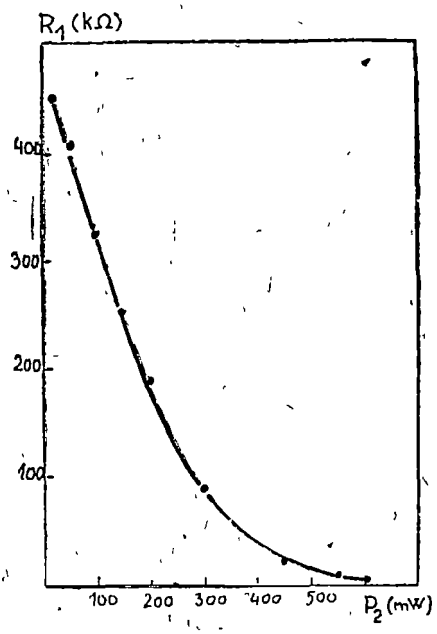

Fig 3

D'après les valeurs de ΔE et α_T on peut supposé, d'une part, que la conductibilité électrique du matériel est du type extrinséque, et d'autre part, que la thermistance conserve une sensibilité thermique assez bonne même à des températures relativement élevées.

La caractéristique de l'échauffement $R_1(P_2)$, où P_2 est la puissance électrique dissipée en R_2, est présentée sur la figure 3 On remarque une dépendance presque linéaire jusqu'à $P_2 = 300$ mW avec une variation $dR_1/dP_2 = 0{,}5$ kΩ/mW.

En considérant P_2 (max) $= 600$ mW, on obtient une résistance "chaude" de la thermistance, $R_c = 5$ kΩ, d'où en résulte que le coefficient du couplage thermique $K = P_1/P_2$ a la valeur 0,08 (8%)) où $P_1 = U_1 I_1 = 49$ mW est la puissance qu'on doit dissiper en R_1 ainsi que $R_1 = R_c$

Les caractéristiques statiques $U_1(I_1)$ ont été relevées pour de différentes valeurs de la température extérieure et du courant électrique d'échauffage I_2 Sur la figure 4 est présentée, partiellement, la famille des courbes obtenues, expérimentalement,

Dans toutes les variantes étudiées on obtient l'effet relais, pour des valeurs relativement faibles de P_2 (20—25) mW, fonction de θ et I_2, ce qui permet un choix assez large des variantes d'utilisation du dispositif obtenu On remarque, par exemple, l'équivalence des modifications de la caractéristique statique $U(I)$ provoquées soit par la variation de I_2 (200—400) mA, soit par la variation correspondante de T (50—80) °C

Conclusions. On peut donc conclure que le prototype réalisé pourrait être utilisé efficacement dans de différentes schémas de télécommande ou de téléréglage, surtout dans les cas où l'on dispose de valeurs assez élevées de P_2, sans une préamplification.

BIBLIOGRAPHIE

1 C Codreanu, I Cosma, M Vancea, Brev inv 68105/1979 „Procédé et dispositif pour le confectionnement des thermistances-type miniaturisé"
2. G N Dulnev, „Teploobmen v radioelectronnih ustroistvah", Mosc — Len, 1963, p 95.

STUDIA UNIV. BABEŞ-BOLYAI, PHYSICA, XXXV, 1, 1990

SOME ASPECTS OF THE CORRELATION BETWEEN SUNSPOTS AND CYCLONES

A. KÓSA-KISS* and H. SZŐCS**

Received January 1, 1990

ABSTRACT. — The present correlation analysis is based on our own observations which cover two decades We deduced an indirect interdependence between the sunspots which fulfil certain conditions and the meteorological cyclones The physical relationship is materialized into a directed effect The indirect cause is the sunspot, while the effect is the polar cyclone The phenomenon will be called correlation, the respective sunspot will be called correlational sunspot, while the meteorogical formation will be called correlational cyclone In the correlational process, the intermediary factor (modulator) is the solar plasma (solar wind) ejected from the sunspot, which heats the terestrial atmosphere, favouring the meteorological effect the atmospheric changes start, having as consequence the constitution of the cyclone

Some meteorological researches proved that, during certain time intervals, the air temperature and the quantity of precipitations change parallelly with the relative number of sunspots , for instance, maximum values of the air temperature and rainfalls correspond to the maximum values of the sunspot number. Such periods are followed by asynchronous intervals [6, 7]. The American researchers Roberts and Olson have examined since 1964 those days when the geomagnetic activity showed appreciable increases in intensity According to their supposition, the causes are solar They have also studied the behaviour of the cyclones which start from the bay of Alaska and pass over the North—American land, establishing that during an increased geomagnetic activity the cyclones are generally stronger than usually [8]. According to the analysis of the data provided by three meteorological stations in Central Europe, as a consequence of violent solar flares, ten days after, the atmospheric thermal values exceed considerably the average of several years. This correlation is based on the analysis of 30 studied phenomena But there are remaining the following problems which is the origin of the warm air masses which cause the weather heating? Which is the path of these ones? What is the latitude up to which their influence can be tracked?

The above analysis is based on solar flares. But a solar flare is a phenomenon which appears suddenly and ends rapidly Only the corpuscular and electromagnetic radiation directed towards the Earth reach our planet, producing various effects [1—5]

Having in view these considerations, we dwelt upon the particles ejected by the sunspots and transported through the solar wind Due to the relative

* *Water Treatment Station, 3650 Salonta, Romania*
** *Engineering Institute, 4800 Baia Mare, Romania*

motions of the Sun and Earth, the Earth can cross several times the flow of particles ejected by one and the same sunspot

Our observations concerning the extent and position of the sunspots with respect to the central meridian (CM), as well as the weather conditions, started in 1971 [9, 10] We used a 15 cm reflector and took a particular heed of the morphology of the clouds [11] In this way, it was possible to perform a comparison between the positions of the sunspots appeared between 1971—1985 in the CM region and the beginning of the precipitations from the clouds which covered the sky

The analysis we performed showed that the respective clouds were not of local origin, they were belonging to a cyclone which affected most of our continent. The precipitation system of the cyclone reached Salonta the days when the sunspots crossed CM (obviously, on a statistical average, there were deviations in time)

Table 1 lists the features of the solar events, provided by our observations compared with the observations performed at important centres of solar data [24, 25]. The heads of the columns signify No = current number of the correlational event, DCM = day when the sunspot crossed CM, So = heliographic latitude of the sunspot, MIC = P S McIntosh's classification; SGA = area of the sunspot group in millionths of solar area [25], No. B = current number of the sunspot group according to [24], the notations in the last column are A for authors' observations, B for observations made in Bucharest [24], C for observations made in Catania [25]; the symbol "—" in SGA and No. B columns indicates the lack of data. (See pag 61.)

The statistics of the correlational events is given in Table 2

Table 2

	"Hurried" cyclone				"Late" cyclone		
Deviations Δt (days)	−3	−2	−1	0	+1	+2	+3
Frequency of cases N	3	7	14	37	14	11	5

In most cases the deviations are of ± 1 day, namely the cyclone comes in Salonta one day sooner (the cyclone is "in a hurry") or later (the cyclone is "late") The 2—3 days deviations are more scarce. The value 0 represents the most outstanding cases The corresponding histogram is given in Fig 1

On the basis of the data listed in Table 2, the Gauss curve has the expression:

$$N(\Delta t) = 0.341 \exp\left(-0.29(\Delta t)^2 + 0.365\,\overline{\Delta t}\right),$$

with $\overline{\Delta t} = 0.63$ and $\sigma = 1.31$, 80% from cases lie into the range 2σ, while 99% from cases lie into the range 3σ The probability for a deviation of 4 days is $p = 0.516\%$

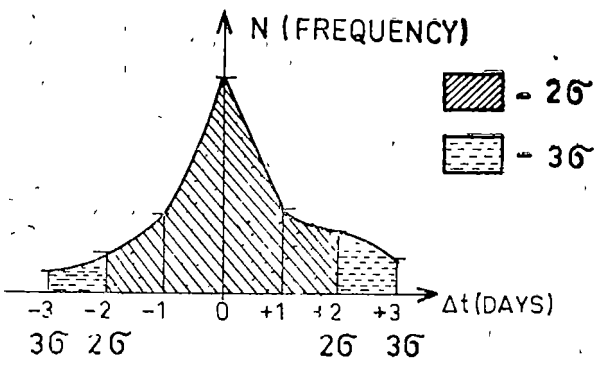

Fig 1.

The correlational sunspot appears generally into a group. Such sunspots appear especially in the years of maximum solar activity, but they were also observed in years of minimum solar activity, and even isolatedly The extent and compactness of the umbra from the sunspot penumbra proved to be decisive According to our observations, the sunspot umbra has a minimum diameter of 20 000 km and a homogeneous, compact structure, with unimportant changes of shape during the 12 days in which it can be observed The evolution of some correlational sunspot groups is plotted in Fig 2

The sunspot penumbra has a diameter of at least 30 000 km The correlational sunspot can exist during several solar rotazions. According to Waldmeier

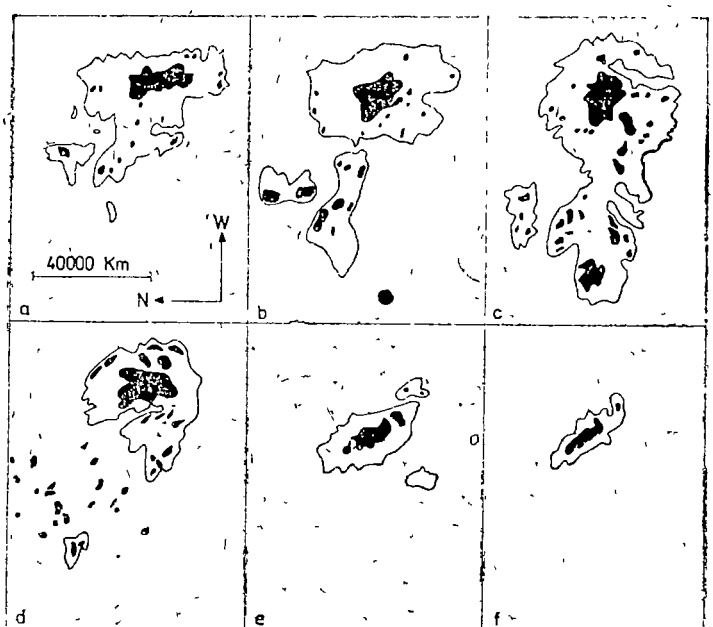

a - 24 JUNE 1977 15 45 (UT)
b - 25 JUNE 1977 15 40
c - 26 JUNE 1977 13 15
d - 29 JUNE 1977 12 55
e - 3 JULY 1977 15 25
f - 4 JULY 1977 15 30

Fig 2.

a sunspot group of maximum longevity was observed between August 23, 1966 and January 8, 1967 (139 days), interval in which the Sun performed 6 rotations [12] According to Kuveler's opinion, the stable sunspots are formed in less than 7 hours [13]. We observed that at the beginning of the formation of a correlational sunspot group only two pores can be seen, passing after three days into the form "D" (according to P S McIntosh's classification), in the fourth day it appears under the form of the type "E"; this active surface appears again under the same form at the next rotation. In order to reach the Earth, the solar particle must originate in sunspots whose optimum position is East or CM into a zone lying into the Eastern extremity of the solar disk. In the data provided by the artificial satellite *Solar Maximum Mission*, data concerning the intensity of the solar radiation [14], there were found minimum values just when the sunspot total area on the solar disk was maximum It seems that the maximum decrease of the solar constant occurs just in the period of rapid apparition of a great number of sunspots. According to Pap [15], this change of the solar constant takes place along some days and can be connected with the presence of stable sunspots covering wide areas The plasma which reaches the solar surface is acceleratedly propelled by the Alfvén waves towards to the corona. The close connection between the sunspot and the corona was proved by the space observations performed by means of *Apollo Telescope Mount* [16], according to which, shortly before the sunspot apparition, one observes coronal luminous points above the ulterior active zone. The coronal phenomena occur always in an active region of the solar surface [17] It is matter of a vertical space, of the form of a column, having at its base a sunspot group The local magnetic field connected with the sunspot group rises appreciably above the photosphere, penetrating into the K corona At the extremity of the corona, in the region of the coronal hole, the magnetic field is open, from here rapid flows of plasma go into the interplanetary space. A coronal hole lasts about six solar rotations, this stability being connected, in our opinion, with the correlational sunspots In August 1971 and July 1981 there was observed the apparition of coronal holes which crossed CM [18, 19] In these intervals we observed correlational events in the low atmospheric layers (correlational events 19, 47 and 48) A large sunspot group crossed CM on August 10, 1979 (sunspot "a"), while two large active zones crossed CM in July 24, 1981 (sunspot "b") and July 28, 1981 (sunspot "c"), respectively In the case of the sunspot "a", the researchers from the Zagreb Observatory observed the filament phenomenon, the sunspot "c" caused a second type solar flare, this last one being the cause of radio disturbances and polar light.

According to Parker [20], the plasma travels with a speed of 500—800 km/s, under the form of the solar wind, and reaches the Earth's magnetosphere after 2—3 days. When the plasma reaches the Earth, it is still consistent enough to increase the temperature of the different ionospheric layers above the North Pole. One knows from data provided by meteorological rockets that a UV radiation is produced, which reaches the stratosphere and is absorbed by this one. During this absorption, a heating of the stratosphere takes place. In the solar effect mechanism, the intermediary part is now played by the warm air resulted from the heating due to the plasma. According to Palmén [21], the vertical

flow of air from the warm stratospheric zones reaches the troposphere through the tropopause funnel. The hot air which reaches the inferior atmospheric layers cools sensibly and, under the form of a descending jet, exerts a pressure on the cold air masses of the polar region. The air jet which reaches the polar zone causes a strong turbulence. Pettersen et al. [22] showed that the cold air masses from the polar region reach low latitude zones only through a strong cyclonic circulation Since the equilibrium, even in the case of small atmospheric perturbations, is concretized into undulatory motions, the air travels Southward under the form of a cold atmospheric front. During this travel, the air depression becomes more and more deep and turns into cyclone

In order to illustrate the phenomena, let us examine the development of the event 53 An E-type sunspot group appeared at −8° heliographic latitude on October 12, 1981 and became of F-type the next day The penumbra of the directional sunspots was ramified The length of the active zone reached 196 000 km On October 17 it contained 81 umbral zones On October 19, CM was reached Till October 20, the greatest umbra of the sunspot group performed a 15° clockwise rotation, and 39° more till October 22 On October 24 it reached the opposite side of the Sun This umbra kept about the same form during its visibility This was the second rotation of the active zone, the first one being performed on September 22 According to our ground observations, on October 20 the *Cirrus fibratus* clouds mark the arrival of a cyclone with outstanding cold front *Cirrocumulus lenticularis* clouds were also formed The cloudy system of the cyclone reached Salonta on October 22, constituting simultaneously the beginning of the correlational phenomenon, because in the same evening the precipitations started The precipitations from the low altitude *Nimbostratus* clouds became abundant on October 24. The temperature maximum was +18°C, as against +22°C on October 22 On October 26 we measured −1°C (first frost). The meteorological situation is given in Fig 3

According to our observations, the cyclone which followed the correlational event consists of a cloudy system covering a zone of about 4000 km and travelling rapidly due to the temperature differences between the North-West (cold air) and South-East (warm air) extremities According to Zverev [23], the travelling of the cyclone is influenced by the cold wind normal to the front We observed that the correlational cyclone travels generally along the Van Bebber trajectory of the third kind This cyclone was featured by a strong cold wind accompanied by a pronounced decrease of the air temperature, independently on season. The Rossby planetary wave ring which surrounds the pole and has a length of 5000—10 000 km is able to change, according to our observations, the form of the frontal surface at extremities the air flow which travels West-East along the latitude circles can change its direction in a relatively short interval, due to the correlational cyclone, into a meridional air flow. During the maximum solar activity of 1979, the summer semester, we could often record cumulative clouds resulted from oceanic and arctic fronts (*Cumulus* and *Cumulonimbus*) 1—2 years after the maximum solar activity, there were inundations in Central Europe as a consequence of abundant precipitations (summer 1970, 1980 and 1981) The intensity of the correlational cyclone depends on the atmospheric situation in a certain site:

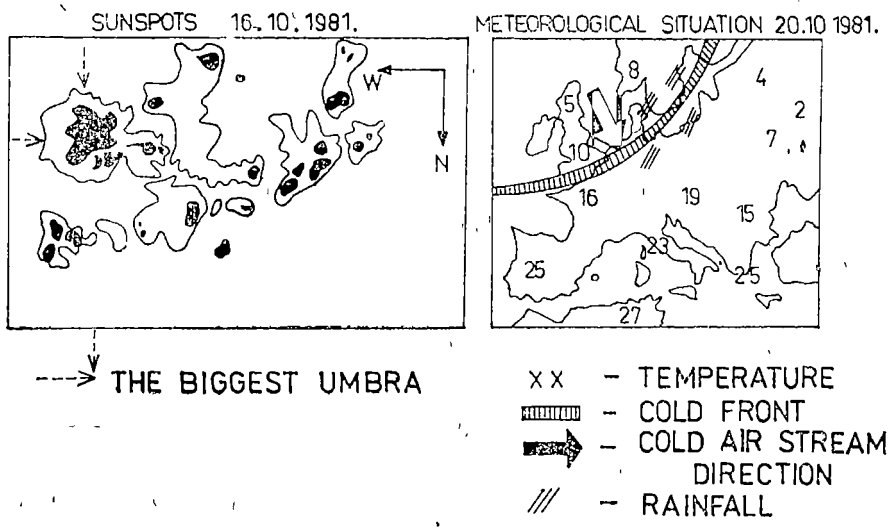

Fig 3

a) if above the Atlantic Ocean there is a cyclone in the Iceland depression zone, the correlational effect is evident (precipitations, winds, temperature decrease),

b) if above the Atlantic Ocean there is an anticyclone, the correlational cyclone has the appearance of a cold and dry front (with reduced precipitations),

c) if along the latitude of 60° there is a series of cyclones, the correlation is illustrated by a "cut-off" cyclone

During a solar cycle, the number of correlational sunspots is small as against the total number of active zones. Between September 10, 1978 and January 7, 1989, out of 658 cyclones which passed over Salonta about 80 were correlational.

The correlation between the solar activity and the terrestrial weather is apparent during short time intervals. The study of the sunspots and correlational cyclones is not difficult, it can be systematically performed [24, 25] The study of synoptic maps has a particular importance From this point of view, we emphasize the essential results of N Topor [26] obtained on the basis of a close analysis of synoptic maps, establishing 7 different possible meteorological situations Out of these ones, the sixth situation is the most adequate for our correlational event; this one ensures the circulation of cold and humid polar air masses, transported by strong winds over the Western and Central Europe, hence over our country, too.

Table 1

Coorrelational sunspots

No	DCM	So (°)	MIC	SGA	No. B	Source
1	24 Aug 1971	−13	F	1682	251	C
2	22 Oct 1971	7	F	1503	295	C
3	5 Aug 1972	13	G	1143	220	C
4	6 Jul 1973	12	C	—	93	B
5	2 Jul 1974	−11	C	—	90	B
6	4 Jul 1974	−14	F	—	92	B
7	15 Jul 1974	−9	H	—	96	B
8	22 Jul 1974	−16	D	—	104	B
9	10 Sep 1978	31	D	234	—	C
10	2 Dec 1978	−18	E	403	425	C
11	12 Dec 1978	20	E	729	—	C
12	25 Jan 1979	−3	F	—	—	A
13	8 Feb 1979	−10	D	—	—	A
14	26 Mar 1979	18	F	—	—	A
15	2 Apr 1979	−16	F	153	128	C
16	29 Apr 1979	18	E	1012	168	C
17	2 May 1979	15	D	811	175	C
18	13 Jun 1979	−17	E	671	260	C
19	19 Aug 1979	−24	E	760	407	C
20	28 Sep 1979	15	E	372	—	C
21	21 Oct 1979	15	F	—	—	A
22	9 Nov 1979	−14	F	463	603	C
23	6 Dec 1979	−14	E	401	—	C
24	30 Dec 1979	−14	E	118	—	C
25	11 Jan 1980	−12	D	833	18	C
26	5 Feb 1980	−16	F	1014	54	C
27	11 Feb 1980	−12	E	486	65	C
28	8 Mar 1980	−10	E	336	94	C
29	1 Apr 1980	26	D	461	126	C
30	24 Apr 1980	−13	E	1090	153	C
31	6 May 1980	−20	E	569	178	C
32	13 May 1980	−16	D	539	197	C
33	3 Jun 1980	−20	J	170	227	C
34	20 Jul 1980	−25	H	613	334	C
35	30 Sep 1980	−17	D	81	486	C
36	14 Oct 1980	−11	E	1056	514	C
37	23 Oct 1980	−18	E	1256	548	C
38	12 Nov 1980	−11	F	2439	585	C
39	18 Dec 1980	6	E	597	4	C
40	7 Jan 1981	−14	D	64	30	C
41	14 Jan 1981	6	D	92	45	C
42	3 Mar 1981	−12	E	510	117	C
43	8 Mar 1981	−4	E	590	125	C
44	20 Mar 1981	9	C	296	156	C
45	15 Apr 1981	9	D	282	224	C
46	1 Jul 1981	−15	F	933	378	C
47	24 Jul 1981	−8	H	1588	439	C
48	28 Jul 1981	−13	F	1774	443	C
49	18 Aug 1981	−15	F	1074	492	C
50	2 Sep 1981	−13	E	500	534	C
51	10 Sep 1981	10	F	—	572	B
52	15 Oct 1981	−18	F	1838	660	C
53	19 Oct 1981	−11	F	1825	670	C

Table 1 (*continued*)

No	DCM	So(°)	MIC	SGA	No B	Source
54	5 Nov 1981	−11	F	1463	710	C
55	1 Dec 1981	−9	E	623	766	C
56	1 Feb 1982	−14	F	1005	38	C
57	10 Feb 1982	−10	F	1792	53	C
58	18 Feb 1982	3	E	849	66	C
59	2 Mar 1982	14	H	499	84	C
60	11 Mar 1982	5	E	409	105	C
61	17 Mar 1982	−5	E	1156	120	C
62	29 Mar 1982	11	E	1236	134	C
63	13 Apr 1982	12	J	244	173	C
64	26 Apr 1982	12	D	535	200	C
65	31 May 1982	−3	E	400	265	C
66	9 Jun 1982	−9	E	908	281	C
67	12 Jun 1982	−18	E	606	287	C
68	20 Jan 1983	−13	D	252	29	C
69	3 Feb 1983	−17	H	879	43	C
70	9 May 1983	−13	D	136	140	C
71	24 May 1983	17	D	433	153	C
72	5 Jun 1983	−9	F	1160	169	C
73	11 Jun 1983	−9	E	694	171	C
74	2 Jul 1983	−8	J	155	192	C
75	19 Jul 1983	13	J	127	211	C
76	3 Aug 1983	−9	F	850	235	C
77	14 Aug 1983	−6	E	453	246	C
78	16 Jan 1984	−16	E	530	2	C
79	12 Feb 1984	−13	D	587	14	C
80	11 Mar 1984	−10	D	—	24	B
81	2 Apr 1984	−15	E	429	55	C
82	16 Apr 1984	8	E	616	68	C
83	29 Apr 1984	−12	F	—	80	B
84	31 Aug 1984	−7	D	446	175	C
85	26 Nov 1984	−12	E	452	207	C
86	12 Dec 1984	−12	D	188	214	C
87	29 Mar 1985	6	C	205	13	C
88	26 Apr 1985	4	E	776	20	C
89	14 May 1985	−12	H	381	26	C
90	7 Jul 1985	−15	D	596	56	C
91	22 Oct 1985	4	C	320	78	C

REFERENCES

1 E Ţifrea, A Dumitrescu, G Mariş, „Universul în radiaţia X", Ed ştiinţifică şi enciclopedică, Bucureşti, 1987
2 N V Pushkov, *Zemlya i vselennaya*, No 4 (1974)
3 H Israel, „Atmospharische Elektrizitat", II Band, Akademie—Verlag, Leipzig, 1961
4 A. Grigoriu, *St Cerc Geol Geogr Geofiz*, ser *Geofizică*, **9** (1) (1969), 49—54
5 E. Ţifrea, I Dumitrescu, I Buceşa, *Chirurgia*, **21** (1972), No 11, 1001—1008
6 J P Druzhinin, B J Sazonov, V N Yagodinskij, „Kosmos—Zemlya Prognozy", Moskva, Mysl, 1974
7 M Konček, „Meteorologické zpravy", č 6, HMU (1972)
8 J M Wilcox, *Science*, **192** (1976), No 4241, 745—748
9. S Ciulache, „Meteorologie Manual practic", Ed didactică şi pedagogică, Bucureşti, 1977

10 * * * „Instrucțiuni pentru observarea, identificarea și codificarea norilor și a fenomenelor meteorologice", C S A , București, 1968
11 * * * „Atlas international de nuages", O M M , Paris, 1956
12 M Waldmeier, *Die Sonne*, No **30**
13 G Kuveler, *Die Sonne*, No **30**
14 R C Willson, *J Geophys Res* , **87** (1982), 4319—4326
15 J. Pop *Astron Nachr* **302** (1981), 13—16
16 * * * *Astrophys J* , **185**, L 47
17 * * * „Sky and Tel", 1969
18 J R Hickey, *Swissair Meteorological Inst Working Report*, No **94**, 1980, 17—19.
19 E A Smith, et al , in „Proc IAMAP 3-rd Scient Assembly, Hamburg, 17—28 August 1981", Boulder, Colorado, p 18—28
20 E N Parker, "The Sun Solar System", Vol 3, San Francisco, 1975
21 E Palmén, C W Newton, "The Atmospheric Circulation Systems", Academic Press, New York, London, 1969
22 D E Petterssen, et al , Geophysica-Norvegica, 1962
23 A C Zverev, "Synopticheskaya meteorologya", Moskva, 1968
24 * * * "Observations solaires Rotations 1570—1770", Obș Astron București, Ed Acad R S R , București, 1972—1986
25 * * * "Solar Observations Made at Catania Astrophysical Observatory during 1971—1985", Ed C D d'Arrigo, Catania, Coniglione
26 E Dumitrescu, „Climatologia R S R ", Facultatea de Geografie și Geologie, Universitatea București, 1976

STUDIA UNIV BABEŞ BOLYAI, PHYSICA, XXXV, 1, 1990

EXOTIC STATISTICS IN THREE, FOUR AND HIGHER DIMENSIONS

E. VINŢELER*

Received April 3, 1990

ABSTRACT. — I conjecture that the central extension of the local algebra of observables Diff (S^{d-1}) admits as integrability structure the d-simplex equation and with this assumption I show that the statistics of d-membranes is determined by the extended braid group

In this article we describe exotic statistics for "extended particles"-D-membranes Also for them we can define the notion of "locality", but then in this "local" quantum field theory we have specific properties. If in two dimensions (algebra of observables is Diff(S^1)) we have a liniar dependence between products of 2 fields space-like separated

$$F_1F_2 = R_{12}F_2F_1 \tag{1}$$

then in d dimensions (algebra of observables is Diff(S^{d-1})) we will have a liniar dependence between products of d fields

$$F_1F_2 \quad . F_d = R_{12} \quad {}_dF_dF_d\hat{1}_1 \cdot F_1 \tag{2}$$

For relation (1) the consistence condition is Yang-Baxter equation for statistical matrix R [1] and for relation (2) is d-simplex equation [2] In this way we show that the algebra of observables Diff (S^{d-1}) admits as integrability structure the d-simplex equation and the statistics of d-membranes is determined by the extended braid group [3]

In the local quantum field theory [4] the observables act as self adjoint operators on a Hilbert space of physical states H By definition, superselection sectors are orthogonal subspaces H_j of H such that the observables map each sector into itself

$$A_j \quad H_j \rightarrow H_j \tag{3}$$

The set of observables with property of locality

$$[A, B] = 0 \text{ if } A \in \mathrm{A}(I), \ B \in \mathrm{A}(I') \tag{4}$$

where I and I' are relatively spacelike, make up local algebras of observables A(I) In our case the algebra of observables is the central extension of Diff(S^{d-1}), in two dimensions is Virasoro algebra [5]

Besides observables we introduce fields which carry charges They make transitions between different superselection sectors We make up algebra F of

* *University of Cluj-Napoca, Department of Physics, 3100 Cluj-Napoca, Romania*

all field operators adding to algebra of observables A the localized morphisms ρ of the algebra A.

The superselection sectors carry inequivalent irreducible positive energy representations π_j of the algebra of observables A If vacuum sector H_0 carry representation π_0 then morphism ρ_j $A \to A$ will have the property

$$\pi_j \simeq \pi_0 \circ \rho_j \text{ with } (\pi_0 \circ \rho)(A) = \pi_0(\rho(A)), \ A \in A \tag{5}$$

The morphism ρ is localized in domain I if.

$$\rho(A) = A, \text{ for } A \in A(I') \tag{6}$$

whenever I and I' are localized relatively spacelike

The morphism ρ_j $\pi_j \to \pi_0$ can be defined by means of the unitary transformation V_j $H_j \to H_0$

$$\rho_j(A_1) = V_j A_j V_j^{-1} \tag{7}$$

The charged field $F_j : H_0 \to H_j$ implement the localized morphism ρ_j $\pi_j \to \pi_0$:

$$A_j F_j = F_1 \rho_j(A_j) \tag{8}$$

where A_j is the observable which act on H_j, or using (7) relation (8) became.

$$A_j B_j = B_j A_j \tag{8'}$$

with $B_j : H_j \to H_j$, $B_j = F_j V_j$

The field algebra $\mathfrak{F}_{\text{free}}$ is generated by observables $A \in A$ and by elements

$$F_{i_1} F_{i_2} \ldots F_{i_n} A, \ A \in A \tag{9}$$

The free field algebra $\mathfrak{F}_{\text{free}}$ is not faithfully represented on Hilbert space H, and we have some additional conditions which restrict $\mathfrak{F}_{\text{free}}$ to the physical field algebra $\mathfrak{F}_{\text{phys}}$. These extra conditions are determined by the existence of intertwiners T.

By definition, an intertwiner T between morphisms ρ and σ is an observable $T \in A$ such that

$$T\rho(A) = \sigma(A)T, \ A \in A \tag{10}$$

T with property (10) spann the linear space Homm (ρ, σ).

It is easy to show that if $T \in \text{Homm}(\rho, \sigma)$, $S \in \text{Homm}(\sigma, \tau)$ then $ST \in \text{Homm}(\rho, \tau)$ and $T \in \text{Homm}(\rho_0 \tau, \sigma \circ \tau)$, $\tau(T) \in \text{Homm}(\tau \circ \rho, \tau \circ \sigma)$

Let's find the intertwiner T_{12} such that.

$$F_2 F_1 = T_{12} F_1 F_2 \tag{11}$$

From (8) we have:

$$AF_1 = F_1 \rho_1(A), \ AF_2 = F_2 \rho_2(A) \tag{12}$$

then.

$$AF_1 F_2 = F_1 \rho_1(A) F_2 = F_1 F_2 (\rho_2 \circ \rho_1)(A) \tag{13}$$

and

$$BF_2F_1 = F_2\rho_2(B)F_1 = F_2F_1(\rho_1 \circ \rho_2)(B) \tag{13'}$$

From (10) we have

$$T_1\rho(A) = \rho_1(A)T_1,\ T_2\rho(A) = \rho_2(A)T_2 \tag{14}$$

Through some calculations we obtain:

$$\rho_1(A)F_1F_2\rho_1(T_2)TT_2^{-1}\rho_2(T_1^{-1}) = F_1F_2\rho_1(T_2)T_1T_2\rho_2(T_1^{-1})\rho_1 \circ \rho_2 \circ \rho_1(A) \tag{15}$$

If in (15) we replace $\rho_1(A)$ by B we see that (15) coincide with (13') if:

$$F_1F_2\rho_1(T_2)T_1T_2^{-1}\rho_2(T_1^{-1}) = F_2F_1 \tag{16}$$

hence from (11).

$$T_{12} = \rho_1(T_2)T_1T_2^{-1}\rho_2(T_1^{-1}) \tag{17}$$

The relation (11) is valid in two dimensions for the observable algebra Diff (S^1). If instead of (11) we want to fulfill (2) knowing that A is a C^*-algebra (we do not approach the case of von Neumann algebras related with subtle considerations about Haag duality [6]), we consider that the products of the form (17) do not take place in the observable algebra A, In other words this means that we restrict the two-dimensional physical field algebra F_{phys} even more The restriction is analogously to that in the Sine-Gordon theory where are obtained new minimal conformal series at criticality [7]. In our case through the restriction we obtain the conformal theories in higher dimensions

Now we can write $F_3F_2F_1$ in two different ways

$$F_3F_2F_1 = \rho_3(T_{12})T_{13}\rho_1(T_{23})F_1F_2F_3 \tag{18}$$

or:

$$F_3F_2F_1 = T_{23}\rho_2(T_{13})T_{12}F_1F_2F_3 \tag{19}$$

where T_{ij} is the intertwiner from Homm $(\rho_i \circ \rho_j,\ \rho_i \circ \rho_i)$ and we obtain the braid equation

$$\rho_3(T_{12})\ T_{13}\rho_1(T_{23}) = T_{23}\rho_2(T_{13})T_{12} \tag{20}$$

For $\rho_1 = \rho_2 = \rho_3 = \rho$ (20) became

$$\rho(T_{\rho 2})T_{\rho 2}\rho(T_{\rho 2}) = T_{\rho 2}\rho(T_{\rho 2})T_{\rho 2} \tag{21}$$

Another relation is [5]

$$T_{\rho 2}\rho\ (T_{\rho 2}) = \rho^k(T_{\rho 2})T_{\rho 2} \tag{21'}$$

The braid group B_n acts on $\rho^n(A)$ through the application

$$s_i \to T_{s_i} = \rho^{i-1}(T_{\rho 2}) \tag{22}$$

where $T_{\rho 2}$ Homm (ρ^2, ρ^2)

Then the defining relations for B_n are:

$$s_i s_{i+1} s_i = s_{i+1} s_i s_{i+1} \tag{23}$$

$$s_i s_j = s_j s_i \,, \quad |i - j| \geqslant 2 \tag{23'}$$

If we note by $A_{(d)}$ the observable algebra in d dimensions we can obtaine $A_{(d+1)}$ from $A_{(d)}$ eliminating the intertwiners $T_{i_1 i_2 \ldots i_d}$ from $\mathrm{Hom}\,(\rho_{i_1} \circ \rho_{i_2} \circ \ldots \circ \rho_{i_d}, \rho_1 \circ \rho_2 \ldots \circ \rho_d)$. On this way the intertwiners in $A_{(d)}$ will obey the d-simplex equation. For example in three dimensions $F_3 F_2 F_1 = T_{123} F_1 F_2 F_3$ and as we have not the intertwiners T_{ij} instead the braid equation we will have the extended braid equation

If we want to generalize the relations between intertwiners to higher dimensions, instead of equations (18), (19) we will suppose that exists an intertwiner so that:

$$F_1 F_2 F_3 = T F_3 F_1 F_2 = T^2 F_2 F_3 F_1 \tag{24}$$

The generalization is straigthforward:

$$F_1 F_2 \ldots F_{d+1} = T F_{d+1} F_1 F_2 \ldots F_d = \ldots = T\, F_2 F_3 \qquad F_{d+1} F_1 \tag{25}$$

The equation (24) gives us the defining relations for the extended braid group $B_{3,(2)}$:

$$s_1 s_2 = s_2 s_3 = s_3 s_1 \tag{26}$$

For $B_{n(2)}$ we have $n - 2$ versions of equation (26):

$$s_1^{(i)} s_2^{(i)} = s_2^{(i)} s_3^{(i)} = s_3^{(i)} (s_1^{(i)} \qquad 1 \leqslant i \leqslant n - 2$$

and:

$$s_2^{(i)} = s_1^{(i+1)} \qquad 1 \leqslant i \leqslant n - 3 \tag{27}$$

$$s_1^{(i)} \cdot s_2^{(k)} = s_2^{(k)} \quad s_1^{(i)} \qquad i \neq k \tag{27'}$$

It can be easily seen that $B_{n,(2)}$ coincides with B_n

From the equation (25) we have the defining relations for the extended braid group $B_{d+1,(d)}$.

$$s_1 s_2 \ldots s_d = s_2 s_3 \ldots s_{d+1} = s_3 s_4 \ldots s_{d+1} s_1 = \ldots = s_{d+1} s_1 \ldots s_2 \tag{28}$$

Analogously to $B_{n,(2)}$ for $B_{n,(d)}$ we have $n - d$ versions of (28), and the equations (27).

It is known that the particles which satisfy an exotic statistics are responsable for different interesting phenomena. the fractional quantum, Hall effect, the high temperature supercondctivity (anyons) and so on I think that the particles which satisfy the extended braid statistics $B_{n,(4)}$ may be responsable for confinement in the quantum chromodinamics.

REFERENCES

1 J Fröhlich, "Statistics of fields, the Yang—Baxter equation and the theory of knots and links Proceedings of the 1987 Cargese School"
2 J M Maillett, F W Nijhoff, *Phys Lett*, **224 B**, 389 (1989); **229 B**, 71 (1989)
3 E Vinteler, "Extended braid group in higher dimensional integrable theories" (to appear)
4. S Doplicher, R Haag, J E Roberts, *Comm Math Phys*, **23**, 199 (1971), **35**, 49 (1974)
5 K. Fredenhagen, K H. Rehren, B Schroer, *Comm Math Phys.*, **125**, 201 (1989), G Mack, V Schomerus, "Endomorphisms and Quantum symmetry of the Conformal Ising Model", preprint DESY 90—028 (1990)
6 D Buchholz, H Schultz-Mirbach," Haag Duality in Conformal Quantum Field Theory", preprint DESY 90—040 (1990)
7 D Bernard, A Leclair, "Residual Quantum symmetries of the Restricted Sine—Gordon Theories", preprint CLNS 90/974, SPhT 90—009 (1990)

STUDIA UNIV. BABEŞ-BOLYAI, PHYSICA, XXXV, 1, 1990

SPECIFIC HEAT JUMP FOR 2D-HIGH Tc SUPERCONDUCTORS

I. GROSU* and M. CRIŞAN*

Received · February 23, 1990

ABSTRACT. — The temperature dependence of the order parameter in a two dimension superconductor has been calculated. The specific heat jump at the critical temperature was evaluated and the result will be discussed in connection with the high—temperature superconductivity

1. **Introduction.** One of the most important features of the high-temperature superconductivity (HTS) is the two dimensional (2D) character of the electronic states. For a square lattice, in the tight-binding approximation the energy is.

$$\varepsilon(\vec{p}) = -2t\,(\cos p_x a + \cos p_y a) \tag{1}$$

where „a" is the lattice constant and "t" the transfer integral.

In the half-filled aproximation the density of states is:

$$N(\varepsilon) = \frac{1}{2\pi^2 t} \cdot \theta(4t - \varepsilon) \cdot K^0\sqrt{1 - (\varepsilon/4t)^2)} \tag{2}$$

where $K_0(x)$ is the complete elliptic integral of the first kind and $\theta(x)$ is th step function. If we consider ω_c the maximum energy on the energy scale and $\frac{\omega_c}{4t} \ll 1$ the equation (2) can be approximated as [1].

$$N(\varepsilon) \simeq C \cdot ln\frac{D}{|\varepsilon|} \tag{3}$$

where $D = 4t$ and C is a constant.

The two dimensional behaviour of the HTS described by (3) has been analysed by Crisan [2] and it was showed that in the weak coupling limit the ratio $\frac{2\Delta_0}{K_B T_C}$ is different from the BCS limit.

The critical temperature T_C in a 2D-HTS has been calculated by Crişan and Vacaru [3] using the Coherent Potential Approximation (CPA) and it was showed that T_C is sensitive to the dimensionality of the electronic system In this paper we will consider the influence of the energy-dependent density of states on the specific heat jump.

* *University of Cluj-Napoca, Department of Physics, 3400 Cluj-Napoca, Romania*

In order to calculate the specific heat jump we have to evaluate the temperature dependence of the order parameter $\Delta(T)$ near the critical temperature.

2. **The order parameter** The equation for the order parameter has the form.

$$1 = \frac{V}{2}\int_{-\omega_D}^{+\omega_D} d\varepsilon \cdot \frac{N(\varepsilon)}{\sqrt{\varepsilon^2 + \Delta^2(T)}} \cdot \tanh\left(\frac{\sqrt{\varepsilon^2 + \Delta^2(T)}}{2K_BT}\right) \tag{4}$$

where V is the attractive interaction, ω_D the Debye energy and T is the temperature

Using the relation:

$$\tanh\frac{x}{2} = 4x\sum_{n=0}^{\infty}\frac{1}{x^2 + \pi^2(2n+1)^2} \tag{5}$$

the equation (4) can be approximated by

$$1 = \frac{2V}{\beta}\int_{-\omega_D}^{+\omega_D} d\varepsilon \cdot N(\varepsilon)\sum_{n=0}^{\infty}\frac{1}{\varepsilon^2 + \omega_n^2} - \frac{2V}{\beta}\int_{-\omega_D}^{+\omega_D} d\varepsilon \cdot N(\varepsilon)\sum_{n=0}^{\infty}\frac{\Delta^2(T)}{(\varepsilon^2 + \omega_n^2)^2} \tag{6}$$

where: $\omega_n = \pi K_B T\,(2n+1)$ and $\beta = \frac{1}{K_BT}$

The equation (6) is valid near T_C and will be rewritten as:

$$1 = \frac{V}{2}\int_{-\omega_D}^{+\omega_D} d\varepsilon \cdot \frac{N(\varepsilon)}{\varepsilon} \cdot \tanh\frac{\beta\varepsilon}{2} - \frac{2V}{\beta}\int_{-\omega_D}^{+\omega_D} d\varepsilon \cdot N(\varepsilon)\sum_{n=0}^{\infty}\frac{\Delta^2(T)}{(\varepsilon^2 + \omega_n^2)^2} \tag{7}$$

The equation for the critical temperature T_C:

$$1 = \frac{V}{2}\int_{-\omega_D}^{+\omega_D}\frac{d\varepsilon}{\varepsilon} \cdot C\ln\frac{D}{|\varepsilon|} \cdot \tanh\frac{\beta_C\varepsilon}{2} \tag{8}$$

has the form

$$\frac{1}{VC} \simeq A \cdot ln^2\left(\frac{2K_BT_C}{D}\right) \tag{9}$$

$\left(A = \frac{1}{2}\right)$ and using (9) we get from (7):

$$A \cdot \left\{ln\left(\frac{2K_BT_C}{D}\right)^2\right\} \cdot ln\frac{T}{T_C} \simeq \frac{1}{\beta_C}\ \Delta^2(T) \cdot \left[\frac{\pi}{(\pi K_BT_C)^3} \cdot \frac{7}{8}\zeta(3) - \sum_{n=0}^{\infty}\frac{\pi}{\omega_n^3} ln\frac{\omega_n}{D}\right] \tag{10}$$

From this equation we calculate the order parameter as.

$$\Delta^2(T) = \alpha^2 T_c^2 \left(1 - \frac{T}{T_C}\right) \tag{11}$$

where :

$$\alpha^2 = \frac{A(4\pi K_B)^2 \ln\left(\frac{D}{2K_B T_C}\right)}{7\varsigma(3)\left[1 + \ln\left(\frac{D}{\pi K_B T_C}\right) - \frac{8}{7\varsigma(3)} \sum_{n=0}^{\infty} \frac{ln(2n+1)}{(2n+1)^3}\right]} \tag{12}$$

With these results we can calculate the specific heat jump near the critical temperature

3 **The specific heat.** In order to calculate the specific heat jump we will use the general result [4]

$$C_S - C_N = K_B \beta_C^3 \left(\frac{\partial \Delta^2}{\partial \beta}\right)\Big|_{\beta=\beta_C} \int_{-\omega_D}^{+\omega_D} d\varepsilon \; N(\varepsilon) \cdot \frac{e^{\beta_C \varepsilon}}{(1 + e^{\beta_C \varepsilon})^2} \tag{13}$$

This equation can be transformed using (3) as :

$$C_S - C_N = K_B \beta_C^2 \cdot C \left(\frac{\partial \Delta^2}{\partial \beta}\right)\Big|_{\beta_C} \left\{ \int_0^{\beta_C \omega_D} \frac{dx}{x} \cdot \tanh \frac{x}{2} + \tanh\left(\frac{\omega_D}{2K_B T_C}\right) \cdot ln\left(\frac{D}{\omega_D}\right) \right\} \tag{14}$$

and using for the gap the equation (11) we get :

$$C_S - C_N = C\alpha^2 T_C \left\{ \int_0^{\beta_C \omega_D} \frac{dx}{x} \tanh \frac{x}{2} + \tanh\left(\frac{\omega_D}{2K_B T_C}\right) \cdot ln\left(\frac{D}{\omega_D}\right) \right\} \tag{15}$$

The specific heat for the normal state is :

$$C_N = 2K_B \beta^2 \int d\varepsilon \cdot N(\varepsilon) \cdot \frac{\varepsilon^2 \cdot e^{\beta\varepsilon}}{(1 + e^{\beta\varepsilon})^2} \tag{16}$$

and using for the density of states the equation (3) we get.

$$C_N = 2CK_\beta^2 \Phi \cdot T \tag{17}$$

where

$$\Phi = \left\{ (\beta\omega_D)^2 \cdot \left[\ln \frac{D}{\omega_D} + 1\right] \cdot \left(1 - \tanh \frac{\beta\omega_D}{2}\right) + 2\left[\ln \frac{\beta D}{2} + 2 - \frac{\pi^2}{12}\right] \right\} \tag{18}$$

With these results we can calculate the specific heat ratio for $T \to T_C$ as

$$\frac{C_S - C_N}{C_N} = \frac{F(T_C)}{2\Phi(T_C)} \left\{ \int_0^{\beta_C \omega_D} \frac{dx}{x} \tanh \frac{x}{2} + \tanh\left(\frac{\omega_D}{2K_B T_C}\right) \cdot \ln\left(\frac{D}{\omega_D}\right) \right\} \tag{19}$$

where :

$$F(T_C) = \frac{A \quad (4\pi)^2 \quad \ln\left(\frac{D}{2K_BT_C}\right)}{7\varsigma(3) \quad \left[1 + \ln\left(\frac{D}{\pi K_BT_C}\right) - \frac{8}{7\varsigma(3)} \cdot \sum_{n=0}^{\infty} \frac{\ln(2n+1)}{(2n+1)^3}\right]} \tag{20}$$

Using now the parameters

$$\omega_D \approx 600\ \mathrm{K}, \quad D \approx 50\,\omega_D\,; \quad T_C \approx 30\ \mathrm{K}\,; \quad \beta_C\omega_D \gg 1$$

we get :

$$\frac{C_S - C_N}{C_S} \simeq 2 \tag{21}$$

4 **Discussions.** The dimensionality effects in the specific heat have been calculated in order to understand the anomaly in the hightemperature superconductors. The ratio Δ_C/C_N depends on the parameters D and ω_D in agreement with the previous result [2] obtained for $\frac{2\Delta_0}{K_BT_C}$ However, for realistic parameters we get (see 21) small deviations from BCS.

REFERENCES

1. J Labbé, J Bok, *Europhys Lett*, **3**, 1225 (1987)
2 M Crișan, *Z Phys*, **74**, 151 (1989)
3 M Crișan D Văcaru, *Z Phys*, **76**, 159 (1989)
4 J P Carbotte, A. Abd El-Rahman, *Can J Phys*, **60**, 1029 (1982)

STUDIA UNIV BABEŞ-BOLYAI, PHYSICA, XXXV, 1, 1990

THE ASYMPTOTICAL BEHAVIOUR OF DISCRETE DYNAMICAL SYSTEMS IN CHAOS

ZOLTÁN TOROCZKAI*

Received February 12, 1990

ABSTRACT. — This paper discusses the formation of the attractors of one-dimensional, discrete dynamical systems and their stability properties using the most general way that is possible and its purpose is the description of the phase space structure's formation during the evolution of dynamics To be able to reach this purpose I introduced a time dependent quantity (the natural procent), which led to the discovering of new properties certain chaotical dominions as intermittency for example (see section 3)

The described method — which can be called fluctuation-analysis — renders possible a new experimental approximation in the inverstigation of chaos (see the last section)

1. **Introduction.** The notion of natural measure is linked to a probability property of the attractors. According to this property to the different regions of the attractor belongs different "visiting" frequencies along the trajectory, or otherwise they have different probabilities This property is mainly used in the definition of the natural measure dimensions which is a part of the attractors' characteristical dimensions. (1, 2) (the generalized Rényi dimensions for example) Following ref. [1], the natural measure is that probability measure (defined on the attractor) which is defined in the followings: let us take a limited volume C (cube) from the phase space and an x_0 point from the basin of attraction of the attractor. The natural measure which belongs to the cube C referring to the trajectory which was started from x_0, is:

$$\mu(x_0, C) = \lim_{t\to\infty} \mu_t(x_0, C) \qquad (1)$$

where $\mu_t(x_0, C)$ is the time fraction spent in the volume C by the trajectory. The natural measure gives the relative probability of different regions of the attractor as obtained from time averages.

1.1. *The notion of natural procent* Being confined to case of one-dimensional, discrete maps, let's transcribe (1) using other notations. Let us consider the attractor in the [0, 1] interval (the maps which are in the class of MSS[3] functions have this property). Now divide the interval [0, 1] into N intervals which have equal length ($\varepsilon = 1/N$). The i^{th} interval (which coresponds to the cube C) is $[i\varepsilon, i(\varepsilon + 1)]$ where $i = 0, 1, 2, \ldots N$.

* *University of Cluj-Napoca, Department of Physics, 3400 Cluj-Napoca, Romania*

We define — along a trajectory — a quantity called natural procent referring to the i^{th} interval as:

$$p_i(x_0, K) = \frac{t_i(x_0, K)}{K} \tag{2}$$

where x_0 is the initial point of trajectory, and $t_i(x_0, K)$ is the number of iteratons which are exactly in the i^{th} interval from the whole K number of iterations.

Of course $p_i(x_0, K) \leqslant 1$ for any $x_0 \in [0, 1]$, $K \in N$ and $i \in \{0, 1, \ldots N\}$.

We can notice that

$$\pi_i(x_0) = \lim_{k \to \infty} p_i(x_0, K) \tag{3}$$

is the natural measure of the i^{th} interval with the assumption that the above limit exists. Further on we are going to investigate the asymptotical behaviour of the (2) quantity.

2. The asymptotical stability of the attractors.

— after T iterations

$$p_i(x_0, T) = \frac{t_i(x_0, T)}{T}$$

— taking K iterations but starting from x_T this time:

$$p_i(x_0, T + K) = \frac{t_i(x_0, T + K)}{T + K} = \frac{t_i(x_0, T) + t_i(X_T, K)}{T + K}$$

so

$$p_i(x_0, T + K) = \left[p_i(x_0, T) + \frac{K}{T} p_i(X_T, K)\right]\left(1 + \frac{K}{T}\right)^{-1} \tag{4}$$

let's introduce

$$f_i(x_0, T, K) = p_i(x_0, T + K) - p_i(x_0, T) \tag{5}$$

quantity with fluctuation character, which will characterize the asymptotical behaviour of the natural procent ($T \gg 1$).

— using (4):

$$f_i(x_0, T, K) = [p_i(x_T, K) - p_i(x_0, T)] \frac{K}{K + T} \tag{6}$$

In practice the limit in (3) can't be calculated using an analytical method, so the investigation of the probability distribution on the attractor will use the asymptotical values of the natural procents.

Let's fix the value of K (optionally), and let's increase T unlimitedly.

Now using (4) we get the following important expression:

$$\lim_{T \to \infty} f_i(x_0, T, K) = \lim_{T \to \infty} \left\{ p_i(x_T, K) - p_i(x_0, T) \frac{K}{K + T} \right\} = 0 \tag{7}$$

Determining the natural procents for every i^{th} interval near $T \gg 1$, then representing all these, we get the figure of the probability distribution (see fig 1 d)

But a question exists how much differs the distribution figure in the case when we iterate with a given $T + K \gg 1$ value from the one in case we iterate until $T \ll 1$? The (7) equality gives the answer: the difference between the two curves can be considered a very little value, if T is high enough, due to the fact that K is fixed and the factor $K/(K + T)$ decreases unlimitedly with the increasing of T So we can enunciate:

THEOREM 1. *The probability measure which is formatted on the attractor (natural measure) is asymptotically stable taking into consideration the limited numbered iterations, so* (with the assumption that (3) exits):

$$f_i(x_0, \infty, K) = 0 \quad \text{for any } x_0 \in [0, 1],\ K \in N \text{ and } i \in \{0, \ldots, N\}$$

If we want to detect the changes of the procent p_i along a trajectory, then the time interval of the experiment (or iteration number) must have a same scale (order) than the one of the distribution which had formated until that moment The detect of fluctuation goes using (6) If $K \sim T$, then the factor above doesn't have any importance at all and f_i is measurable Further on we take the $T = K$ case in the calculations just as in the measurements

2 1 *Scaling properties* In this section I'm going to present another aspect of the asimptotical stability in the respect of the time intervals' largeness (K) Let's take the following measurement series, in which the measured quantity is the $p_i(x, K)$ natural procent in the i^{th} interval and the time interval is K:

$$\xrightarrow[x_0]{p_i(x_0, K)} \cdot \xrightarrow[x_k]{p_i(x_k, K)} \cdot \xrightarrow{} \cdots \xrightarrow[x_{nk}]{p_i(x_{(n-1)k} K)} \cdot \xrightarrow{} \cdots$$

let

$$< p_i(x_0, K) >^{(n)} = \frac{1}{n} \sum_{k=0}^{n-1} p_i(x_{nk}, K) \tag{8}$$

Let's assume that we have made n measurements We can write in this case.

$$< p_i(x_0, K) >^{(n)} = \frac{t_i(x_0, K) + t_i(x_k, K) + \ldots + t_i(x_{(n-1)k}, K)}{n \quad K} = \frac{t_i(x_0, nK)}{nK}$$

then

$$p_i(x_0, K) >^{(n)} = p\ (x_0, nK) \tag{9}$$

To the whole trajectory ($n = \infty$)

$$< p_i(x_0, K) >^{\infty} = \lim_{n \to \infty} \frac{1}{n} \sum_{k=0}^{n-1} p_i(x_{hk}, K) = \lim_{n \to \infty} < p_i(x_0, K) >^{(n)}$$

taking into consideration (9) and (3) it follows:

$$< p_i(x_0, K) >^{\infty} = \pi_i(x_0) \tag{10}$$

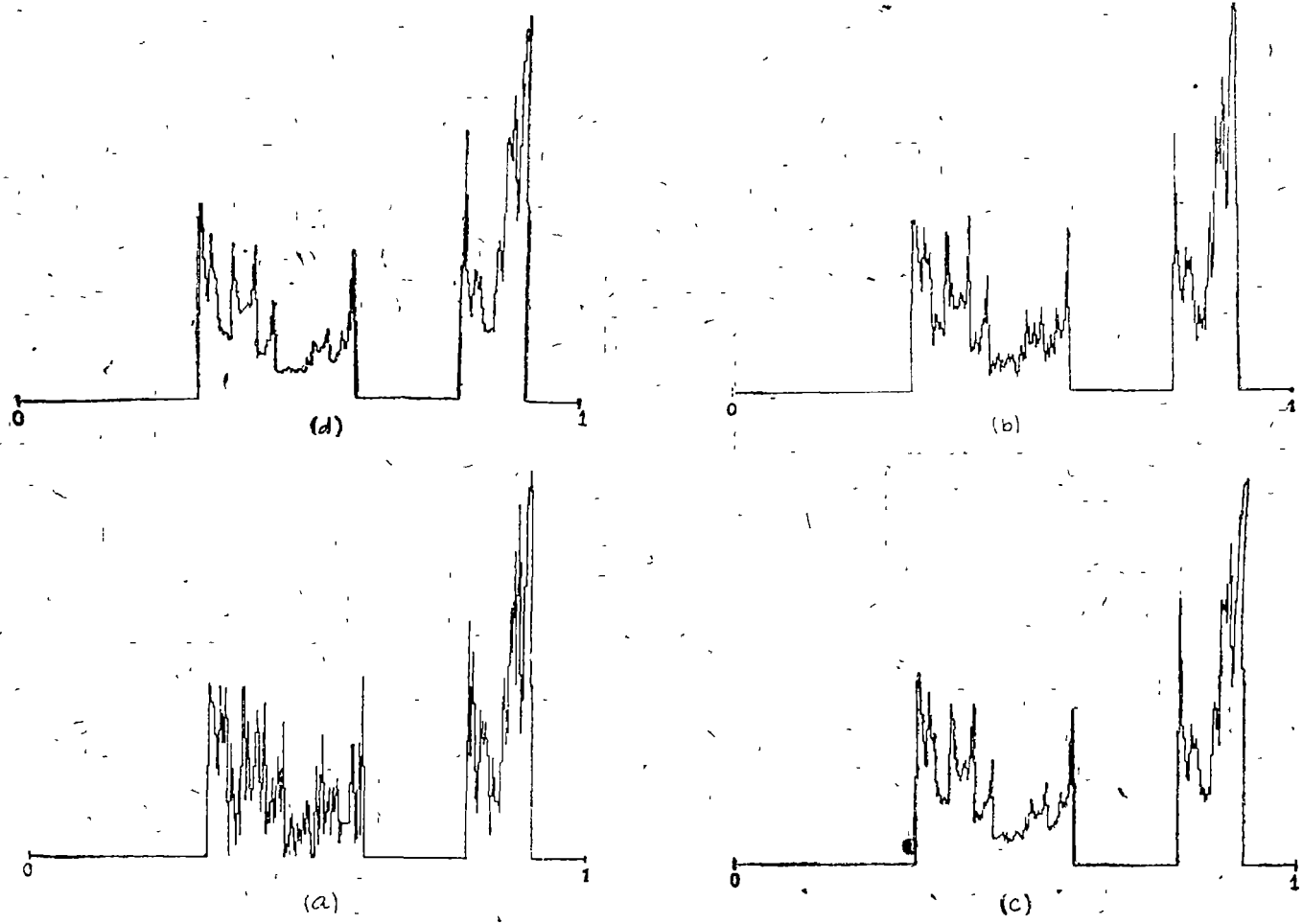

Fig 1 Probability distribution on the attractor of the logistical map at $r = 3{,}6$ for different iteration numbers a) $K = 10^3$, b) $K = 5 \cdot 10^3$, c) $K = 30 \cdot 10^3$, d) $K = 200 \cdot 10^3$, $(N = 300)$

so this is independent of K, — of the time—and it's just the natural measure of the i^{th} interval.

Let's develop the variance

$$\sigma_i^{(n)2}(x_0, K) = \frac{1}{n}\sum_{j=0}^{n-1}[p_i(x_{jk}, K) - <p_i(x_0, K)>^{(n)}]^2 \tag{11}$$

using (8) and a suitable index exchange

$$\sigma_i^{(n)2}(x_0, K) = \frac{1}{n^3}\sum_{h_1, h_2, h_3=0}^{n-1}\Delta_i^{(k)}(h_1, h_2)_0 \quad \Delta_i^{(k)}(h_1, h_3)_0 \tag{12}$$

where

$$\Delta_i^{(k)}(h_1, h_2)_0 = p_i(x_{h_1 k} K) - p_i(x_{h_2 k}, K) \tag{13}$$

The (13) quantities can be taken for the elements of a matrix(nxn type). Let's call this the fluctuation-matrix and let's mark it with $\overline{\overline{f}}_i(x_0, K)_n$.

$$\overline{\overline{f}}_i(x_0, K)_n = \begin{vmatrix} 0 & p_i(x_0, K) - p_i(x_n, K) & \dots \\ p_i(x_k, K) - p_i(x_0, K) & 0 & \dots \\ \cdot & \cdot & \dots \\ \cdot & \cdot & \dots \\ \cdot & \cdot & \dots \end{vmatrix}$$

If we make "∞" measurements on the trajectory, then $\overline{f}_i$ is a matrix with infinite rows and columns. Using (12)

$$\sigma_i^{(n)2}(x_0, K) = -\frac{1}{h^3}\sum_{h_2, h_3=0}^{n-1}\{\overline{\overline{f}}_i(x_0, K)_n\}_{h_2, h_3}$$

where $\{\overline{\overline{f}}_i^2(x_0, K)_n\}$ marks the h_2h_3 element of the $\overline{\overline{f}}_i^2(x_0, K)_n$ symmetrical matrix

Let's introduce the $\mathfrak{R}$ linear functional defined on the linear space of the $n \times n$ symmetrical matrixes, with the next relation:

$$\mathfrak{R}(\overline{\overline{A}}) = \sum_{i,j=0}^{n-1} a_{ij}, \quad \text{where} \quad \overline{\overline{A}} = [a_{ij}], \; i, j = \overline{0, n-1}$$

Using these marks the variance will be

$$\sigma_i^{(n)2}(x_0, K) = -\frac{1}{n^3}\mathfrak{R}(\overline{\overline{f}}_i^2(x_0, K)_n) \tag{14}$$

on the whole trajectory

$$\sigma_i^2(x_0, K) = \lim_{n\to\infty}\left[-\frac{1}{n^3}\mathfrak{R}(\overline{\overline{f}}_i^2(x_0, K)_n\right] \tag{15}$$

* * *

Now let's choose a new $T = mK, m \gg 1$, $m \in N$, "time-unite" on the discrete time-scale. Let's calculate the above quantities and express them with the corresponding quantities which are concerning the K^{th} measurements. It's valid.

$$p_i(x_0, T) = p_i(x_0, mK) = \frac{1}{m} \sum_{j=0}^{m-1} p_i(x_k, K). \tag{16}$$

and

$$p_i(x_{kT}, T) = \frac{1}{m} \sum_{j=0}^{m-1} p\,(x_{(km+j)k}, K) \tag{16'}$$

if we have made n measurements

$$< p_i(x_0, T) >^{(n)} = \frac{1}{nm} \sum_{l=0}^{nm-1} p_i(x_{lk}, K) = < p_i(x_0, k) >^{(nm)} \tag{17}$$

namely, the same average. From (9)

$$< p_i(x_0, T) <^{(n)} = p_i(x_0, nT) = p_i(x_0 nmk) \tag{18}$$

Let's study the variance

$$\sigma_i^{(n)^2}(x_0, T) = \frac{1}{n} \sum_{j=0}^{n-1} [p_i^2(x_{jT}, K)] = < p_i(x_{0i} T) >^{(n)^2}$$

Since the n measurements with T time-unit contains mn measurements with K unit:

$$\sigma_i^{(nm)^2}(x_0, T) = \frac{1}{nm} \sum_{k=0}^{nm-1} p_i^2(x_{hk}, K) - < p_i(x_0, K) >^{(nm)^2}$$

rom (16), (16'), (17), (18) result

$$\sigma_i^{(n)^2}(x_0, T) = \sigma_i^{(nm)^2}(x_0, K) - \frac{1}{n} \sum_{j=0}^{n-} \sigma_i^{(m)^2}(x_{jT}, K) \tag{19}$$

expression which gives the searched relation between the variances measured with different time-units The second expression on the right of the (19) is exactly the average of the m variance started from the different x_{jT} points ($j = \overline{0, n-1}$ with K time-unit. On the whole trajectory

$$\sigma_i^2(x_0, T) = \sigma_i^2(x_0, K) - \lim_{n \to \infty} \frac{1}{n} \sum_{j=0}^{n-1} \sigma_i^{(m)^2}(x_{jT}, K) \tag{20}$$

approximating the average in (19) with the first element

$$\sigma_i^{(n)^2}(x_0, T) \cong \sigma_i^{(nm)^2}(x_0, K) - \sigma_i^{(m)^2}(x_0, K) \tag{21}$$

and taking this to the whole trajectory

$$\sigma_i^2(x_0, T) \cong \sigma_i^2(x_0, K) - \sigma_i^{(m)^2}(x_0, K) \tag{22}$$

We can observe from (19) that $\sigma_i^{(n)^2}(x_0, T) < \sigma_i^{(nm)^2}(x_0, K)$ which means that the variances (the "width" of the fluctuations) decreases while increasing the time-unit Since $\lim_{m\to\infty} \sigma_i^{(m)^2}(x_0, K) = \sigma_i^2(x_0, K)$, so if $m \to \infty$ then $\sigma_i^2(x_0, T) \to 0$ which is exactly another expression of the asymptotical stability. We can enunciate.

Theorem. *increasing the time-unit of measurements, the width of the natural procents' fluctuations is decreasing and*

$$\lim_{T\to\infty} \sigma_i^2(x_0, T) = 0 \tag{23}$$

Observations · 1) using the formalism initiated in the (12)—(15) expressions we can observe that the matrix-language can be able to describe the natural procents' fluctuations. If we put the (14) compact expression of the variances into (19):

$$\Re\left(\frac{1}{n^3}\overline{\overline{f_i}}^2(x_0, T)_n - \frac{1}{n^3 m^3}\overline{\overline{f_i}}^2(x_0, K)_{nm} + \frac{1}{n}\sum_{j=0}^{n-1}\frac{1}{m^3}\overline{\overline{f_i}}^2(x_{jT}, K)_m\right) = 0$$

and also into the (21)

$$\Re\left(\frac{1}{n^3}\overline{\overline{f_i}}^2(x_0, T)_n - \frac{1}{n^3 m^3}\overline{\overline{f_i}}^2(x_0, K)_{nm} + \frac{1}{m^3}\overline{\overline{f_i}}^2(x_0, K)_m\right) \cong 0$$

we obtain the above equalities. This formalism will be investigated in the nearest future;

2) we can associate the following physical meaning to the asymptotical stability which was expressed in the 1 and 2 theorems: the formation of the structure of the phase space is going on as the system was linked to a termostat which is characterized by the equations of dynamics and by the attractor in geometrical sense It's due to the fact that the dynamics is given with determinístical equations,

3) we were confined only to the one-dimensional discrete systems and to the existence of (3) but the above study can be generalized to n-dimensional dynamicswith the same valid theorems,

4) it's not necessary to chose a $T = mK$. For any $T > K$ exist m and q so that $T = mK + q$, $q < K$ The calculated quantities are differing only in an negligible term from the former ones and the 2nd theorem is also valid.

3 The fluctuational-analysis as an experimental method. This section presents a numerical application on the welliknown logistical map. The measurements were made with $N = 300$ using a fixed division of the [0, 1] interval ($\varepsilon = 3\,34 \cdot 10^3$).

On the I. a—d figures the probability distribution on the attractor is represented for different iteration-numbers and with the same $x_0 = 0.3$ starting point using a fasten controllparameter value $r = 3\,6$ We can observe that the difference between the I a and I b figures is much more accentuated than between I. c and I d figures in spite of the fact the difference between the proper iteration numbers is $4\ 10^3$ in the former cases, and in the last ones this value is $170\ 10^3$, so much more bigger This fact is equal to the statement ofthe 1st theorem To be able to detect a measurable difference from the distribution which is answe-

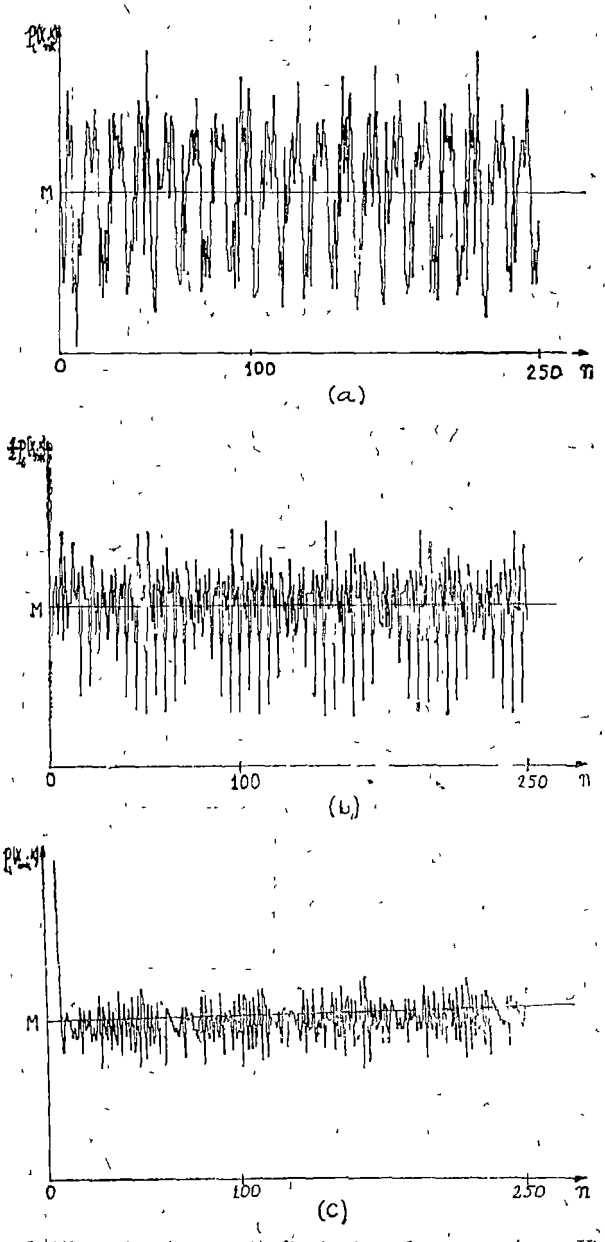

Fig 2 The natural procent's fluctuation diagram $p_s(x_{nK}, K)$ vs n for $K = 30 \cdot 10^3$, corresponding to the cell which contains the S_1 supertrack for different control parameter value(r) in the intermittency zone a) $r = 3.82700$, $M = 5.46\%$ b) $r = 3.82770$, $M = 8.29\%$ c) $r = 3.82825$, $M = 15.05\%$ where $M = \langle p(x_0, K)\rangle^{(n)} = p_s(x_0, nK)$ For each diagram was made in total $nK = 7500 \cdot 10^3$ iterations.

ring to the I d. figure, the length of the trajectory which founds the new distribution must be at least doubled: $2K = 400 \cdot 10^3$.' But according to the 2^{nd} theorem this difference will be also much smaller than in the case of the first pair of figures and is decreasing while increasing the K. Let's perform now the measurements presented in the 2^{nd} section: $p_i(x_0, K), p_i(x_K, K), \ldots, p_i(x_{nK}, K), \ldots$. If we represent $p_i(x_{nK}, K)$ vs. n we get the II. a—c fluctuation figures. I investigated those intervals (C cubes) that contain the singularities of the probability density function of the map, i e. those that contain the supertracks (3, 4, 5). The numerical analyse was made on the supertrack S_1 because this was the most accentuated but the behaviour of the natural procent which belongs to the other supertracks was calitatively the same as in the case of the S_1. I investigated the dominions of that control parameters which are qnite before the periodical windows in the intermittency zones.

In the periodical windows the fluctuations certainly don't exist but they appear in the intermittency zones and they become more accentuated while decreasing the control parameter.

The investigation of the fluctuations result in the following qualitative scenario:

chaos dominion	"entire" chaos	intermittency	periodical window
the fluctuations of the natural proc.	chaotical fluctuations	quasiperiodical and periodical fluc.	no fluctuations

Observations. 1) the fluctuation figures were made using $K = 30\,000$, because in this case the natural procents approximate the natural measure faithful enough, with 1%. Increasing N, certainly K also has to be increased;

2) the method depends of an experimental parameter which is K, but we are interested in such measurements which supply such informations which are caracteristical to chaos, so are independent to that experimental parameter. We can easily demonstrate that the periodicity of the fluctuations is exactly an information of this kind (using the (8), (9) equalities). If $T = mK$ and if we assume that the signal is periodical and its period is P (in K units), the periodicity will remain, but the new period (in T units) is:

$P' = \frac{P}{(P, m)}$ where (P, m) denotes the greatest common divisor of the number P and m.

Acknowledgements. The computations were made on an IBM PC/268 computer and in this sense I express my thanks to a little collective from Unirea enterprise for the work possibility on this computer.
I would like to thank Vinţeler Emil for many useful comments and discussions.

REFERENCES

1 J Doyne Farmer, Edward Ott and James A Yorke, *Physica*, 7D, 153 (1983)
2 Filipe J Romeiras, Celso Grebogi, Edward Ott, *Phys Rev*, **A 2**, (1990)
3 I A Dorobanţu, A L Barabasi and L Nitsch, "On the way to and beyond chaos A display of universalities", reprint, march 1989
4 Roderick V Jensen and Christopher R Myers, *Phys Rev*, **A 2**, 1222 (1985)
5 Edison, S Flynn, C. Holm, D Veeks and R F Fox, *Phys Rev*, **A 4**, 2809 (1986)
6. H G Schuster, "Deterministic Chaos" (Physik Verlag, 1983)

STUDIA UNIV BABEŞ-BOLYAI, PHYSICA, XXXV, 1, 1990

TIME INVERSION SYMMETRY AND QUASI-ENERGY STATE DEGENERACY

I.I. GERU*

Received March 7, 1990

ABSTRACT. — A geometric interpretation of time inversion transformation and Kramers' theorem for the case of stationary energy-states based on a theoretical and group-like approach is given It is shown that a traditionally performed expansion of point symmetry group to magnetic-symmetry group is true only for systems with integral total angular momentum J. With semi-integral J such expansion should be done by means of 4-fold cyclic group $\{k, k^2, k^3, k^4 = e\}$ (k — time inversion operator) that gives rise to four groups of magnetic symmetry (instead of 58 for integral J) which are isomorphic not to Shubnikov's but to Belov's lower groups of four-colour-symmetry.

Quantum-physics systems simultaneously having symmetry with respect to both the time inversion and the time translation are considered It is demonstrated that Kramers' degeneracy of quasi-energy states is present (absent) at semi-integral (integral) value of J An additional (compared with Kramers' one) degeneracy of quasi-energy states is found for the cases which time inversion operators does not commutate with time translations operators.

Introduction. Time inversion symmetry for stationary states of *quantum-physics* systems gives rise to the presence of magnetic symmetric groups in addition to Kramers degeneracy 58 point groups of magnetic symmetry [1, 2], which are known to be isomorphic to Shubnikov,s groups of antisymmetry, are referred to systems with integral total angular momentum J [3] only.

At semi-integral J totally 4 point groups of magnetic symmetriy are possible which are isomorphic to Belov's lower groups of four-colour symmetry [3] but not to Shubnikov's ones

Time inversion symmetry by itself for non-stationary states does not lay additional restrictions on quasi-energy states compared with the case of stationary states However, a simultaneous account of time inversion symmetry and time translation symmetry causes additional restrictions on quasi-energy states, compared with the case of stationary states. However, a simultaneous account of time inversion symmetry and time translation symmetry causes additional restrictions on quasi-energy states, since each individual operator of both the time inversion and the time translation does commutate with "Hamiltonian" $H = H(t) - i\hbar \frac{\partial}{\partial t}$ and does not commutate with each other for the common case

The present paper demonstrates that depending on the commutating properties of time inversion and translation operators at any entire number of periods, the quasi-energy states of a quantum system can be either non degene-

* *Moldavian State University, Physics Department, 177003 Kishinev, Moldova.*

rated (when these operators commutate with each other) or 2-fold degenerated (when operators specified do not commutate with each other).

2. Time inversion symmetry for stationary states.

The Hamiltonian of N-partial quantum physics system commutates with the Wigner time-inversion operator in the absence of magnetic field

$$K = {}^{N}\prod_{n=1}^{N} \sigma_{yn} \cdot K_0, \tag{1}$$

where σ_{yn} is the Pauli imaginary matrix that is relevant to n—particle with spin $1/2$; K_0 — the complex conjugation operator [4].

When adding the elementary angular momenta to form up systems with angular momenta J_γ (which in its turn form up a system with integral angular momentum J) the operator can be represented as [5]

$$K = \prod_{\gamma=1}^{p} U_\gamma K_0 = \mathcal{U}_\gamma K_0,$$

where U_γ represents the unitary parts of operator K in $(2J_\gamma + 1)$ — dimentional spaces of angular momenta. Matrices of unitary operators U_γ are considered to be antisymmetrical with matrix elements on secondary diagonal, being equal to $+1$ and -1 in turn and with other matrix elements equal to O Matrix U_γ is symmetrical with respect to its reflection in the center of secondary diagonal at integral and it is antisymmetrical at semi-integral value of J.

Transformation of time inversion for N—partial system with angular momentum J has the following geometrical meaning The state with angular momentum J in a functional $(2J + 1)$ dimensional discrete space corresponds to the point that makes an antirotation about an axis passing through the origin of coordinates under the effect of time inversion transformation When J is semi-integral this antirotation is carried out through an angle of $\pi/2$ and the system returns to the initial state of wave function with initial phase after four consecutive antirotations of such kind in one direction. When J is integral, the system passes into the initial state after two antirotations through π-angle In this case the second antirotation is reverse to the first one. The transformations described are geometrically represented in Fig. 1 for instances when K is equal to 1/2, 1 and 3/2. The antisimilarity operation is consistent with the transition to a complex-conjugation wave function.

The varying geometrical behaviour of systems with integral and semi-integral J at time inversion is related to the above-mentioned property of unitary operator U. In order to be assured of it, it is necessary to plot a $(2J + 1)$ — dimensional unit cube inscribed into $(2J + 1)$ — dimensional unit sphere with its center in the origin of coordinates. Initially, this cube should take a position such the coordinate axis pass through the middles of $2J$—dimensional planes. Then it is required to turn the cube so that the top's position selected on the

sphere is defined by $(2J+1)$ values of functions playing the role of coefficients in the expansion of N—partial wave function

$\psi^{(J)}(\vec{\tau}_1, \vec{\tau}_2, \ldots, \vec{\tau}_N)$ with respect to the base spinors $\zeta_\sigma^{(J)}$:

$$\psi^{(J)}(\vec{\tau}_1, \vec{\tau}_2, \ldots, \vec{\tau}_N) = \sum_{\sigma=-J}^{\sigma=+J} \mathcal{S}_\sigma(\vec{\tau}_1, \vec{\tau}_2, \ldots, \vec{\tau}_N)\, \zeta_\sigma^{(J)} \tag{37}$$

which satisfie normalization conditions:

$$\sum_{\sigma=-J}^{\sigma=J} \int |\mathcal{S}_\sigma(\vec{\tau}_1, \vec{\tau}_2, \ldots, \vec{\tau}_N)|^2 \, d\vec{\tau}_1 \, d\vec{\tau}_2 \ldots d\vec{\tau}_N \tag{4}$$

It is obvious that time inversion operation involves antirotation of „state vector" directed along one of principal diagonals of $(2J+1)$-dimensional cube with transition on the other principal diagonal (Fig. 1).

A point-behaviour analysis which describes the state of a system under consecutive transformations of time inversion made on it, has allowed to clarify a geometric meaning of Kramers' theorem on additional degeneracy of

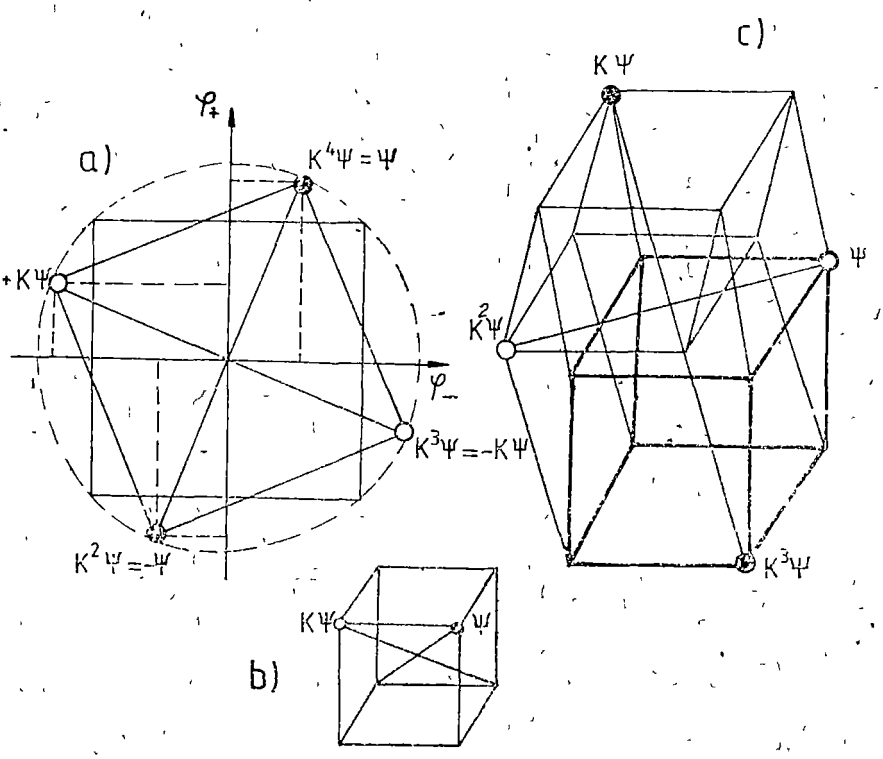

Fig 1 a) J = 1/2; b) J = 1, c) J = 3/2

energy levels attributed by time inversion symmetry. It consists in the existence of a sole pair of mutually orthogonal diagonals (with accuracy of up to movement group) in the $(2J + 1)$-dimensional Euclidean cube when J is semi-integral and in the absence of such a pair, when J is integral [3].

Abelian group of symmetry $2' = \{K, K^2 = e\}$ is used to expand classical crystallographic groups of magnetic symmetry [1, 2] However, due to peculiarities in the structure of operations U_γ such expansion, as it was said, is feasible for systems with integral total angular momentum only. None of the 58 black-and-white groups of magnetic symmetry can be used to investigate a magnetic structure of systems with semi-integral total angular momentum. In the case of systems with semi-integral J the expansion of classical groups up to the group of magnetic symmetry should be carried out by means of a cyclic 4-fold group $U' = \{K, K^2, K^3, K^4 = e\}$ [3]. When J is semi-integral, operators K^q shall meet the requirements as follows

$$K^2 = -K^4 = -e, \quad K^3 = -K$$

Due to a higher symmetry of group $4'$ in comparison with group $2'$ the number of magnetic symmetry groups with semi-integral J is considerably less than that with integral J The Ref. [6] reports about groups of generalized symmetry on the basis of expansion of 32 crystalic classes with the help of these very crystalic classes. Using the results of this work one can find out that there are only 4 lower groups of magnetic symmetry when J is semi-integral (instead of 58 groups with integral J). These are Belov's point groups of four-colour symmetry $4^{(\overline{4}'z)}$, $4^{(4'z)}$, $4^{(4'z)}/m^{(1)}$ and $4/^{(4'z)(2)}m$ [3] where a small line on the top indicates a mirror rotation and a dash means an antirotation

Along with antirotations forming up the group $4'$ one can take into account the other elements of generalized symmetry of the square with two similarly coloured, diagonally opposite tops This square is placed in the plane perpendicular to the antirotation axis (reflections $m_{xy}^{(i)}$ in diagonals and antireflections $m_v^{(i)}$ in straight lines passing through centres of opposite sides, $i = 1,2$) Expansion of classical point groups of symmetry up to groups of magnetic symmetry is possible then by means of group $4'm'm$ In the latter, the transformation of time inversion can be represented as a product of reflection type m_{xy} by relevant antireflection, type m'_{xy}.

$$K = m_x'^{(i)} m_x^{(i)} = -m_{xy}^{(i)} m_x'^{(i)} = -m_x'^{(j)} m_{xy}^{(i)} = m_{xy}^{(i)} m_x'^{(i)},$$
$$m_v'^{(i)} m_{xy}^{(i)} \pm m_{xy}^{(i)} m_x'^{(i)} = m_{xy}^{(i)} m_x'^{(j)} \pm m_x'^{(j)} m_{xy}^{(i)} = \pm\eta, \tag{5}$$

where $\eta_+ = 0$, $\eta_- = 2K$, $i, j = 1, 2$ $(i \neq j)$. Only groups 422, $4mm$ and $42m$ out of entire 32 point groups admit expansion by means of group $4'm'm$. In this very generalized case there are also 4 point lower groups of generalized symmetry i.e. groups of four-colour symmetry $4^{(4'_z)}\ 2^{(m'_x)} 2^{(m_{xy})}\ 4^{(4'_z)}\ m^{(m''_x)} m^{(m_{xy})}\ \bar{4}^{(4'_z)} 2^{(m'_x)}\ m^{(m_{xy})}$ and $\bar{4}^{(4'_z)}\ 2^{(m_x)}\ 2^{(m_{xy})}$ [3].

3. Time inversion symmetry for non-stationary states

Non-stationary states of particles (quasi-particles) in an external periodic field of high intensity are described conveniently by means of the notion of quasi-energy [7, 8]. Feasibility of such a description is attributed by the fact that the Hamiltonian of the system in the presence of a time-periodic field with frequency ω has the property of time periodicity.

$$H(\vec{x}, t+\tau) = H(\vec{x}, t), \ \tau = \frac{2\pi}{\omega}. \tag{6}$$

The time-dependent Schrodinger equation can be solved as follows

$$\Psi_\zeta(\vec{x}, t) = S(\vec{x}, t)\, e^{-\frac{i}{\hbar}\mathcal{E}t}, \tag{7}$$

where

$$S(\vec{x}, t) = S(\vec{x}, t+\tau). \tag{8}$$

Here, $\mathcal{E}$ — is the system quasi-energy, $\vec{x}$ includes both the spatial and the spin coordinates. A time-periodic wave function $S(x, t)$ is quadratically integrable and is consistent with the Schrodinger equation

$$\left[H(\vec{x}, t) - i\hbar\frac{\partial}{\partial t}\right] S(\vec{x}, t) = \mathcal{E}S(\vec{x}, t). \tag{9}$$

Time translation operators $T_{m\tau}$ ($m = 0, \pm 1, \pm 2, \ldots$) commutes with operator $H(x, t) - i\hbar\frac{\partial}{\partial t}$ and set up the Abelian group of unspecified symmetry representation which can be characterized by means of quasi-energy values $\mathcal{E}$ (τ is fixed and given by an external source)

$$T_{m\tau}\Psi_{\mathcal{E}}(\vec{x}, t) = e^{\frac{i}{\hbar}\mathcal{E}\tau}\Psi_{\mathcal{E}}(\vec{x}, t). \tag{10}$$

In the general case, a countable set of wave functions belongs to the given value

$$S_{lm}(\vec{x}, t) = f_l(\vec{x})e^{im\omega t} \tag{11}$$

$$(l = 1, 2, \ldots; m = 0, \pm 1, \pm 2, \ldots).$$

The functions $S_{lm}(\vec{x}, t)$ can be regarded as state vectors in generalized Hilbert space $\mathfrak{R} + \mathfrak{T}$ (functions $f_l(\vec{x})$ are defined in space $\mathfrak{R}$, while $\exp(im\omega t)$ is defined in space $\mathfrak{T}$ [9]). The operator $-i\hbar\frac{\partial}{\partial t}$ in space $\mathfrak{R} + \mathfrak{T}$ is Hermitian and therefore Hamiltonian $\mathcal{H} = H(t) - i\hbar\frac{\partial}{\partial t}$ is Hermitian too in this space, and due to it each quasi-energy value is real while functions $S_{lm}(\vec{x}, t)$ belonging to different values of quasi-energy, are orthogonal.

If $\mathcal{E}$ and $S(\vec{x}, t)$ are a proper value (quasi-energy) and a proper function of operator $\mathcal{H}$ correspondingly, then

$$\mathcal{E}' = \mathcal{E} + m\hbar\omega, \; S'(\vec{x}, t) = S(\vec{x}, t)e^{im\omega t} \tag{12}$$

are a proper value and a proper function of operator $\mathcal{H}$ for any integral m too. An entire wave function of the system is not changed in this case

$$S(\vec{x}, t)e^{-\frac{i}{\hbar}\mathcal{E}t} = S'(\vec{x}, t)e^{-\frac{i}{\hbar}\mathcal{E}'t} \tag{13}$$

As a consequence of (13), all solutions (12) are physically equivalent at any integral m. Existence of equivalent states of quasi-energy makes it possible to bring any value of quasi-energy to the point in "a reduced zone of quasi-energy space" (similar to the first Brillouin zone of one-dimensional periodic lattice).

It is carried out with the help of a real number E for which

$$E - \frac{1}{2}\hbar\omega \leqslant \mathcal{E} \leqslant E + \frac{1}{2}\hbar\omega \tag{14}$$

Zone selection, i e selection of E is arbitrary Let us mak clear the how functions at time inversion are transformed The Equation (9) is not invariant under operator K from (1) and (2) since $[K, H] \neq 0$ Nevertheless, one can define such operator K_t under which operator $\mathcal{H}$ is invariant

$$K_t^{-1}\mathcal{H}K_t = \mathcal{H}. \tag{15}$$

For this purpose let us define operator I_t by analogy with inversion operator in a coordinate space

$$I_t t = -t, \; I_t^2 = 1. \tag{16}$$

Operator I_t transforms function $F(t)$, obviously dependent on time, into function $F(-t)$.

$$I_t F(t) = F(I_t^{-1}t) = F(I_t t) = F(-t) \tag{17}$$

Since the states $S_{lm}(\vec{x}, t) = f_l(\vec{x}) \exp(im\omega t)$ and $Uf^*(\vec{x}) \exp(-im\omega t)$ belong to one and the same value of quasi-energy $\mathcal{E}$, the operator of time inversion for systems with quasi-energy spectrum assumes the following form with regard of (13)

$$K_t = UK_0 I_t. \tag{18}$$

The first reduced zone in a quasi-energy space has two special points Γ (in the center) and Λ (on its boundary). Let us consider consequences attributed to time inversion symmetry with spin not taken into account

A. Point Γ The star Γ consists of one point $\mathcal{E} = 0$. The point group $C_i \{e, I_t\}$; $\sum_{Q_0} \chi(Q_0^2) = 2$ (where Q_0 is a symmetry element converting $\mathcal{E}$ into $-\mathcal{E}$) is a symmetry group to which this point Γ belongs too. This is the case (a) by Wig

ner [4], i e. when an additional degeneracy caused by time inversion symmetry is not present.

B. Point Λ. $\mathcal{E}_\Lambda = \pi\hbar/\tau$ differs from $-\pi\hbar/\tau$ by "the vector of inverse lattice" $2\pi\hbar/\tau$

The group of Λ — point symmetry is C_i, $\sum_{Q_0} x(Q_0^2) = 1$, case (a).

With account of spin as in the case for stationary states, an additional degeneracy of quasi-energy levels is possible due to time inversion symmetry at $U^2 = -e$ and $K_i^2 = -e$ With the presence of a crystallin field it is required to define operator U in the space of basic functions of representations of crystallographiic point groups. An explicit view of this case is reported in [5].

4. A simultaneous examination of time inversion and time translation transformations

Hamiltonian H is simultaneously invariant under both the time inversion and the time translation transformations

$$[H, K_i] = [H, T_{m\tau}] = 0 \tag{19}$$

Let us consider a new group of transformations created by operators $K_i T_{m\tau}$. This new expanded group of transformations is not an Abelian one, compared with the time transformation group, because

$$T_{m\tau} I_i = I_i T_{-m\tau} \tag{20}$$

and therefore, in the general case (apart from below considered exception), we have

$$[K_i, T_{m\tau}] \neq 0 \tag{21}$$

The Hamiltonian of the system commutes with any two operators of transformations which do not commute with each other, the spectrum of proper values of Hamiltonian falls apart into "multiplets of degenerated states" [10] Since operator K_i is antiunitary, safety precautions are required when generalizing these results for the case of inequation (21)

Let us consider any proper function of Hamiltonian H which is simultaneously considered to be a proper function of operator $T_{m\tau}$ with proper value $e^{\frac{i}{\hbar} m\mathcal{E}\tau}$

$$H|\mathcal{E}> = \mathcal{E}|\mathcal{E}>, \tag{21a}$$

$$T_{m\tau}|\mathcal{E}> = e^{\frac{i}{\hbar} m\mathcal{E}\tau} |\mathcal{E}>, \tag{21b}$$

where the following notation is used for quasi-energy states

$$|\mathcal{E}> \equiv \Psi_{\mathcal{E}}(\bar{x}, t) = f_l(x) \exp\left\{i\left(m\omega - \frac{\mathcal{E}}{\hbar}\right)t\right\} \tag{22}$$

Then

$$HK_t|\mathcal{E}> = \mathcal{E}K_t|\mathcal{E}>,$$

$$T_{m\tau}K_t|\mathcal{E}> = T_{m\tau}I_tUK_0|\mathcal{E}> = I_tT_{-m\tau}UK_0|\mathcal{E}> =$$

$$= UK_0I_tT_{-m\tau}|\mathcal{E}> = UK_0I_te^{-\frac{1}{\hbar}m\mathcal{E}\tau}|\mathcal{E}>, \tag{21c}$$

from which it follows that

$$T_{m\tau}K_t|\mathcal{E}> = e^{-\frac{i}{\hbar}m\mathcal{E}\tau}K_t|\mathcal{E}>. \tag{21d}$$

Thus the spectrum of eigen values of $\mathcal{H}$ operator consists of degenerated state doublets that are eigen functions of operator $T_{m\tau}$ with eigen values $e^{\pm\frac{i}{\hbar}m\mathcal{E}\tau}$. Both these states pass from one to the other during time inversion K_t. In this case, the commutator $[K_t, T_{m\tau}]$ is defined by the following expression

$$[K_t, T_{m\tau}] = 2i\sin\left(m\frac{\mathcal{E}}{\hbar}\tau\right)K_t. \tag{23}$$

Particularly, for $l = 1$, the expression is as follows

$$|\mathcal{E}_1> = \varphi_{1m}(\vec{x}, t)e^{\frac{i}{\hbar}\mathcal{E}_1t} = f_1(\vec{x})e^{i\left(m\omega-\frac{\varphi_1}{\hbar}\right)t} \tag{24}$$

The action of commutator (23) on the state $|\mathcal{E}_1>$ (with regard to $f_1(\vec{x})$ function reality and without regard to spin) produces the following expression

$$[K_t, T_{m\tau}]|\mathcal{E}_1> = 2i\sin\left(m\frac{\mathcal{E}}{\hbar}\tau\right)|\mathcal{E}_1>. \tag{25}$$

According to (25) at

$$\frac{\mathcal{E}}{\hbar\omega} = \frac{K}{2m},\ K = 0, \pm1, \pm2, \tag{26}$$

operators K_t and $T_{m\tau}$ commutate

$$[K_t, T_{m\tau}] = 0, \tag{27}$$

i.e., in this case the quasi-energy state $|\mathcal{E}_1>$ is an eigen function of operation $[K_t, T_{m\tau}]$ with an eigen value being equal to zero, that is consistent to the presence of "singlets" (instead of "doublets") of quasi-energy.

On the basis of formulae (25)—(27) one can conclude that a quasi-energy spectrum in the non-degenerated energy spectrum consists of quasi-energy singlets, if the ratio of quasi-energy $\mathcal{E}$ to quantum energy $\hbar\omega$ is a rational number. When this ratio appears as an irrational number, each quasi-energy level is doubly degenerated. Since the power of a set of rational numbers is much less than that of irrational numbers, then it physically means that a quasi-energy

spectrum in the system with non-degenerated energy spectrum is composed of quasi-energy doublets.

It is worth noting that states $(1 + K_t)\varphi_{lm}(\vec{x}, t)$ and $i(1 - K_t)\varphi_{lm}(\vec{x}, t)$ with integral total angular momentum are simultaneously eigen functions of operators H and K_t, creating a real basis of eigen functions, whereas such real basis does not exist for systems with semi-integral total angular momentum because operator K_t does not have any eigen functions in this case that gives rise to Kramers degeneracy of quasi-energy states.

REFERENCES

1 M Hameimesh, "Theory of groups and its application for physical problems", Moskva, Mir, 1966, p 367
2 I S Zheludev, "Symmetry and its applications", Moskova, Atomizdat, 1976, p 286
3 I I Geru, "Colour symmetry and time inversion in systems with semi-integral total spin", *Proceedings of the USSR Academy of Science*, **268**, N 6, 1392—1394, (1980)
4 E Wigner, "Theory of groups and its applications for theory of atomic spectra, Moskva, IL, 1961, p 443
5 I I Geru, "Low frequency resonances of exitons and defect centers", Kishinev, Shtuntsa, 1976, p 194
6 V A Coptsik, I N Cotsev, "Magnetic (spin) and magneto-electric point groups of P-symmetry", Moskva, United Institute of nuclear research, 1974, p 19, preprint, P4—8466
7 L B Zeldovich, "Quasi-energy of quantum system being exposed to periodic action", *Journ of Experim and Theoret. Phys*, **51**, N 5(12), 1492—1495 (1966)
8 V I Ritus, "Shift and energy-level spliting by electromagnetic wave field," *Journ of Experim and Theoret Phys*, **51**, N 5(11), 1544—1549 (1966)
9 H Sambe, "Steady state and quasienergies of a quantum mechanical system in an oscillating field", *Phys Rev*, *Ser A*, **7**, N 6, 2203—2213 (1973)
10 C. Lipkin, "Quantum mechanics", Moskva, Mir, 1977, p 502

STUDIA UNIV. BABEŞ-BOLYAI, PHYSICA, XXXV, 1, 1990

TEMPERATURE DEPENDENCE OF 584 cm^{-1} DEPOLARIZED RAMAN LINE WIDTH OF 2 FLUOR-TOLUENE

T. ILIESCU* and V. SMARANDACHE**

Received April 17, 1990

ABSTRACT. — The temperature dependence of depolarized Raman line width for 584 cm^{-1} vibrational transitions of 2 fluortoluene was studied The reorientational times and potential energy barrier were determined

Different spectroscopic techniques (I R. depolarized Rayleigh, Raman, NMR) are used for the study of molecular dynamics in condensed phases [1]. The contribution of rotational and vibrational relaxation can be separated on the one hand, by the analysis of isotropic and anisotropic Raman line at only one temperature [2], and on the other hand, by studying the temperature dependence of Raman depolarized line width [3]

The total half-width $\Gamma_{1/2}$ of depolarized Raman lines is divided in two parts of which one is independent of temperature and is called the intrinsec width δ_0, determined by vibrational relaxation, and the other one $\Gamma(T)$, is temperature dependent and expresses the contribution of the chaotic motion of the molecules [4]

Thus

$$\Gamma_{1/2} = \delta_0 + \Gamma(T), \quad \Gamma(T) = \frac{1}{\pi c \tau_r} \tag{1}$$

where τ_r is the time of reorientation given by Debye's equation

$$\tau_r = 4\pi a^3 \eta/(3KT) \tag{2}$$

or Frenkel's equation

$$\tau_r = \tau_0 \exp\,[U_D/(KT)] \tag{3}$$

a — is the effective radius of molecule, η — the viscosity coefficient. K — Boltzmann's constant, T — absolute temperature, τ_0 — period of oscillation of the molecule in the equilibrium position, U_0 — activation energy for the transition of the molecule for the equilibrium position to another one

In the present paper, we study the temperature dependence of width for depolarized Raman line 584 cm^{-1} (A'', $\rho = 0{,}148$) of 2 fluor-toluene

The experimental details were given in [5]

* *University of Cluj Napoca, Department of Physics, 3400 Cluj-Napoca, Romania*
** *Chemistry Institute, 3400 Cluj-Napoca, Romania*

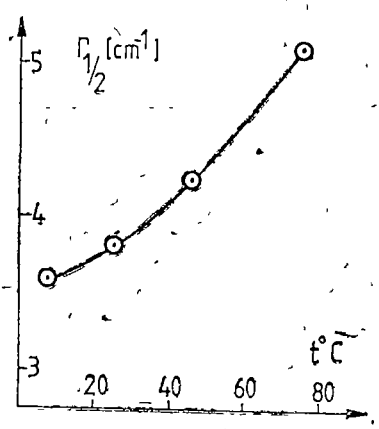

Fig 1 Half-width of 584 cm^{-1} band vs t

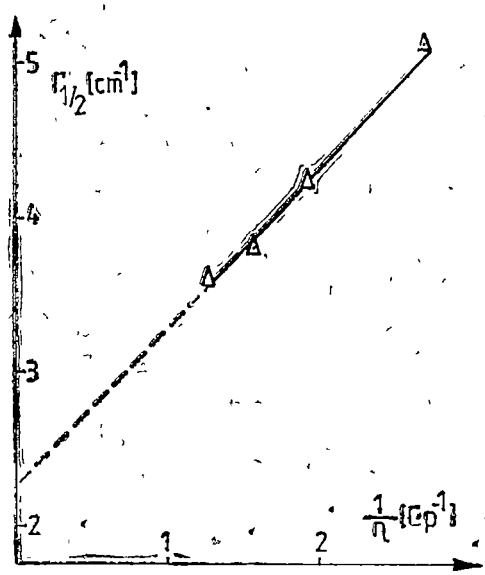

Fig 2 Half-width of 584 cm^{-1} band vs $1/\eta$

The spectral slit width was 0,35 cm^{-1}, so the finite slit width effect on the experimental data could be neglected 2 fluor-toluene from "Merck" was used after distillation

Fig 1 shows the exponential dependence of the width from temperature. Using the formulae (1) and (2) one obtains equation

$$\Gamma_{1/2} = \delta_0 + 3KT/(4\pi^2 a^3 c\eta) \qquad (4)$$

Fig 2 shows the linear dependence of $\Gamma_{1/2}$ vs $1/\eta$ The values of viscosity coefficients were taken from Landolt-Bornstein tables [6].

Assuming $1/\eta \to 0$ when the mobility of the molecules does no longer influence the line width, one can find from this diagram the intrinsic width, $\delta_0 = 2{,}25$ cm^{-1} From the formula (1) we obtain $\tau_r(t = 7{,}5\,°C) = 7{,}86$ p.s., $\tau_r(t = 75\,°C) = 3{,}72$ p s For 2 fluor-toluene, which bellongs to point group C_s, is extremely difficult to study reorientational motion about any specific axis of the molecule The intrinsic width obtained from isotropic Raman spectra of this line [7] show a little temperature dependence and was approximately 3 cm^{-1}. This difference in the intrinsic width is probably determined by vibrational dephasing which was neglected in the first method.

Using the formulae (1) and (3) one can obtain the equation

$$\Gamma_{1/2} = \delta_0 - \frac{1}{\pi c \tau_0} \exp\left(-U_{0r}/(KT)\right) \qquad (5)$$

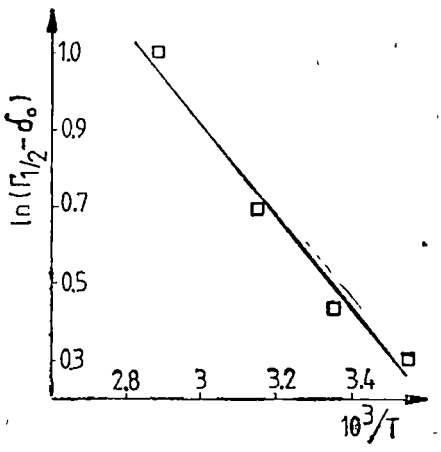

Fig 3 Logarithmic plots of $(\Gamma_{1/2}-\delta_0)$ vs $1/T$.

From logarithmic plots of $(\Gamma_{1/2}-\delta_0)$ versus $1/T$, the values of the potential energy barrier of molecular reorientation in liquid, U_{0r}, are obtained These dependences are shown in Fig 3 and the value of U_{0r} was 2 1 Kcal/mol
According to Frenkel [8] the temperature dependence of the viscosity is given by·

$$\eta = \text{const} \exp(U_b/KT) \qquad (6)$$

from which the U_b value can be obtained This value (2 62 Kcal/mol) is, in the limit of the experimental errors, in a good agreement with the U_{0r} value

The potential energy barrier U_{0r} can be considered as a characteristic feature of the medium in which molecular motion takes place Thus by using different solvents, the 2 fluor-toluene molecules can act as a "probe" of thermal motion of the solvent molecules

The Raman line width measurements in various solvents and at different temperatures for 2 fluor-toluene using the correlation vibrational and rotational functions are presented in another paper [7].

REFERENCES

1 S Bratos and R M Pick (Eds), "Vibrational Spectroscopy of Molecular Liquids", Plenum Press, New York, 1980
2 F J Bartoli, T A Litovitz, *J Chem Phys*, **56**, 404 (1972)
3 A V Rakov, *Optica i spectroscopia*, **7**, 202 (1959)
4 I Bratu, T Iliescu, I Milea, *J of Molecular Liquids*, **30**, 231 (1985)
5. I Bratu, K Klosterman, T Iliescu, S Aştilean, *J of Molecular Liquids*, **45**, 57 (1990)
6. Landolt-Bornstein, "Zahlwerte und Funktionen" 5 Teil, "Transport Phanomene" I (Viscositat und Diffusion) Springer-Verlag, Berlin—Heiderlberg—New York, 1969
7 T Iliescu, S Aştilean, T Vereş, I Bratu, "XX-th European Congress on Molecular Spectroscopy 25—30 August 1991", Zagreb
8 Y I Frenkel, "Kinetic theory of Liquids", Moscow, 1945

STUDIA UNIV BABEŞ-BOLYAI, PHYSICA, XXXV, 1, 1990

GROWTH CONDITIONS INFLUENCES ON THE COMPOSITION AND PROPERTIES OF $HgCr_2Se_4$ CRYSTALS

L. YA. PASENKO*, K. G. NIKIFOROV* and S. I. RADAUTSAN*

Received March 25, 1990

ABSTRACT. — The influence of the transport conditions on the chemical composition and physical properties of the $HgCr_2Se_4$ crystals growth by chemical transport vapour has been analysed

Introduction. The magnetic semiconductor spinels ACr_2X_4 (where A=Cd, Hg, Cu, Zn, Fe, Co and X=S, Se, Te) have been studied intensively This interest has been caused by the coexistence of interconnected ferromagnetic ordering and semiconductor properties which induced a number of specific effects [1, 2]. The nonstoichiometry possibility in a spinel structure leads to the evident dependence of the crystal properties from the growth condition [3—5]. On the other hand, the thermodynamical analysis demonstrates the real control of the vapour composition over growing crystal [6—8] But the lack of information about the crystal composition made the use of this control difficult.

In our work we studied the correlation between the transport conditions, crystal composition and physical properties for $HgCr_2Se_4$ the one of the more interesting [9] magnetic semiconductors.

Crystal growth and composition analysis. The polycrystalline $HgCr_2Se_4$ has been synthesized by the solid state reactions from HgSe, Cr and Se (and doping material, if necessary) at 800°C for 300 h [5] The crystal growth has been performed in the closed quarts ampoule using $AlCl_3$ as a transport gas source (see Tab. 1, 2).

The chemical composition of the grown crystals has been analysed by the electron probe mycroanalysis (EPMA) method using the "Camebax" 10

Chemical composition. The results of composition analysis are presented in Table 1 and Table 2 For all undoped $HgCr_2Se_4$ crystals the cation-to-anion mole ratio is less than 0,75 expected for the stoichiometric substance (Table 1). The selen ions form a dense packed structure of the crystalline lattice Subsequently their interstitial implantation (i.e. selen excess) turns out to be practically impossible [3, 11] while cation A vacancies formation seems to be quite possible.

The cation B-to-cation A mole ratio is less than 2 in all cases that may be explained by the chromium vacancies (Cr ions have preference to the B sites therefore $HgCr_2Se_4$ crystallizes in the normal spinel structure). Nevertheless the use of the $AlCl_3$ leads to the crystal contamination by Al (0,2 ... 0,3 at %) which can substitute Cr in B sites decreasing Cr/A ratio

* *Institute of Applied Physics, Academy of Science of the SSR Moldova, 277028 Kishinev, USSR*

Tabel 1

Growth conditions and chemical composition of the undoped $HgCr_2Se_4$ crystals

No	$AlCl_3$ content (mg/cm³)	T_s (°C)	T_g (°C)	Atomic ratios		
				Cr/Hg	(Hg+Cl)/Se	Se/Cr
1	2.7	655	635	1.83	0.72	2.16
2	3.1	650	600	1.96	0.69	2.17
3	4.6	700	670	1.91	0.69	2.20
4	5.0	700	670	1.83	0.73	2.13
5	7.0	690	670	1.89	0.71	2.17
6	7.0	690	670	1.82	0.71	2.18
7	7.0	700	660	1.86	0.72	2.13
8	12.2	660	615	1.96	0.72	2.09

Notes a) synthesis with Hg excess,
b) crystal Hg annealing,
c) repeated homogenized synthesis

For the understanding of the $HgCr_2Se_4$ vacancy nature we use the following results. The synthesis with Hg excess or the additional homogenization of $HgCr_2Se_4$ by the repeated synthesis leads to the Hg content increase in a formula unit (Table 1). The diffusional annealing of grown crystals in Hg vapour has the analogous effect. These facts demonstrate the existence of considerable quantity of the Hg vacancies in $HgCr_2Se_4$ (in contrast with $CdCr_2X_4$ crystals where the anion X vacancies are predominant [3, 11]. Chromium distribution in the crystals is more uniform in comparison with the Hg or Se distribution, that demonstrates the relative stability of this (Cr) element in such compound.

The increase of the transport gas source value leads to the decrease of the Hg and Se contents in the $HgCr_2Se_4$ crystals. It is possible that such Hg content decrease is connected with the ratio change between Hg, Cr, Se-content components in the vapour-gaseous phase at growth [8, 12]. On the other hand we suggest that the above mentioned Se content reduction can be conditioned by Cl substitution of Se ions during the growth process [11]. This assumption may be confirmed by our experimental data showing simultaneous content changes: the increase of Al (i.e. Cl) and the decrease of Se.

The working temperatures have less influence on the crystal composition because temperature dependence for vapour-gaseous phase composition is lower than that of transport gas concentration [8]. However it can be noted that the tendency of Hg content increase takes place when the average transport temperature becomes greater (at relative stability of Cr, Se contents).

The impurity concentration in all doped $HgCr_2Se_4$ crystals is less than in the initial polycrystals (Table 2). The evident tendency of cation A content increase and Se content decrease in such crystals can be mentioned as well. This may be explained by assuming that the doping ions do not substitute A cations, but occupy the vacant A sites at crystal growth.

Table 2

Chemical composition of the doped $HgCr_2Se_4$ crystals

No	Doping (at %)		Atomic ratios		
	Nominal	fact	Cr/A	-(A+Cr)/Se	Se/Cr
1 Ga	2,0	0,44±0,12	1,93	0,76	2,01
2 In	5,0	2,90±0,18	1,86	0,75	2,04
3 Ag	1,0	0,69±0,13	1,89	0,74	2,07
4 Ag	2,0	0,89±0,08	1,88	0,73	2,09
5 Au	2,0	0,61±0,09	1,85	0,73	2,10
6 Cu	3,0	2,93±0,36	1,81	0,74	2,09
7 Cu	5,0	3,36±0,29	1,81	0,72	2,15

Notes samples 1, 3, 4, 5 grown at T_s=650 660°C, T_g = 620 630°C, = 4 mg/cm³,
samples 2, 6, 7 grown at T_s = 710 720°C, T_g = 680 690°C, = 4 mg/cm³

Some physical properties. In this part should like to give a short survey on the correlation between the above mentioned EPMA results and some typical properties of the $HgCr_2Se_4$ crystals.

To begin with, the diffusional annealing in Hg vapour leads to the well known [2—4] metal like conductivity (in the ferromagnetic phase) The conductivity dependence on the Hg vapour pressure (P_{Hg}) is stronger at small P_{Hg} values (Fig. 1) Probably, such annealing "heals" the Hg vacancies (acceptor action) but does not eliminate the Se vacancies (donor action) The saturation effect is caused by the limitation of Hg vacancy healing process.

The reduction of the typical low temperature maxima of the ferromagnetic resonance linewidth $2\Delta H$ (in 100 direction) takes place when the doping content increases (Fig 2a) It is well known that such maxima are formed by tetravalent chromium ions arising from Hg vacancies influence [13, 14]. Therefore the above mentioned effect demonstrates the filling of the Hg vacancies by the doping ions.

The analogous FMR linewidth $2\Delta H$ reduction has been observed as a result of the decreasing of the transport gas concentration at growth (Fig 2b). This fact can be explained by the decrease of the Hg vacancies quantity.

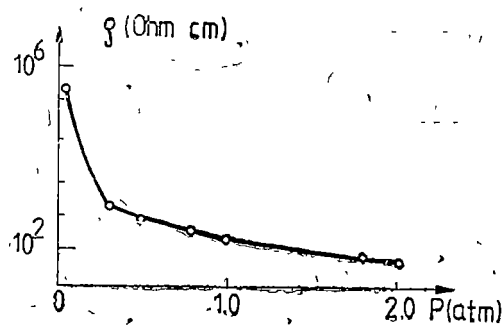

Fig 1 Conductivity dependence (at 77 K) for annealing $HgCr_2Se_4$ crystals from Hg vapour pressure

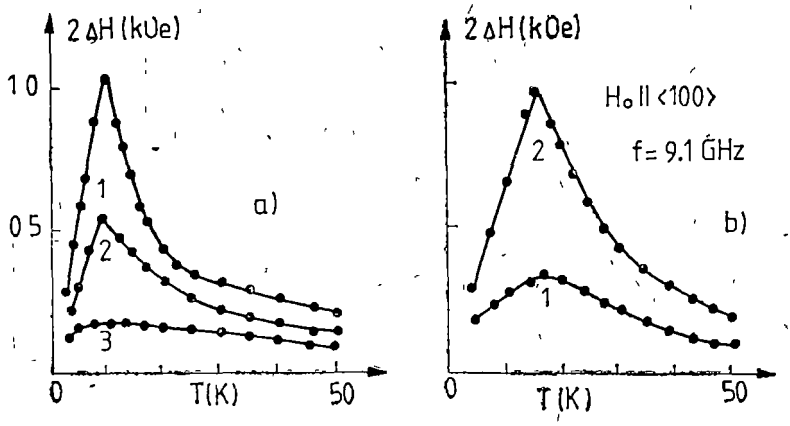

Fig 2 FMR linewidth temperature dependence for $HgCr_2Se_4$ crystals a) 1 — undoped, 2 — 1 at %Au doped, 3 — 2 at %Au doped, b) grown with $AlCl_3$ concentration equal to 2 7 (1) and 12 2 mg/cm³ (2) respectively

The additional homogenized synthesis results in the $HgCr_2Se_4$ magnetization increase (from 52,3 to 53,1 Gs.cm³.g^{-1} at 4,2 K) due to the total spin moment rise [15, 16] caused by the Hg vacancies (i.e. Cr^{4+} ions) quantity decrease. However the Hg annealing reduces the $HgCr_2Se_4$ magnetization (from 52,3 to 51,9 Gs.cm³ g^{-1} at 4,2 K) which is caused by the Hg/Se ratio increase due to the Hg vacancies "healing" and the Se vacancies (i.e Cr^{2+} ions [15]) formation

Conclusion. The presented results of the $HgCr_2Se_4$ studies confirm both the close correlation between growth conditions, chemical composition and crystal properties, and the real possibility to control the characteristics of the growing crystals.

It should be noted that the synthesis with Hg excess or the repeated homogeneous synthesis is useful for stoichiometric improvement

Our results have proved the necessity to use the growth condition change critically due to the possibility of the crystal composition degradation.

REFERENCES

1 K Miyatani, *Japan J Appl Phys*, **19,** 237 (1980)
2 S I Radautsan, *Nuovo Cim*, **2D,** 1782 (1983)
3 S I Radautsan, V E Tezlevan and K G Nikiforov, *J Crystal Growth*, **49,** 67 (1980)
4 A I. Merkulov, S I Radautsan and V E Tezlevan, *J Crystal Growth*, **57,** 563 (1982)
5 L Ya Pasenko, K. G Nikiforov and S I Radautsan, in "Chancogenide semiconductors", Ed L. L Kulyuk, Shtiintsa, Kishinev, 1985, p 26
6 P Gibart, L Goldstein, J L Dormann, *Japan J Appl Phys*, **19,** 183 (1980)
7 L Ya Pasenko, S. I Radautsan and K G Nikiforov, in , 7- th All-Union Conf on Growth Processes of Semiconducting Crystals", Novosibirsk, 1986, v 1, p 269

8 V K Belyaev, K G Nikiforov, S I Radautsan and V A. Bazakutsa, *Cryst Res Technol*, **24,** 371 (1989)
9 A Selmi, M Herities and P Gibart, *Progr Crystal Growth and Charact*, **13,** 121 (1986).
10 L Ya Pasenko, K G Nikiforov and S I Radautsan, *J Crystal Growth* (to be published)
11 A Ametani, *Bull Chem Soc Japan*, **49,** 450 (1976)
12 P Gibart, J Crystal Growth **43,** 21 (1978)
13 K G Nikiforov, L Ya, Pasenko, A G Gurevich, S I Radautsan and L M Emiryan, *Sov Phys — Solid State*, **27,** 137 (1985)
14 J M Ferreira and M D Coutinho-Felho, *J Magn Mater* **54—57,** 1280 (1986)
15 H Pinch and S Berger, *J Phys Chem Sol* **29,** 2091 (1968)
16 K Masumoto, T Kilyosawa and I Nakatani, *J Phys Chem Sol* **34,** 569 (1973)

STUDIA UNIV BABEŞ-BOLYAI, PHYSICA, XXXV, 1, 1990

ELECTRICAL AND PHOTOELECTRICAL PROPERTIES OF Me-SEMICONDUCTOR/As_2Se_3—Al HETEROSTRUCTURES

V. V. BIVOL', M. A. IOVU*, M. S. IOVU* and E. G. KHANCHEVSKAYA*

Received March 15, 1990

ABSTRACT. — The influence of the metallic electrode to the Me-In_2S_3/As_2Se_3-Al and Me-InP/As_2Se_3-Me heterostructures on the current-voltage characteristics and photoconductivity spectral distribution was investigated. It is shown, that the polarity of applied field changes the shape of the lux-ampere and photoconductivity characteristics also The interest in such structures has been increasing because of the search for new photosensitive cells with an enlarged region of spectral photosensitivity for different applications

Introduction. In the previously papers [1, 2] was shown, that the material electrode exhibit an essential influence on the electrical and photoelectrical properties on the heterostructures based on the calcogenide glass thin films This influence is conditioned by the energetical barrier on the interface metal-calcogenide glass, the magnitude of which depends on the used materials and by the curvature of bands at the semiconductor/chalcogenide glass interface. Influence of metal electrode, contacting with a defect (In_2S_3) and amorphous (As_2Se_3) semiconductors, on the shape of current-voltage, lux-ampere characteristics and photoconductivity spectral distribution of the Me-In_2S_3/As_2Se_3-Al and p-InP/As_2Se_3-Me heterostructures was studied

Experimental The heterostructures were obtained on a glass substrate covered with lower metallic electrode by means of subsequent thermal deposition in vacuum of defect semiconductors (In_2S_3) chalcogenide vitreous semiconductors (As_2Se_3), layers and top electrodes (Al and Au) Thin films of Au, Al Cr, Ni, Bi, Sn metals and SnO_2 were used for electrodes A thin layer of a Zn_x In_{1-x} alloy is used as an ohmic contact to the single crystals of p-InP

Results and discussions. The effective resistance of the heterostructures Me—In_2S_3(p-InP)/As_2Se_3—Me is greater than summary resistance of the component thin films. The similar effect was observed for the heterostructure Sb_2S_3/As_2Se_3 [1].

The current-voltage characteristics for all used electrodes are non-symmetrical and display a rectification, the magnitude of current for negative polarity to the top electrode is greater than for the opposite polarity. For the heterostructure Me—In_2S_3/As_2Se_3—Al the ohmic region of forward current-voltage characteristics is followed by the power low behaviour (Fig 1), that seems to be linked with the space-charge-limited current in As_2Se_3. From the analysis of current-voltage characteristics for Me-In_2S_3/As_2Se_3—Al heterostructures with various electrodes the structure conductivity was seen decreasing with the metal work function φ_m increase.

This can be associated both with current flow at the In_2S_3/As_2Se_3 interface and with the specifical properties of the Me/In_2S_3 interface. Moreover, from

* *Institute of Applied Physics, Academy of Sciences of the SSR Moldova, 277028, Kishinev, USSR*

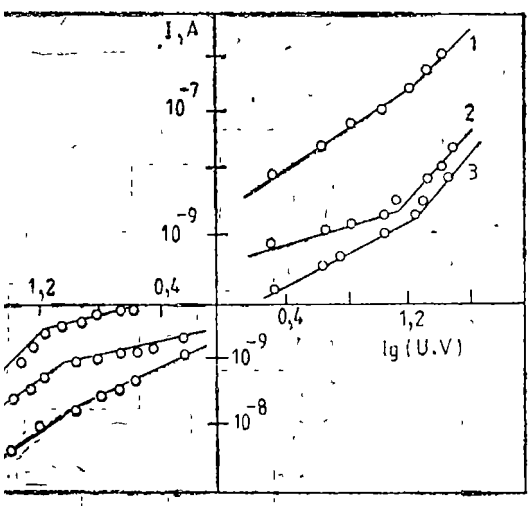

g 1 Current-voltage dependence for the Me—In_2S_3/As_2Se_3—Al heterostructure The polarity of plied field-relative to the lower electrode The material the lower electrode 1—SnO_2, 2—Al, 3—Au, The ckness of In_2S_3 film — 0,3 μm The thickness of As_2Se_3 film — 0 6 μm, T = 293 K

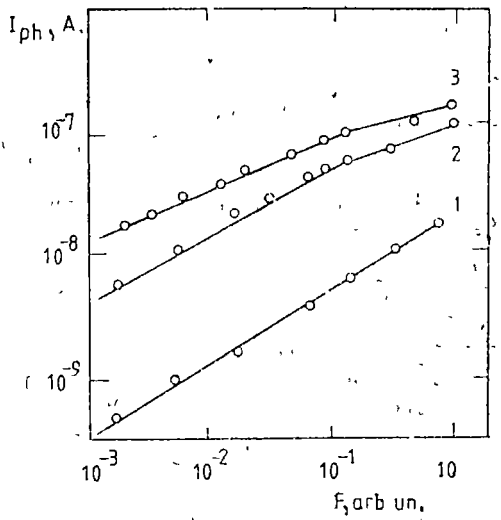

F ig 2 Lux-ampere characteristics for the Al — In_2S_3/As_2Se_3—Al heterostructure Illumination from the maximum photosensitivity region The applied bias U = 0 75 V at the positive polarity to the illumination top electrode Temprature T, K 1—295, 2—313, 3 — 337 F — light strenght The thickness of In_2S_3 film — 0 3 μm, the thickness of As_2Se_3 film — 0 6 μm

he experiments measuring the drift mobility, the In_2S_3 semiconductor was een to possess a bipolar conductivity.

The polarity of applied field exhibits an essential effect on photoelectrical haracteristics of the Me—In_2S_3/As_2Se_3—Al heterostructure Thus, the lux-ampere haracteristics exhibit a power low behaviour with the power index less than nity, the slope of which decreases with increase of temperature on the positive olarity to the top electrode (Fig 2) and increases at the opposite polarity

This behaviour of lux-ampere characteristics may be interpreted by Rose iodel [3], which assumes an exponential distribution of localized states in the orbiden gap of the amorphous semiconductor

$$N(E) = N_0 \exp(-E/kT_0), \quad (1)$$

with the parameter of this distribution T_0

According to this model the concentration of nonequilibrium carrier $n(p)$ ersus light strength F is given by

$$n(p) = BF^{\alpha}, \quad (2)$$

where B — is temperature independent, and the power index α depends on temperature

$$0{,}5 \leqslant \alpha \leqslant \frac{T_0}{T + T_0} = 1{,}0. \qquad (3)$$

According to (3) α decreases with the temperature increase If the drift mobility of amorphous semiconductors depends on light intensity, the relations (2, 3) are more complicated

The spectral distribution of photoconductivity of the Me—In_2S_3/As_2Se_3—Al heterostructures is characterized by a wide region of photosensitivity, due to the participation of amorphous and detect semiconductors of different gap widths (E_g for As_2Se_3 is 1,76 eV, E_g for In_2S_3 is 2 03 eV) It should be noted, that the Me—In_2S_3/As_2Se_3—Al heterostructures are photosensitive both in the reverse and forward directions, and photosensitivity depends on the used material electrode to the In_2S_3 (Fig 3)

The sharp lowering of photocurrent observed in the short-wave region is due to the process of the surface recombination at negative polarity to the top illuminated electrode

On Fig 4 a spectral distribution of photoconductivity of p-InP/As_2Se_3—Me heterostructures are given under reverse bias

The heterostructures with an Au electrode to As_2Se_3 are characterized by a wide interval of spectral photosensitivity from 0 9 to 2 4 eV, while for heterostructures with an Al electrode to As_2Se_3 this interval is narrowed down to 1 4 eV

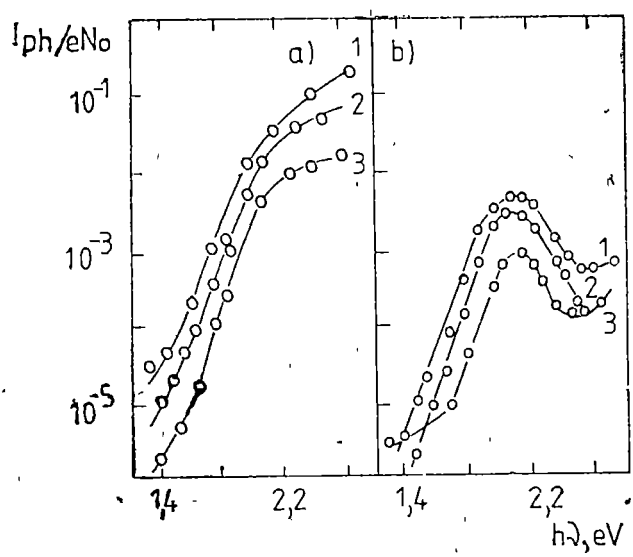

Fig 3 Photocurrent spectral distribution for the Me—In_2S_3/As_2Se_3—Al heterostructure with the SnO_2 (1), Al (2) and Au (3) electrodes at positive (a) and negative (b) polarity on the illuminated top electrode.

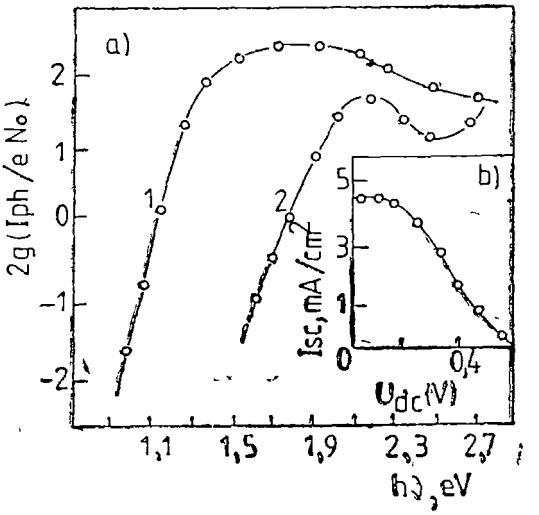

ıg 4 a) Spectral distribution of pho-
:onductivity of heterostructures p-InP/
$_2Se_3$—Me with Au (1) and Al (2) elec-
›des b) Load characteristic of hetero-
uctures with Au electrode to As_2Se_3

The maximum open-circuit voltage is equal to $U_{oc} = 0.6$ eV, the short-cuit current $I_{sc} = 4.6$ mA/cm², the fill factor is 0.5.

Conclusions. Analysis of the electrical and photoelectrical results may be ken into account and used for creation of recording media for holography. pecially, in the presence of electrical field and illumination on the surface of ıorphous semiconductor of the used heterostructure may appear the mecha-:al deformations, which change the reflectance and transmitance of the struc-re. The magnitude of this modification depends on the photocurrent density ross the heterostructure. In this point of view, the heterostructure Me—In_2S_3/ $_2Se_3$—Al with the SnO_2, Sn, Cr and Ni lower metalic electrodes, characterized th a maximum of photosensitivity, appears to be the most favorable. The terostructure p-InP/As_2Se_3 may be useful for constructing semiconductor ›des, photodiodes, and other solid state devices with amorphous semicon-ctors.

REFERENCES

A Andriesh et al, "The vitreous arsenic sulphide and it aloyes", Kishinev, Shtiintsa, 1981.
A. Andriesh et al, *Phys Stat Sol* (a), 1985, **89**, K 231
A Rose, "Concepts in Photoconductivity", Moskow, Mir, 1966.

Tiparul executat la Imprimeria „ARDEALULᵘ Cluj, C-da nr. 245.

În cel de al XXXV-lea an (1990) *Studia Universitatis Babeş—Bolyai* apare în următoarele serii:

matematică (trimestrial)
fizică (semestrial)
chimie (semestrial)
geologie (semestrial)
geografie (semestrial)
biologie (semestrial)
filozofie (semestrial)
sociologie-politologie (semestrial)
psihologie-pedagogie (semestrial)
ştiinţe economice (semestrial)
ştiinţe juridice (semestrial)
istorie (semestrial)
filologie (trimestrial)

In the XXXV-th year of its publication (1990) *Studia Universitatis Babeş—Bolyai* is issued in the following series:

mathematics (quarterly)
physics (semesterily)
chemistry (semesterily)
geology (semesterily)
geography (semesterily)
biology (semesterily)
philosophy (semesterily)
sociology-politology (semesterily)
psychology-pedagogy (semesterily)
economic sciences (semesterily)
juridical sciences (semesterily)
history (semesterily)
philology (quarterly)

Dans sa XXXV-e anné (1990) *Studia Universitatis Babeş—Bolyai* paraît dans les séries suivantes:

mathématiques (trimestriellement)
physique (semestriellement)
chimie (semestriellement)
géologie (semestriellement)
géographie (semestriellement)
biologie (semestriellement)
philosophie (smestriellement)
sociologie-politologie (semestriellement)
psychologie-pédagogie (semestriellement)
sciences économiques (semestriellement)
sciences juridiques (semestriellement)
histoire (semestriellement)
philologie (trimestriellement)

Abonamentele se fac la oficiile poştale, prin factorii poştali şi prin difuzorii de presă, iar pentru străinătate prin „ROMPRES-FILATELIA", sectorul export-import presă, P. O. Box 12—201, telex. 10376 prsfir, Bucureşti. Calea Griviţei nr. 64—66

Lei 55